Evaluation and development of CPT-based design methods for the laterally loaded pile in sand

M.Sc. Thesis

Final report

Student

D. J. Veldhuijzen van Zanten

4983548

Committee

Dr. A. Askarinejad

Dr. H. Wang

Prof. Dr. K.G. Gavin

Dr. F. Pisanò

Acknowledgements

This thesis is written in the context of a final requirement for obtaining the degree of Master of Science in Geo Engineering. The research has been conducted as part of the MIDAS research project at Delft University of Technology. During this research I have been supervised by Dr. Huan Wang from the TU Delft.

This research outlined in this thesis is of value to anyone who is interested in the use- and development of design methods for piles in sand that are subjected to monotonic lateral loads, especially for the application of offshore wind turbine (*OWT*) monopile foundations. The performance of five existing *CPT*-based *p-y* methods is qualitatively and quantitatively assessed and their strengths, weaknesses and limitations are explored. Furthermore, an alternative pile-soil interaction model is experimentally validated. This could not have been done without pile load test (*PLT*) data from Wang et al. (2020) and many others previous studies, as well as test data that were gathered using specialised TU Delft equipment such as the geotechnical centrifuge at the laboratory of Geoscience and Engineering and the instrumented MIDAS model pile.

A great number of people have contributed to the realisation of this thesis in a meaningful way. Firstly I would like to deeply thank my supervisor, Huan Wang. He has provided me with endless amounts of guidance, suggestions and expert knowledge in technical areas, as well as in the areas of research structure and reporting. We've had many interesting discussions along the way and without his valuable input and friendly support this research would not have been possible. I would furthermore like to thank Luke Prendergast and Yifan Yang, whose MATLAB code I could use and expand upon to respectively run pile load test simulations and to process CT scans. Finally from the TU Delft I of course want to thank the rest of my graduation committee, Amin Askarinejad, Ken Gavin and Federico Pisanò for their feedback and for the hours they spent attending my meetings and presentations and studying my report.

Lastly I would like to take the time to warmly thank my parents and other family who have always supported me unconditionally and my friends who have often set me on the right path. In particular I would like to thank Ewoud for his many tips and daily dose of good vibes, as well as Cor for offering me a wonderful distraction-free study retreat. It has been a journey with its ups and downs and your support has pulled me through.

Executive Summary

In the design of offshore wind turbine (*OWT*) foundations the key factor is the lateral response, due to large horizontal forces and overturning moments from winds, waves and currents. Because of the soil conditions that are typical to Northern Europe, 80% of installed *OWT*'s in this region have been built on monopile foundations. These monopiles are typically over 6m in diameter and short, with aspect ratios (*L/D*) under 8 (Kirkwood 2016). Since the power of an *OWT* scales with the square of its rotor length, turbines are expected to keep increasing in size and in turn monopiles will increase in diameter and decrease in aspect ratio (Lehnhoff, et al. 2020). Meanwhile, the European commission has proposed an ambitious goal of reducing greenhouse gas emissions by 55% compared to 1990 by the year 2030, which entails a renewable energy target of 40% (EUR-Lex - 52020DC0562 - EN - EUR-Lex, n.d.). Additionally, European offshore wind capacity is expected to double between 2021 and 2025 and to keep increasing rapidly after that (Windeurope 2022). Considering these trends and the relatively high economic cost of *OWT* foundations, there is a great need for optimized design of laterally loaded piles in sand.

An industry standard approach is provided by API (2014). This *p-y* method does have a few notable problems, especially regarding its use for *OWT* design. It was developed for long and flexible piles and has been shown to overestimate the initial stiffness of the *p-y* response for large-diameter piles (Choo & Kim 2015). Furthermore, it is sensitive to uncertainties in its sole input (the angle of internal friction). In order to address the latter problem and to conveniently and properly model in-situ soil complexity, several *CPT*-based *p-y* methods have been developed (Suryasentana & Lehane 2016).

In this thesis the performance of five *CPT*-based *p-y* models by Novello (1999), Dyson & Randolph (2001), Li, et al. (2014) and Suryasentana & Lehane (2014;2016) is assessed. This is done in part by comparing the measured load-deflection response from a set of lab- and field tests that is representative for offshore monopile structures to the predicted response generated by a MATLAB pile-response model that incorporates the aforementioned *p-y* models. It is found that with the exception of Suryasentana & Lehane (2014), alle models are more accurate at large- than at small displacements. Furthermore, the models are generally conservative at a groundline displacement of D/100 and unconservative at a groundline displacement of D/10. The latter is likely related to inability of the models to adequately capture the ultimate soil resistance. The strongest found correlation with prediction accuracy is a negative one with pile rigidity at small displacements. The models from Dyson & Randolph (2001) and Li, et al. (2014) generate predictions with the highest mean accuracy, though all models perform relatively poorly when compared to a benchmark from Burd, et al. (2019).

The aforementioned *CPT*-based *p-y* models are tested further through a number of new instrumented pile load tests in the TU Delft geotechnical centrifuge and the experimental methods for these tests are evaluated. Image analysis of CT scanned sand samples shows that though there is substantial non-uniformity present in samples prepared through hand raining, this method yields acceptable results and is preferable to preparation using a sand raining machine. Secondly, though soil disturbance does occur as a result of pile installation at 1*g*, this is not likely to greatly impact the results. A comparison of the load-deflection predictions generated with the *p-y* models (including API) for these load tests supports the notion that the initial response from the API (2014) model is far too stiff and that it is therefore unconservative in the prediction of the limit states. Furthermore, a modified 5^{th} order polynomial fitting method is found to adequately fit discrete bending moment data and in turn *p-y* curves are produced. These show that the p_u from the models Suryasentana &

Lehane (2014;2016) is only reached at shallow depths and does not match the measured ultimate resistance. Finally, at all except the shallowest depths the *CPT*-based *p*-*y* models strongly overestimate *p* though the resulting prediction of the load-deflection response is more reasonable.

As mentioned previously, the *CPT*-based *p*-*y* models do not perform optimally for the studied experimental cases, especially at small groundline displacements. This can likely be attributed to the fact that they were generally developed from test data on long and flexible piles. Additionally, rigid piles under lateral load develop moments and shear forces at the base that are not taken into account by methods that rely solely on lateral soil resistances (Peralta 2010). To solve these problems the PISA model with additional soil reaction terms was developed and it has been proven to provide better displacement predictions than traditional methods relying on lateral soil resistance (Byrne, et al., 2015a). However, this model is more complex and may not be the most convenient method to use. A less complex alternative has been proposed which uses a simplified rotational pile-soil interaction model to capture the load-displacement behaviour of perfectly rigid piles of varying diameter, stress level and loading eccentricity. Numerical simulations by Wang, et al. (2022) have shown this to work and in this thesis these results are validated using experimental data. The unification of the pile responses is found to work, but is not as successful for the experimental data. This may be due to several factors, the most likely of which are variations is sand density and imperfect rigidity of the model pile. However, the results support use of methods based on the aforementioned simplified rotational pile-soil interaction model, such as the rotational spring model proposed by Wang, et al. (2022).

List of abbreviations

API	American Petroleum Institute
CV	Coefficient of variation
CT	Computed tomography
CPT	Cone penetration test
DNV	Det Norske Veritas
DOF	Degrees of freedom
FEA	Finite element analysis
FEM	Finite element method
FLS	Fatigue limit state
LAP	Lateral analysis pile
LVDT	Low velocity displacement transducers
PISA	Pile soil analysis
PLT	Pile load test
OWT	Offshore wind turbine
SLS	Serviceability limit state
SPT	Standard penetration test
ULS	Ultimate limit state
A	Area
BM	Bending moment
C1, C2, C3	Coefficients function of soil friction angle (API)
D	Diameter
Dr	Relative density
E	Young's modulus
e	Loading eccentricity
E_p	Young's modulus pile
E_s	Young's modulus soil
F	Force
f_s	Sleeve friction
g	Gravitational acceleration
G_{max}	Maximum shear modulus
H	Lateral load
HS	Hardening Soil
I	Second moment of area
K	Net pressure coefficient
K0	Coefficient of earth pressure at rest
k_i	Initial spring stiffness
K_{py}	Sub-grade reaction modulus
K_s	Spring stiffness
L	Embedded length
M	Moment
M_r	Moment relative to the centre of rotation
p	Soil resistance
p_a	Atmospheric pressure

p_u	Ultimate soil resistance
p_{ud}	Ultimate soil resistance for deep mode of failure
p_{us}	Ultimate soil resistance for shallow mode of failure
q_c	Cone resistance
R	Pearson's correlation coefficient
r	Radius
t	Wall thickness
u_g	Water pressure at ground level
y	Lateral displacement
y_0	Lateral groundline displacement
z	Depth
γ	Volumetric weight
γ'	Effective volumetic weight
ε	Strain
η	Accuracy metric
θ	Rotation
θ_0	Groundline rotation
ρ	Ratio metric
σ_v	Vertical stress
σ'_v	Effective vertical stress
φ	Curvature
φ'	Effective friction angle
ψ	Pile cross section rotation
ω	Angular velocity

Contents

Part 1. Introduction and theoretical background

1.1 Introduction

1.1.1 Background & Motivation

For a typical wind farm, the support structures of the turbines can take up more than 30% of the total cost and play an important role in the economic feasibility of the whole project. Due to large horizontal forces and overturning moments from the wind, wave and currents, the lateral response of foundations is the key factor in the design. Among all the foundation types, monopiles are the most preferred for supporting offshore wind turbines (OWTs) and have been used in around 80% of total installations in Europe. As the seabed in offshore areas of Europe is dominated by dense sands, the loads on *OWT*'s in typical water depths of 10m to 40m can be effectively resisted by large diameter (*D*) monopiles with low aspect ratios (*L/D*, where *L* is the embedded length of monopile).

The diameters of monopiles installed in Europe are usually larger than 6 m and the aspect ratios are less than 8. Meanwhile, monopiles with diameter of 10 m and aspect ratio of 3 are under consideration for turbines with larger capacity in deeper waters (Kirkwood 2016, Negro et al. 2017). The power of an OWT scales with the square of its rotors (Lehnhoff, et al. 2020). This is why turbines are expected to keep increasing in size in the future, as can be seen in Figure 1. In turn, this will lead to increases in monopile diameters and therefore lower *L/D* ratios.

Additionally, the European commission has recently proposed new ambitious goals concerning the reduction of greenhouse gas emissions with a 55% decrease compared to 1990 by 2030, which would mean a renewable energy target of 40% (EUR-Lex - 52020DC0562 - EN - EUR-Lex, n.d.). As of January 2021, Europe had a total wind power capacity of 220 GW, of which 194 is located onshore and 25 GW offshore. This is expected to increase by 105 GW before the end of 2025, 30% of which will come from offshore facilities. This would mean a doubling of offshore wind capacity over a five year period (Windeurope 2022). Taking all these trends and the relatively high economic cost of wind turbine foundations into account, there is a great need for the optimization of wind turbine foundation designs and therefore a need for optimized design methods of laterally loaded piles in sand.

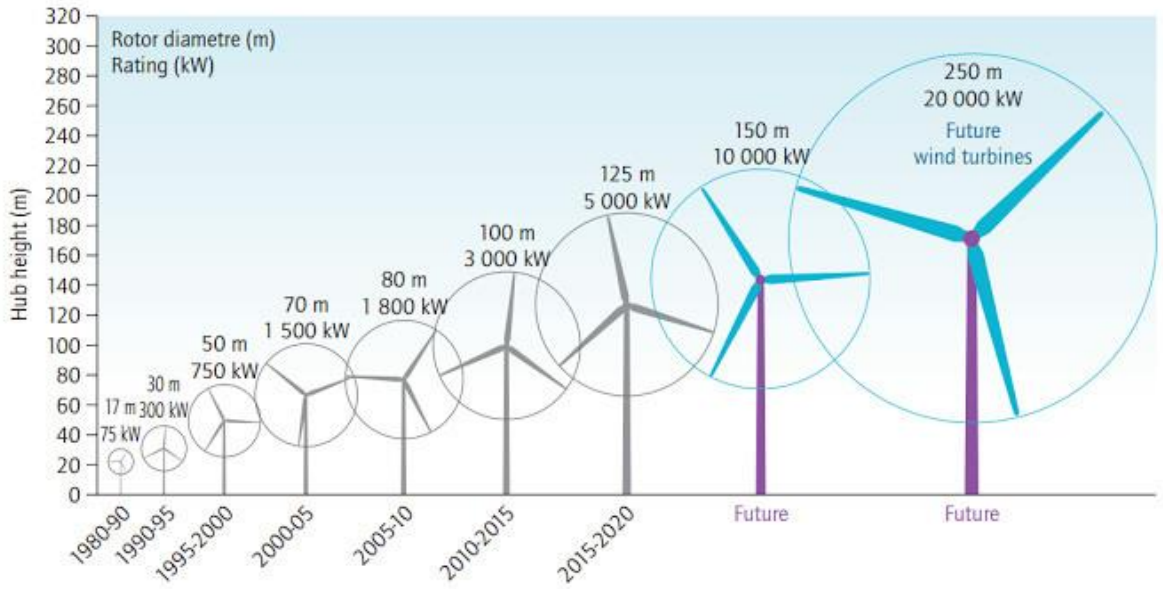

Figure 1: Trends of increasing wind turbine size and -power (Padmanathan et al. 2017)

1.1.2 The current state of affairs

Among all the existing methods for the design of a laterally loaded pile, the *p-y* load transfer method is the most widely used. The basis of this method is the Winkler model, with the pile being modelled by a series of beam elements and the soil being represented by a series of non-interacting, non-linear springs distributed along the pile. The *p-y* curves are used to represent non-linear relationships between the net soil resistance (p) at a given depth per unit length and the lateral deflection of a pile at that depth (y) (Suryasentana & Lehane 2016). Figure 2 shows a schematic representation of the model described above, with the horizontal components of the soil response being modelled by *p-y* curves that vary depending upon soil conditions and depth.

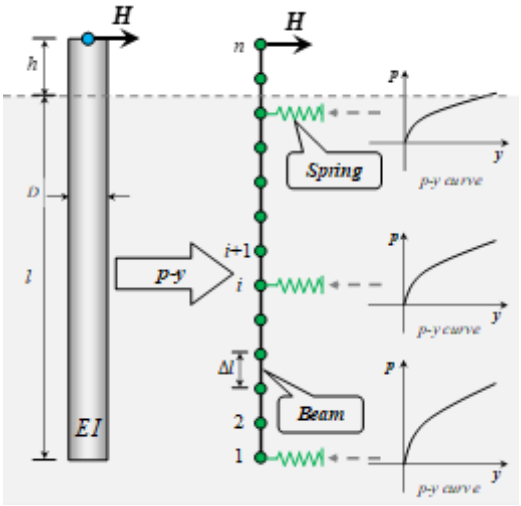

Figure 2: Winkler method for modelling lateral pile behavior

The *p-y* method in current design guidelines API (2014) and DNV GL (2013) were proposed based on a series of field tests performed by Reese, et al. (1974) and has been used in the oil and gas industry for many decades, . There are, however, a number of problems with this method. First of all, its applicability to large-diameter monopiles is uncertain because it was derived from test results on small-diameter ones (D=0.61 m, L/D=34.4). This has become especially relevant with the increasing use of large-diameter monopile foundations for offshore wind turbines. Choo & Kim (2015) have previously shown that for large-diameter piles, the API method predicts a stiffer than observed *p-y* response, especially for the initial stiffness. This overestimation of the soil stiffness can lead to unconservatism in pile design and is therefore not safe. Additionally, offshore wind turbine design requires accurate predictions of pile stiffness at small deflection and rotation. This means that the inaccuracy of the initial stiffness in the API model makes it less suitable for *OWT* foundation design.

Furthermore, the API (2014) uses the friction angle (φ') of a soil as the only input to define the *p-y* curves. In real projects, empirical correlations with in-situ test results (e.g. *CPT*, *SPT*) will be used to determine the sand friction angle. The uncertainties in those empirical correlations will further exacerbate the method's already high sensitivity to the chosen φ'.

Therefore, to avoid difficulties in selecting appropriate strength parameters and to properly model in-situ soil complexity, several researchers have suggested ways of using the tip resistance (q_c) from the cone penetration test (*CPT*) to determine the relationship between the soil resistance and the lateral deflection of a pile (i.e. p-y curves). Such approaches have the advantage that they are direct methods

that are not susceptible to the subjectivity associated with the inference of friction angle values (Suryasentana & Lehane 2016).

1.1.3 Aims & scope

The API method of deriving *p-y* curves and predicting lateral displacement behaviour of piles may produce suboptimal designs for short monopile foundations in general and offshore wind turbines specifically. This is because it was developed for flexible piles instead of large diameter rigid monopile foundations and because in practice it usually relies on uncertain correlations to derive necessary strength parameters. Performing finite element analyses (*FEA*) to derive *p-y* springs can lead to predictions that more accurately resemble measurements from pile load tests (*PLT*), but doing this for all offshore wind projects would be prohibitively time consuming and expensive (Byrne et al. 2017). Using *p-y* springs that can directly be defined from in-situ measurements may prove to be a convenient and cheap alternative.

Therefore, this research aims to systematically evaluate the performance of existing *CPT*-based *p-y* methods, as well as to experimentally validate an alternative method of modelling the response of rigid piles under lateral load. This is done by collecting and re-analysing experimental load-deflection results from existing literature and also performing additional centrifuge pile load tests in the TU Delft lab to obtain data from which *p-y* curves can be derived. All the tests are performed under a fully drained monotonic loading condition. Additionally in the course of these lab tests, the experimental methods used will be evaluated and improved upon. The measured load-deflection response and computed response at ground level are compared to qualitatively and quantitatively assess the performance of the different *CPT*-based *p-y* models in Part 2 and 4. Subsequently, the experimental methods are outlined and evaluated in Part 3. Finally the predicted *p-y* curves are produced and evaluated against the gathered experimental test data and the moment-rotation responses of the piles from the lab tests are unified through normalization in Part 4, to experimentally validate a simplified pile-soil interaction model for the laterally load rigid pile in sand.

1.2. Literature review

1.2.1 Monopile design principles

The American Petroleum Institute originally developed its p-y method for use in the offshore oil- and gas industry. This means that it focused on the lateral pile behaviour of the long and slender piles used in the jacket foundations of offshore platforms, as opposed to the shorter and broader monopile foundations of offshore wind turbines. There are important differences in the design considerations of these two structures.

The foundations of both jacket platforms and wind turbines have to resist a vertical load from the respective structures themselves, as well as varying horizontal loads from the environment actions in the form of winds, waves and currents. However, compared with a platform which is relatively heavy and produces a great vertical load while resting atop multiple piles, an offshore wind turbine is relatively light and stands atop a single pile. As can be seen in Figure 3, this leads to differences in the way that loads are transferred to the structure's foundation. For offshore wind turbines, the horizontal force is comparable to the vertical loads with additional huge overturning moment, where the vertical load of an offshore platform is usually an order of magnitude larger than the lateral force (Byrne & Houlsby, 2004). As a result, jacket pile design mainly considers (vertical) axial loading, whereas monopile design is mainly concerned with lateral loading and overturning moments (Hoving, 2016).

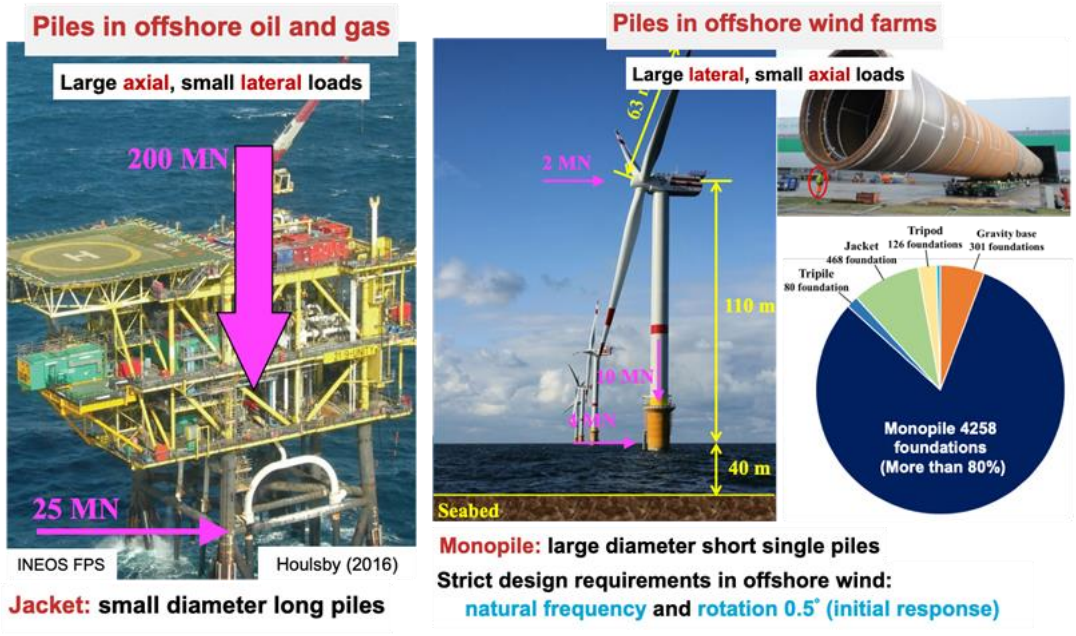

Figure 3: Typical loads on an OWT with monopile foundation (left) and a jack-up rig (right)

Another design consideration for monopile foundations concerns cyclic loading. The aforementioned wind- and wave actions come in the form of periodic loads, which vary in frequency and intensity. This is also goes for operational loading, which in this case comes from the rotation of the wind turbine rotor blades. These cyclic loads induce a dynamic response in the turbine, which can be especially damaging if the frequency of the cyclic loads matches the natural frequency of the structure, leading to resonance. As a consequence, it is of great importance that offshore wind turbines are designed such that their natural frequencies fall outside of the ranges of frequencies imposed upon them by environmental- and operational loads. An illustration of this is given in Figure 4. The natural frequencies of wind turbines depend strongly on both the material properties of the structure and on the stiffness of the soil surrounding the foundation. Because of this and the relatively high uncertainty in soil properties, it is essential that soil stiffness is accurately modelled in order to prevent failure (Arany, et al., 2014).

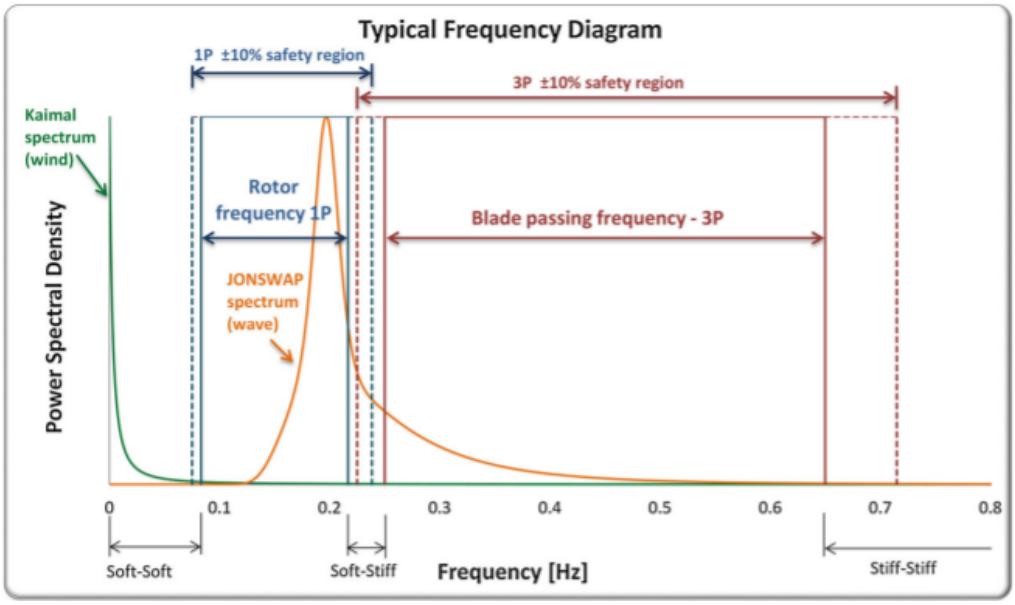

Figure 4: Typical frequency ranges of wind, wave and operational (1P & 3P) loads on OWT's (Arany, et al., 2014)

In DNV-OS-J101 (2014), four design limit states are described that should be avoided in order to ensure proper safety and performance of offshore structures. According to this guideline, each design limit state has specific criteria pertaining to certain loads, displacements or rotations. These criteria vary depending upon the load scenarios, the function of the structure and the type of foundation it is built upon. The three limit states that are considered to be most important in the design of offshore wind turbines are described in Table 1.

Table 1: Important limit states for offshore monopile foundations

Design criterion	Description
Ultimate limit state (ULS)	The ultimate limit state corresponds to the maximum load capacity that a structure's foundation can withstand before failure occurs. Due to the hardening response of monopile foundations in sand, it is difficult to obtain the ultimate geotechnical capacity of the monopile since a large deflection is required to mobilize it. Normally for a monopile, the pile resistance at a ground displacement y_0 of 10% of the pile diameter or a groundline rotation θ_0 of 2° is defined as the bearing capacity (Byrne, et al. 2015b).
Serviceability limit state (SLS)	The serviceability limit state corresponds to the usability of the structure and is usually related to the maximum displacement or rotation of the foundation. According to the design code, the largest rotation of the monopile should be less than 0.5°, including the 0.25° rotation from possible installation misalignment.
Fatigue limit state (FLS)	The fatigue limit state corresponds to the cumulative damage from repeated loading of an offshore structure. It is not related to the maximum load capacity, because repetititve loading can cause the structure to fail long before the maximum load capacity is reached. The maximum fatigue limit stress depends on both the stress magnitude in the structure and the frequency of the load (load cycles).

Traditionally, the various *p-y* methods used in offshore oil and gas are more focused on the avoidance of the *ULS* of offshore structures. However, since offshore wind turbines are long, slender, dynamically sensitive structures with strict requirements regarding the system's deflection, the *SLS* and *FLS* are more dominant for foundation design. Therefore, besides the pile capacity it is worthwhile to evaluate the performance of existing *p-y* models in predicting the lateral response of laterally loaded piles at small deflections.

1.2.2 Static lateral pile behaviour

Under static loading conditions, the soil surrounding a laterally loaded pile exerts an increased force in the opposite direction of the load, leading to increased soil stresses on one side of the pile. This is the passive soil reaction and it occurs on the side of the pile opposite the lateral load (*H*). Where the passive reaction leads to increased soil stresses compared to the situation before lateral loading, the active soil reaction on the other side of the pile leads to decreased soil stresses. This is because the soil on the active side can expand into the space opened up by the pile. A plan view visualization of the radial stresses around a laterally loaded pile is shown in Figure 5.

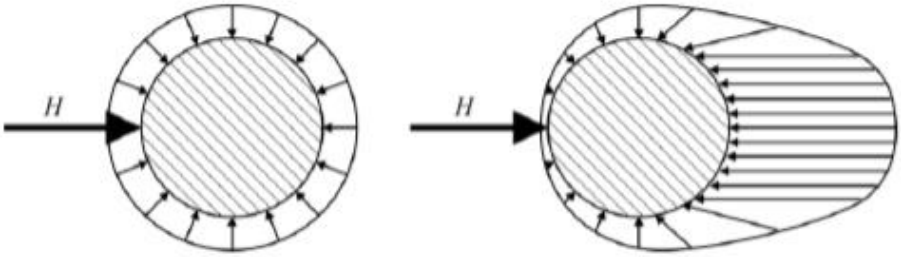

Figure 5: Soil stresses surrouding a pile before- and after application of horizontal load (Janoyan & Whelan, 2004)

As shown in Figure 6 (left), the passive soil stress acting against the horizontal load can be decomposed into a normal stress component acting on the front of the pile and a shear stress component acting on the sides. Because the active soil stress is negligibly small (as can be seen in figure 5), it is not taken into account. In the API- and other *p-y* methods, the soil stress *P* is normally simplified so that the shear stress component is incorporated into one stress that acts normally on the pile (as shown in the right of Figure 6).

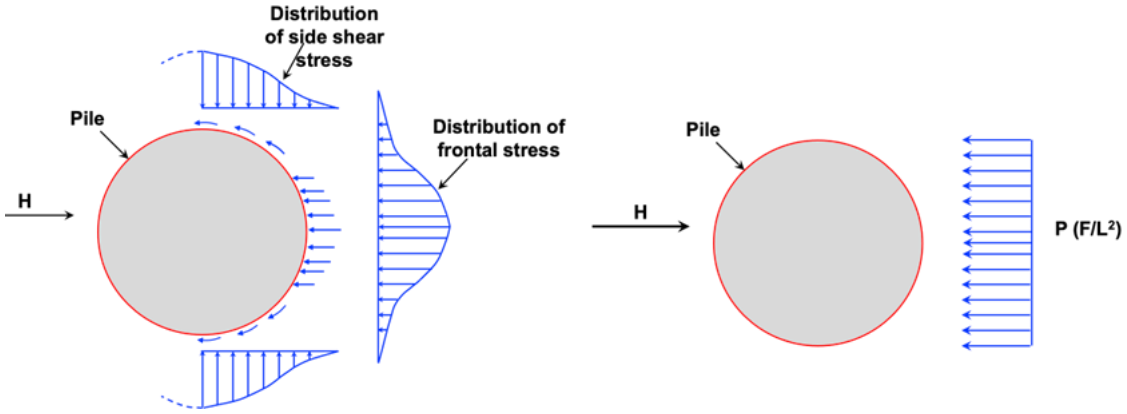

Figure 6: (left) actual distribuition of soil stresses under lateral load, (right) simplified soil stress after (Baguelin, et al., 1977)

A soil reaction (*p*) profile shows the variation in lateral soil stress increase due to a horizontal load, along the depth of a pile foundation. If the integral of the soil stress profile equals the applied load, the foundation is in equilibrium. For a flexible pile, the soil resistance profile theoretically looks like the one shown in Figure 7.

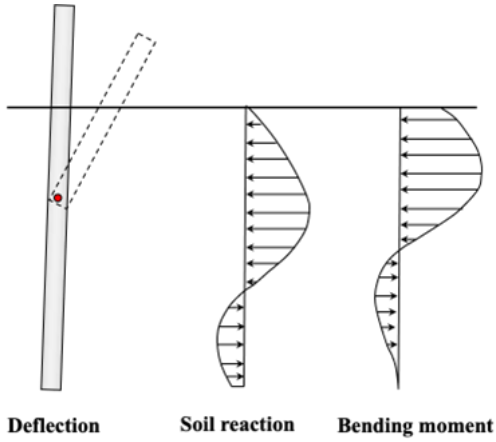

Figure 7: Soil resistance profile for flexible piles under lateral load

1.2.3 The *p-y* load-transfer method

The Winkler spring model

In order to calculate the pile displacement at a given load, a relationship for the soil reaction can be defined in a pile-response model. The Winkler model is a basic and well-known method of simulating the soil reaction for a laterally loaded pile. In this method the pile is represented in a simplified way as a series of beam elements. Each beam element is then connected to a soil spring, which acts on the pile independently of the other springs. These individual springs are called *p-y* springs and their behaviour is governed by *p-y* curves, that define the relationship between the net soil pressure *p* and the lateral displacement *y*. Originally, the soil was assumed to be perfectly elastic and the soil stiffness was defined as a sub-grade reaction modulus (*Kpy*) that is constant according to *Kpy = p/y*, which leads to a linear *p-y* curve.

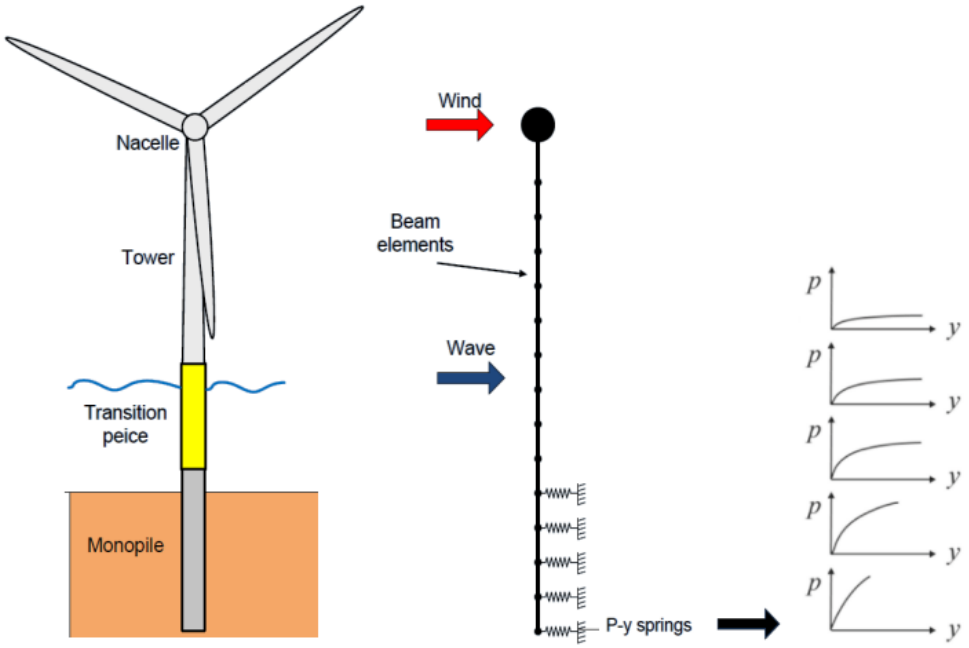

Figure 8: P-y method applied to a typical OWT after Liingaard (2013)

The assumption that soils are perfectly elastic is obviously not realistic, so in order to capture non-linear soil behaviour an updated *p-y* method was put forward by McClelland & Focht in 1958. In this method, the constant soil spring stiffness is replaced by a stiffness that decreases with an increasing pile displacement. Furthermore, it introduces an ultimate soil pressure (p_u) beyond which the pressure cannot increase, while increases in displacement will continue. Because the maximum soil pressure is dependent upon local soil characteristics, the *p-y* curves are depth-specific. Figure 8 shows a typical design for an offshore wind turbine and its simplified beam-spring model with corresponding *p-y* curves.

As mentioned before, the pile is represented as a beam and this is usually (including this study) done according to Euler-Bernoulli beam theory. In this theory, a lateral load induces bending moments and shear forces on the pile internally- and lateral soil pressure externally. These are governed by the following Equations:

$$\theta = \frac{dy}{dz} \qquad (1)$$

$$M = -EI\frac{d^2y}{dz^2} \tag{2}$$

$$V = -EI\frac{d^3y}{dz^3} \tag{3}$$

$$p = -EI\frac{d^4y}{dz^4} = E_{py}y \tag{4}$$

In these Equations, *y* is the displacement at depth *z*, *M* is the bending moment, *V* is the shear force, *p* is the soil resistance per unit length, *EI* is the flexural rigidity and θ is the rotational slope of the beam. A deforming beam element according to Euler-Bernoulli beam theory can be seen in Figure 9. This model does not incorporate vertical shear forces. Previous research by Byrne et al. from 2017 has shown that the vertical shear forces under lateral load are relatively insignificant in comparison to the bending moments for long piles (*L/D*>10) and can therefore be neglected, however this is not the case for intermediate (3<*L/D*<6)- and short piles (*L/D*<3).

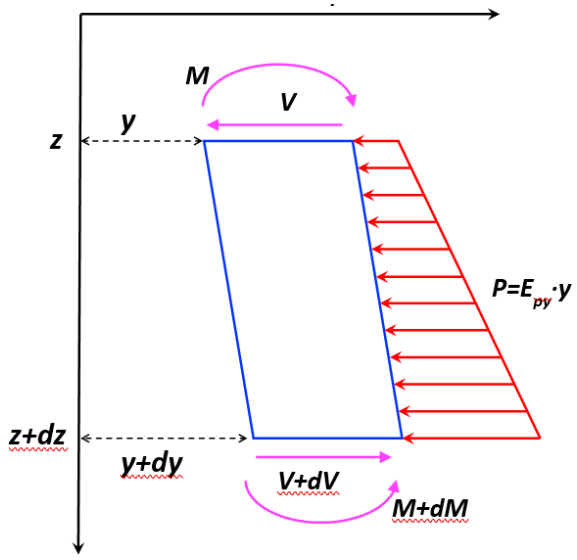

Figure 9: Deforming Euler-Bernoulli beam element

Derivation of *p-y* springs

Traditionally, pile load tests are performed in the field on prototype scale piles at a target site to produce *p-y* curves that can be used to make accurate load-displacement predictions for that site. During such a test, a range of increasing load increments is applied to the pile, whilst several instruments measure the pile displacement and deformations. A soil pressure profile can be constructed from strain gauge measurements and together with the pile displacements these can be used to construct depth-dependent *p-y* curves. This process is also applied for pile load tests in a geotechnical centrifuge. The method of obtaining soil pressure profiles is detailed below.

First, the measured strain data are used to calculate the curvature and the bending moment:

$$\text{Curvature} \qquad \varphi = \frac{\varepsilon_{compression} - \varepsilon_{tension}}{D} \tag{5}$$

$$\text{Moment} \qquad M = \varphi EI \tag{6}$$

Here $\varepsilon_{compression}$ and $\varepsilon_{tension}$ are the measured strains on the compressed and extended sides of the pile respectively and *EI* is the flexural rigidity of the pile. By performing either double differentiation or integration, respectively the pressure- and displacement profiles can be determined:

$$\text{Displacement} \qquad y = \iint \varphi dz + \theta_0 z + y_0 \tag{7}$$

$$\text{Soil pressure} \qquad p = -\frac{d^2M}{dz^2} \tag{8}$$

Here *z* is the depth along the pile, θ_0 is the ground rotation and y_0 is the ground displacement. θ_0 and y_0 can both be derived from linear variable differential transformer (*LVDT*) measurements. A schematic overview of the method can be seen in Figure 10.

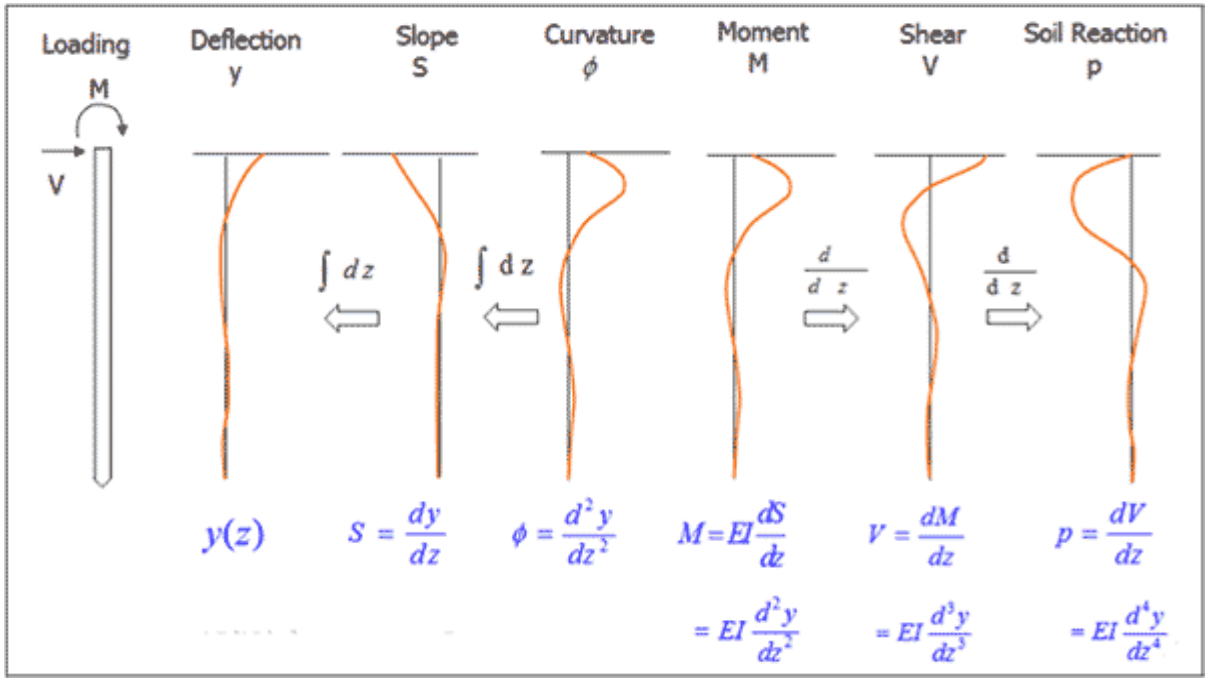

Figure 10: Derivation of horizontal pile deflection (y) and soil resistance (p) (Lemnitzer, 2013)

1.2.4 Overview *p-y* methods

As mentioned previously, *p-y* springs can be derived for a specific location using full scale pile load tests, or alternatively it can be done through 3D *FE* testing. However, this is a time-consuming and expensive process, which means that it is not feasible in practice to apply this process in every project. Therefore, empirical generalized *p-y* methods have been conceived to make predictions of lateral pile displacements. There are a number of empirical methods for relating the displacement at a given depth to the soil pressure, with the API method recommended by the American Petroleum institute and Det Norske Veritas (DNV) standards being the most widely used. This method uses as its main input and main measure of soil strength the internal friction angle (API, 2011).

API

The API method was originally conceived by Reese et al. (1974) from a series of field tests at Mustang Island, USA and consists of a *p-y* curve defined by four parts. The first is a straight part through the origin, the second is a parabolic section and the third- and fourth parts are again straight lines. The following Equations describe the four sections:

Section 1: $$p = K_{py} z y \tag{9}$$

Section 2: $$p = C y^{\frac{1}{n}},\ C = \frac{p_m}{y_m^{\frac{1}{n}}},\ n = \frac{p_m}{m y_m} \tag{10}$$

Section 3: $$p = my,\ m = \frac{p_u - p_m}{y_u - y_m} \tag{11}$$

Section 4: $$\text{for } y \geq \frac{3b}{80},\ p = p_u \tag{12}$$

Here *z* is the depth along the pile, *y* the horizontal displacement and *b* the pile diameter. Variables p_m, y_m, p_u and y_u are indicated in Figure 11.

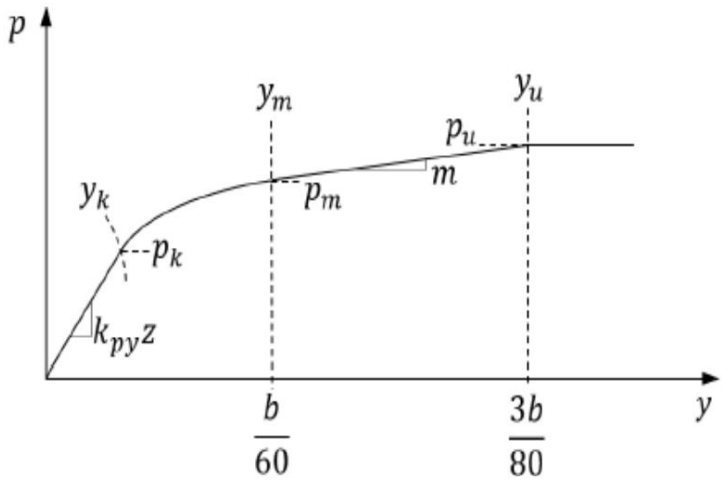

Figure 11: p-y curve for sand after Reese et al. (1974)

Because there are different failure modes of the soil near the surface and at depth, the ultimate soil pressure p_u from the *p-y* curve is depth-dependent. Figure 12 shows the two failure modes, with a wedge failure mode occurring near the surface and a deep horizontal flow failure at greater depth.

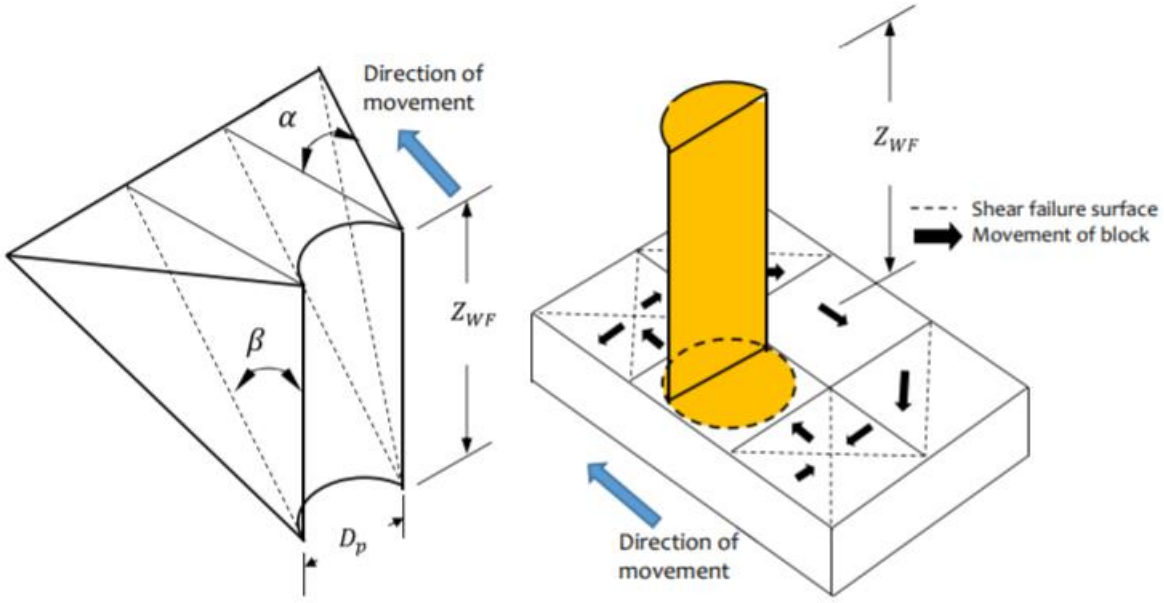

Figure 12: Two soil failure modes (Ammar Bouzid, 2018)

An updated method for calculating the ultimate soil pressure in cohesionless soils was produced by Borgard & Matlock (1980), using Equations 13, -14 and -15. From the two values for p_{us} and p_{ud}, the smallest is taken to be the ultimate soil pressure. The values for the coefficients *C1, C2* and *C3* can either be derived from Figure 13 using *φ'*, or they can be calculated using formulas from (API, 2011).

$$p_{us} = (C_1 z + C_2 D)\,\gamma' z \tag{13}$$

$$p_{ud} = C_3 D \gamma' z \tag{14}$$

$$p_u = \min\,[p_{us}; p_{ud}] \tag{15}$$

Here *γ'* is the effective volumetric soil weight, *z* is the depth and *D* is the pile diameter.

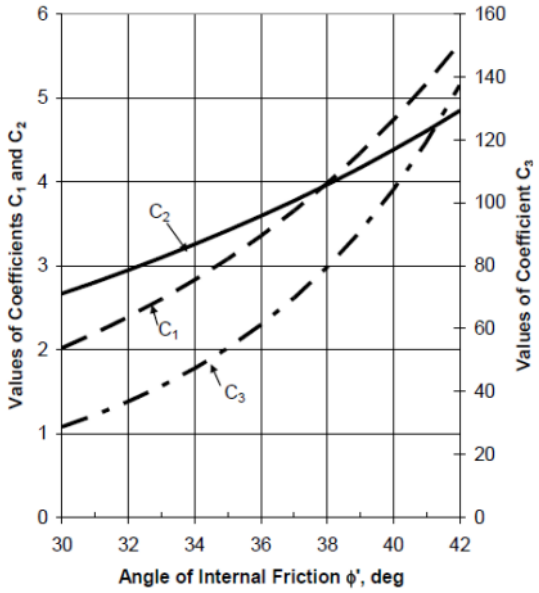

Figure 13: Curves for coefficients C1, C2, and C3 as a function of the angle of internal friction φ' (API, 2011)

The *p-y* method that is included in the current API guidelines (API, 2011) and that has therefore become the standard approach for the prediction of lateral pile displacements in cohesionless soils, is a method published by O'Neill & Murchison in 1983. They put forward a simpler *p-y* curve that consists of one hyperbolic tangent function, as shown in Equation 16. In this function, p_u is calculated according to Equations 13 through 15 and the initial tangent stiffness k_1 is taken from

Table 2.

$$p = A\, p_u \left[\frac{kz}{Ap_u} y\right] \tag{16}$$

$$A = \left(3.0 - 0.8\frac{z}{D}\right) \geq 0.9 \text{ for static loading} \tag{17}$$

Table 2: Initial stiffness (API, 2011)

φ' [degrees]	**K_1 [MN/m^3]**
25	5.4
30	11
35	22
40	45

The API *p-y* method was originally derived from the results of field tests on small diameter (D = 0.61m) piles with large aspect ratios (L/D = 34.4). It has previously been found to provide good predictions for piles with D < 2m in comparable soil conditions as those at Mustang Island by Peralta (2010). However, as the DNV guideline on monopile design in DNV-OS-J101 (2014) states, the predictions from this method can be less accurate for large diameter piles.

CPT-based *p-y* methods

As mentioned previously, in the industry standard API method the angle of internal friction φ' is used to define the soil strength. In practice, this friction angle is determined indirectly through empirical correlations with the results of in-situ tests (e.g. *CPT*, *SPT*). Therefore, the high sensitivity of the results from the API method to the chosen φ' is made worse the uncertainties in those correlations (Suryasentana & Lehane, 2016).

In order to avoid difficulties in the selection of the appropriate strength parameters, several methods of directly relating in-situ test results to *p-y* curves have been proposed. They make use of the cone penetration or '*CPT*' test, which is the most common test globally for determining soil parameters and -layers. While an instrumented cone is pushed through the soil, the total resistance force on the cone tip (q_c) and the friction along the cone sleeve with the soil (f_s)are measured. Because the influences of the rigidity and compressibility of a soil medium, as well as that of the mean effective stress on the cone are comparable to those on a pile, the cone penetrometer is a good analogue for a miniature pile foundation (Wrana, 2015; Ardalan, et al., 2009).

Salgado & Randolph (2001) performed a series of numerical analyses and concluded that the cone tip resistance depends both on horizontal stress, the sand friction angle and the sand's stiffness characteristics. Similarly, the performance of laterally loaded pile is also governed by the horizontal soil stress, the sand friction angle and the sand's stiffness characteristics. Therefore, it is reasonable to correlate the *p-y* curve of a laterally loaded pile with the measured in-situ cone tip resistance of a

cone penetration test. Also for this reason, q_c values are often used to normalize site-specific soil parameters (Novello, 1999; Houlsby & Hitchman, 1988). A typical test setup and cone for a *CPT* test are presented in Figure 14.

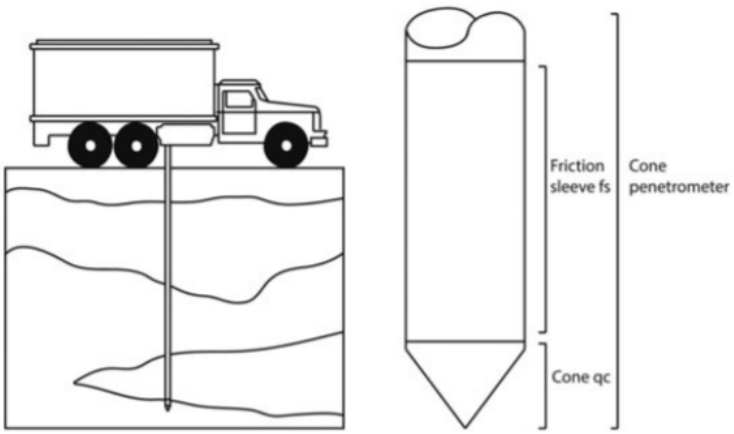

Figure 14: (a) Typical CPT setup in the field (Rose et al. 1996); (b) Schematic cone design (Lunne et al. 1997)

Novello

Novello (1999) proposed a simple *CPT*-based expression to predict *p-y* curves where the soil pressure p is a function of D (m), the effective volumetric weight γ' (kN/m^3) and z (m). The expression is based on both centrifuge- and field tests performed in Bass Strait calcareous sands. The field tests concerned free-headed piles, one of which had a diameter of 2.137 and was driven to a depth of 31.5m, whereas the other one had a 0.365m diameter and was driven to 6.1m and 31.5m. By performing a regression on the *PLT* data using a power-law model, Equation 18 was found to provide a good fit to the test results. An summary of the method by Novello (1999) is given in Table 3.

$$p = \min\left(2D(\sigma_v')^{0.33}(q_c)^{0.67}\left(\frac{y}{D}\right)^{0.5}, Dq_c\right) \tag{18}$$

Table 3: Summary p-y method Novello (1999)

Developed in	1999
Derived from	Model scale *PLT* from Williams, et al. (1988) & centrifuge tests from Wesselink et al. (1988)
Soil conditions	Calcareous sands from the Bass Strait, Kingfisher B- and Halibut A locations specifically
Pile type(s)	Free-headed & driven steel pipe
Pile geometries	D: 2.137m & 0.356m; L/D: 14.7 & 17.1

Dyson & Randolph

A similar method based on a power-law model was developed by Dyson and Randolph (2001), with additional consideration for installation method, pile head restraint conditions and rate of loading. The method is based on a series of centrifuge *PLT's* at 160*g* in calcareous sands originating from the Australian North-West Shelf. For free head conditions, Dyson and Randolph found Equation 19 to be a good fit to the test data.

$$p = 2.84D(\gamma' D)\left(\frac{q_c}{(\gamma' D)}\right)^{0.72}\left(\frac{y}{D}\right)^{0.64} \quad (19)$$

Table 4: Summary p-y method Dyson & Randolph (2001)

Developed in	2001
Derived from	Centrifuge tests (160g)
Soil conditions	Calcareous sands from the North-western continental shelf of Australia, water table: ground level, γ': 8.1kN/m^3, φ_{cv}: 38°
Pile type(s)	Free-headed aluminium pipe, jacked at 1g
Pile geometries	*D*: 2.080m; *L/D*: 26.15

Li et al.

In 2014, Li, et al. conducted a study in which the performance of previously developed *CPT*-based *p-y* methods was assessed and in which a new formulation was proposed. The dataset on which the new expression was based contains a set of field *PLT's* that were performed in siliceous sand on six open-ended piles of varying dimension, four being flexible and two being rigid. The test sites were at Blessington, Ireland, with soil conditions as shown in

Table 5. The new formulation proposed in this study can be seen in Equation 20.

$$p = 3.6D(\gamma' D)\left(\frac{q_c}{\gamma' D}\right)^{0.72}\left(\frac{y}{D}\right)^{0.66} \quad (20)$$

Table 5: Summary p-y method Li et al. (2014)

Developed in	2014
Derived from	Field tests at Blessington, Ireland
Soil conditions	Calcareous sands from the North-western continental shelf of Australia, water table: ground level, γ': 8.1kN/m^3, φ_{cv}: 38°
Pile type(s)	Free-headed aluminium pipe, jacked at 1g
Pile geometries	6 piles with *D*: 0.34m, *L/D*: 6.5-20.6

Suryasentana & Lehane 2014

Suryasentana & Lehane (2014) presented a more or less generalized method for the response of piles in sands under lateral load. A series of 3D Finite Element Analyses (carried out with Plaxis 3D and Oasys ALP), using the Hardening Soil (*HS*) constitutive model was carried out to derive the *p-y* curves. Rigid-

and flexible piles of varying diameter (0.5-5 m) were studied in both loose- and dense sands with varying strength- and stiffness parameters. The piles were installed by 'wishing in place', meaning that installation effects were not considered. The *CPT*-profiles for the various sands were generated numerically using a cavity expansion analogue with the *HS* model.

Consequently, a non-linear regression analysis was performed to determine the parameters of a power-law model that fit the computed data. In order to correct the overprediction of soil stiffness at large loads, the expression was given a limiting character and was recast into an exponential form, according to Equation 21.

$$p = 2.4\sigma_v' D \left(\frac{q_c}{\sigma_v'}\right)^{0.67} \left(\frac{z}{D}\right)^{0.75} \left(1 - exp\left(-6.2\left(\frac{z}{D}\right)^{-1.2}\left(\frac{y}{D}\right)^{0.89}\right)\right) \quad (21)$$

Since the above method was derived from a set of computer simulated *PLT*'s, it was also applied to a number of real-world cases to assess the accuracy of its *p-y* predictions. The results from this comparison were generally good, which is promising for the use of *CPT*-based *p-y* methods in the case of laterally loaded piles in sand.

Table 6: Summary p-y method Suryasentana & Lehane (2014)

Developed in	2014
Derived from	*PLT* & *CPT* data from 3D- and 2D *FEA* respectively
Soil conditions	10 parameters hardening-soil model, φ': 36°-51°, relative density: 28-97%
Pile type(s)	Linear elastic solid pile, E_p: $2.4*10^7$ kPa
Pile geometries	10 piles with *D*: 0.5-5m

Suryasentana & Lehane 2016

In 2016, Suryasentana & Lehane further improved the method using the same 3D *FE* model in Suryasentana & Lehane (2014) to addresses a number of limitations of the original version. An initial stiffness is defined according to the small strain shear modulus (G_{max}), as seen in Equation 23. The influence of the bending stiffness of the pile was also assessed by conducting additional simulations on four piles of varying flexural rigidities (E_pI_p), one of which is classified as rigid according to the Poulos & Hull (1989) criterion. Previous research is conflicted on the influence of flexural rigidity on *p-y* curves. Ashour & Norris (2000) for example concluded that ultimate resistance and stiffness of the soil response increase with increasing E_pI_p, when Fan & Long (2005) concluded that the *p-y* response is generally independent of the rigidity.

Suryasentana & Lehane (2016) concluded that the *p-y* response is independent of E_pI_p for piles in both loose- and dense sands. However, this was only assessed at depths of 1 and 2 m below the ground surface and it is therefore unsure whether this holds true for the entire depth along a pile. The influence of water table depth was also assessed for a fully saturated condition and a condition with the water table at *z/D* = 1.5. It was concluded that the same ultimate resistance is reached above and below the water table, but that the response is stiffer under unsaturated conditions and that the ultimate resistance is reached at lower displacements. This can be accounted for by factoring the normalised displacement (*y/D*) by the following equation:

$$\eta_w = \left(\frac{\sigma_v - u_g}{\sigma_v^{'}}\right)^{0.5} \quad (22)$$

where σ_v and σ'_v are the total- and effective vertical stresses respectively and u_g the water pressure at ground level. Another factor was also proposed to account for square pile cross sections as opposed to circular ones. All of these additions finally resulted in the method outlined in Equations 23 through 26.

$$p = 4.5G_{max}y \quad y/D \leq 0.0001 \quad (23)$$

$$p = p_u f(y) \qquad y/D \geq 0.01 \quad (24)$$

$$f(y) = 1 - exp\left[-8.9\left(\frac{y}{D}\right)\left(\frac{\sigma_v - u_g}{\sigma_v'}\right)^{0.5}\left(\frac{z}{D}\right)^{-1.25}\right] \quad (25)$$

$$p_u = 2.4\sigma_v' D\left(\frac{q_c}{\sigma_v'}\right)^{0.67}\left(\frac{z}{D}\right)^{0.75} \leq q_c D \quad (26)$$

Table 7: Summary p-y method Suryasentana & Lehane (2016)

Developed in	2016
Derived from	*PLT* & *CPT* data from 3D- and 2D *FEA* respectively
Soil conditions	Loose sand, D_r: 0.28, γ': 11kN/m^3, φ': 36.1 Dense sand, D_r: 0.79, γ': 11kN/m^3, φ': 45.2
Pile type(s)	Linear elastic solid piles, 3 flexible & 1rigid, E_p: 30*10^5-30*10^7 kPa
Pile geometries	4 piles with *D*: 0.5-2m, *L/D*: 5 or 20

Overview and comparison *CPT*-based *p-y* methods

A condensed overview of all the aforementioned *p-y* methods is shown in Table 8. Comparing the methods against each other, a number of things stand out. Firstly, the datasets that the methods of Novello (1999), Dyson & Randolph (2001) and Li et al. (2014) were derived from do not contain broad ranges of *PLT*'s that are representative for both flexible- and rigid piles. In the case of Novello (1999), only three tests were performed at a single location, with an aspect ratios ranging from 14.74 to 86.30. The dataset from Dyson & Randolph (2001) again does not contain varying soil conditions and only has piles with an aspect ratio of 26.15. Finally, the piles in the study by Li et al. (2014) did vary in aspect ratio and rigidity (with one pile being classified as rigid). However, though the soil conditions at the two test sites are mostly representative of European offshore conditions (i.e. dense siliceous sands), there is little variation in soil conditions and only six tests were performed. Using 3D *FEM* modelling Suryasentana & Lehane (2014;2016) were by contrast able to perform a larger and more varied set of *PLT*'s, with soil relative densities ranging between 28% and 97%. This is likely to make the methods by Suryasentana & Lehane (2014;2016) more generally applicable.

Additional to the aforementioned more general datasets, the methods from Suryasentana & Lehane incorporate a number of features that are not present in the three simpler, power-law based methods.

These include an ultimate soil resistance p_u, as well as an initial stiffness and a soil saturation factor in the case of the updated version. Furthermore, the two more advanced methods normalize the cone resistance q_c by the vertical effective stress instead of the effective volumetric weight multiplied by the pile diameter, which makes more sense. The study by Li et al. (2014) suggests that the method from Suryasentana & Lehane (2014) does indeed provide more accurate *p-y* predictions, with the simpler methods from Novello (1999) and Dyson & Randolph (2001) specifically underpredicting both the displacement- and rotation capacity of rigid piles.

Table 8: Overview API- and CPT-based p-y methods

Reference	**Methodology**	**Soil**	***p-y* method**
API (2011)	Field tests	Siliceous sand	$p = A\, p_u \left[\frac{kz}{Ap_u} y\right]$ $p_{us} = (C_1 z + C_2 D)\, \gamma' z$ $p_{ud} = C_3 D \gamma' z$ $p_u = \min\,[p_{us}; p_{ud}]$
Novello (1999)	Centrifuge tests	Calcareous sand	$p = 2D(\sigma'_v)^{0.33}(q_c)^{0.67}\left(\frac{y}{D}\right)^{0.5}$
Dyson and Randolph (2001)	Centrifuge tests	Calcareous sand	$p = 2.84D(\gamma' D)\left(\frac{q_c}{(\gamma' D)}\right)^{0.72}\left(\frac{y}{D}\right)^{0.64}$
Suryasentana and Lehane (2014)	Numerical	Sand	$p = 2.4\sigma'_v D\left(\frac{q_c}{\sigma'_v}\right)^{0.67}\left(\frac{z}{D}\right)^{0.75}\left(1 - exp\left(-6.2\left(\frac{z}{D}\right)^{-1.2}\left(\frac{y}{D}\right)^{0.89}\right)\right)$
Suryasentana and Lehane (2016)	Numerical	Sand	$p = 4.5G_{max}y \quad y/D \le 0.0001$ $p = p_u f(y) \quad y/D \ge 0.01$ $f(y) = 1 - exp\left[-8.9\left(\frac{y}{D}\right)\left(\frac{\sigma_v - u_g}{\sigma'_v}\right)^{0.5}\left(\frac{z}{D}\right)^{-1.25}\right]$ $p_u = 2.4\sigma'_v D\left(\frac{q_c}{\sigma'_v}\right)^{0.67}\left(\frac{z}{D}\right)^{0.75} \le q_c D$
Li et al. (2014)	Field tests	Siliceous sand	$p = 3.6D(\gamma' D)\left(\frac{q_c}{\gamma' D}\right)^{0.72}\left(\frac{y}{D}\right)^{0.66}$

In order to get a better grasp on some the differences between the various *p-y* methods, it is helpful to show some predictions for the case of a fictional typical *PLT*. The chosen case concerns a full scale monopile foundation for an offshore wind turbine for soil conditions that are typical in Northern Europe (an important simplification is that the soil is assumed to be a homogenous sand of constant relative density). All relevant parameters are shown in Table 9.

Table 9: Relevant parameters for fictional pile test case

D (m)	**L (m)**	**e (m)**	**Wt (m)**	**y_{0max}/D**	**E (GPa)**	**γ' (kN/m^3)**	**D_r**
8	40	10	0.1	1.375	210	10	80%

Furthermore, an (empirical) method is needed to derive a realistic q_c profile that can serve as input for the p-y model predictions. To this end, a method proposed by Schmertmann (1976) is used:

$$q_c = C_0 p_a \left(\frac{\sigma'_v}{p_a}\right)^{C_1} exp(C_2 D_r) \tag{27}$$

Here P_a stands for atmospheric pressure (taken as 98.1kPa), D_r for the sand relative density and C_0, C_1, C_2 are non-dimensional correlation factors. The values for the latter three (shown in Table 10) are taken from Jamiolkowski, et al. (2003), who did relevant *CPT* lab tests on three well-known types of silica sand.

Table 10: Non-dimensional correlation factors from Jamiolkowski, et al. (2003)

C_0	C_1	C_2
17.68	0.50	3.10

A MATLAB pile response model (further outlined in Section 2.2.1) is used to simulate load tests for this case and produce load-displacement curves. Additionally, *p-y* curves at several depths are calculated. Looking at Figure 15 a few things become clear. The relative difference in predicted load between the models increases with displacement. This is mainly due to the fact that the models from Novello (1999) and Dyson & Randolph (2001) predict a larger decrease in the stiffness of the pile behaviour under lateral load with increasing displacement than the other three. At groundline displacements of up to 0.04*D* the predicted loads are relatively comparable.

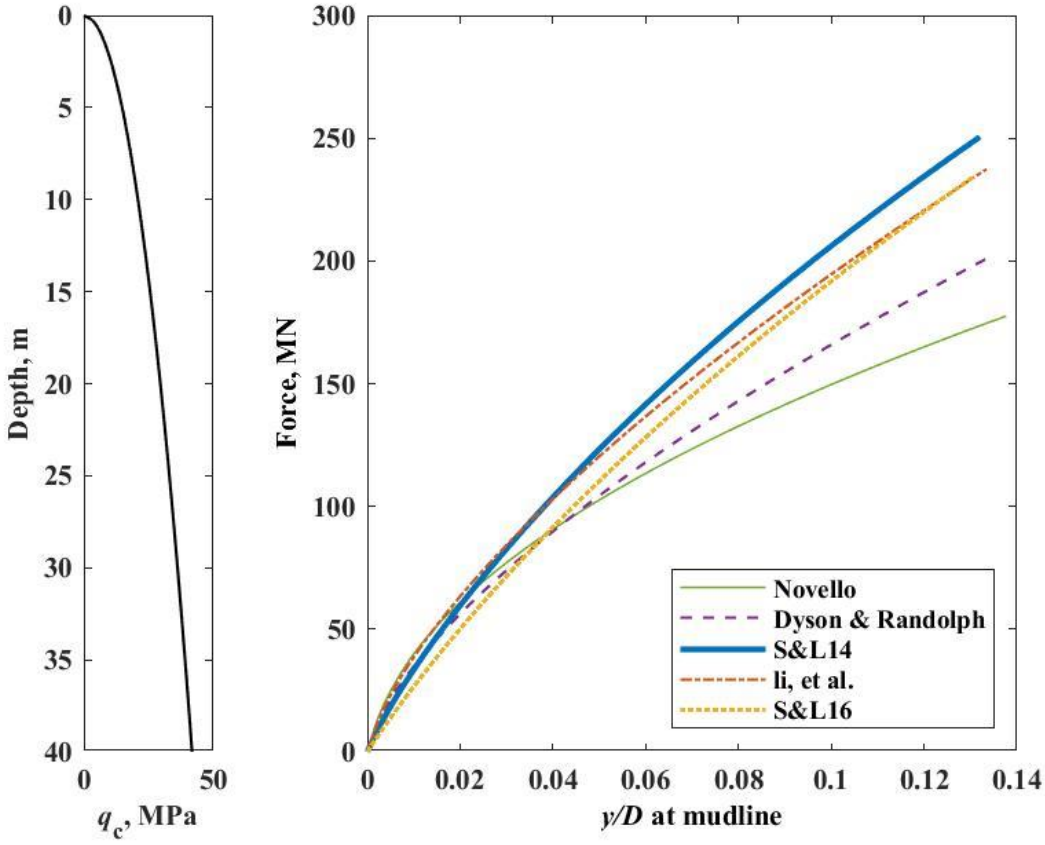

Figure 15: H-y response predicted by the CPT-based p-y models

Subsequently, predicted *p-y* curves are calculated for the previously described case using the five *CPT*-based *p-y* models at different depths, the results of which are shown in Figure 16. Looking at these results the first thing of note is that the predicted soil resistance varies wildly between methods, especially at large displacements. Furthermore, as with the *H-y* response, the method by Novello (1999) consistently predicts the weakest behaviour. The methods by Dyson & Randolph (2001) and Li, et al. (2014) predict a relatively large soil resistance at shallow depths (z<2D) and a relatively small resistance at greater depth. This is perhaps the opposite of what can be expected, since they both normalize the cone resistance by D instead of σ'_v. This means that the normalisation term does not increase with depth.

Additionally, the methods by Suryasentana & Lehane (2014;2016) mostly predict stronger soil behaviour up until the point where the ultimate resistance is reached. After this point their predicted resistance is again exceeded by those of the other methods. The two aforementioned methods clearly reach an ultimate soil resistance at shallow depths of 0.5*D* and 1*D*, but not at greater depth. Finally, the predictions from Suryasentana & Lehane (2014;2016) are very similar above the centre of rotation (located at *z*=3.75*D*) but they diverge below the centre of rotation, with the method by Suryasentana & Lehane (2014) predicting significantly stronger soil behaviour.

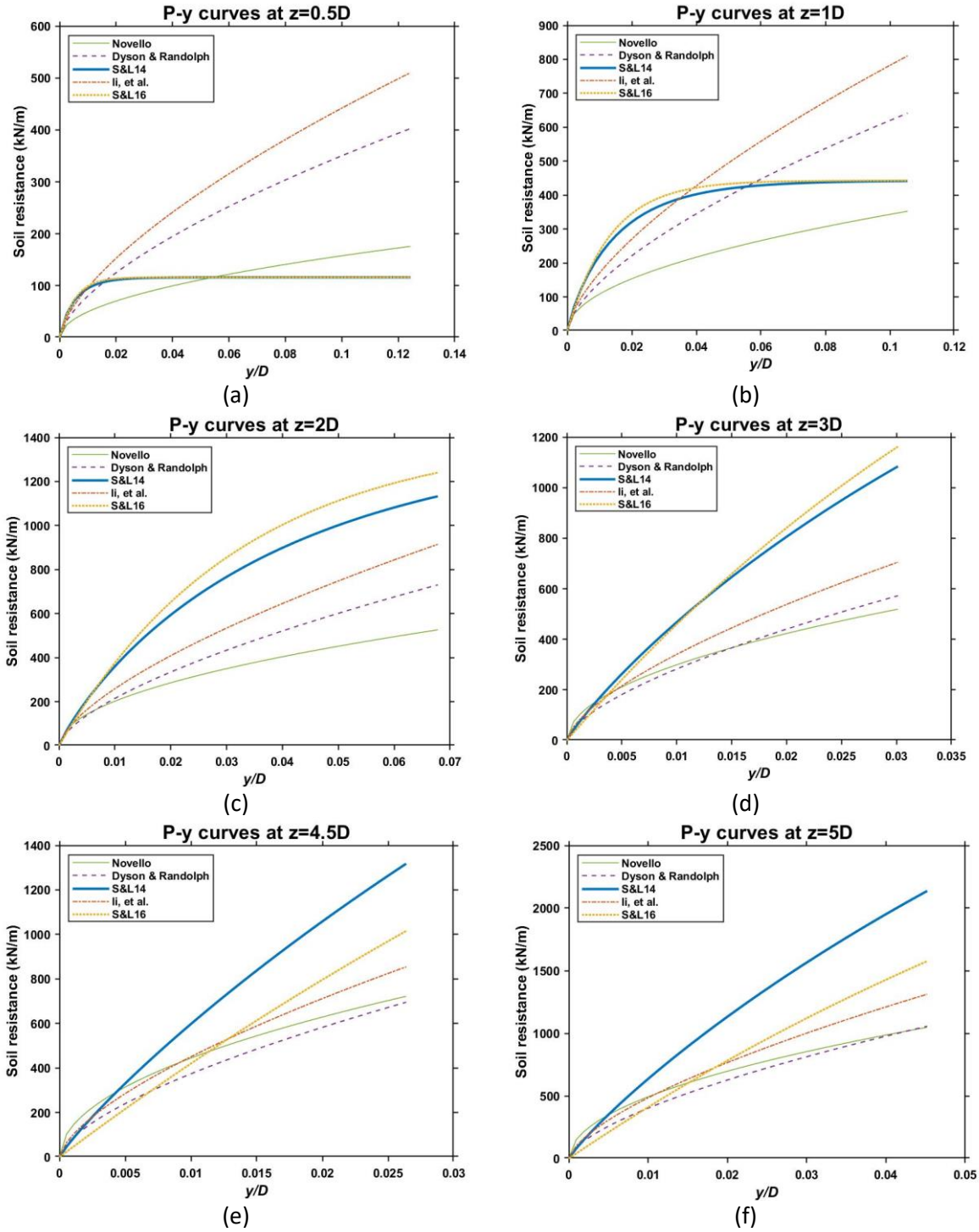

Figure 16: P-y curves for imaginary case at depths of 0.5-5D

1.2.5 Alternative design methods for the laterally loaded pile

PISA method

Short piles usually behave rigidly under lateral load. This means that they have a given point of rotation and that there is significant displacement at the pile tip. Therefore a moment and a shear force are developed at the base of the pile, which leads to inaccurate predictions for the pile head displacements when using traditional methods that rely solely on lateral soil pressures (Peralta 2010). In 1983 Davidson & Donovan used tests on laterally loaded drilled pier foundations (with aspect ratios

of 3.2 in sand and of 6.7 in clay) to produce a model with four soil reaction terms instead of just one, to better capture the behaviour of short piles.

Consequently, this model with additional soil reaction terms was used as the basis for an extended *p-y* method in the PISA project. Figure 17 (left) shows the four soil reaction terms for a pile loaded by a lateral force HG and moment MG that are incorporated in the PISA model, namely the distributed load, the distributed moment, the base shear and the base moment. Figure 17 (right) shows the same concept in a simplified 1D FE model. Relationships for the additional soil reaction terms were developed in the PISA project and the new method was proven to give more accurate predictions for the displacement of short piles than those based just on lateral soil pressure (Byrne, et al., 2015a). However, this method is relatively complicated with many parameters to calibrate and it may therefore not be the most convenient method to use.

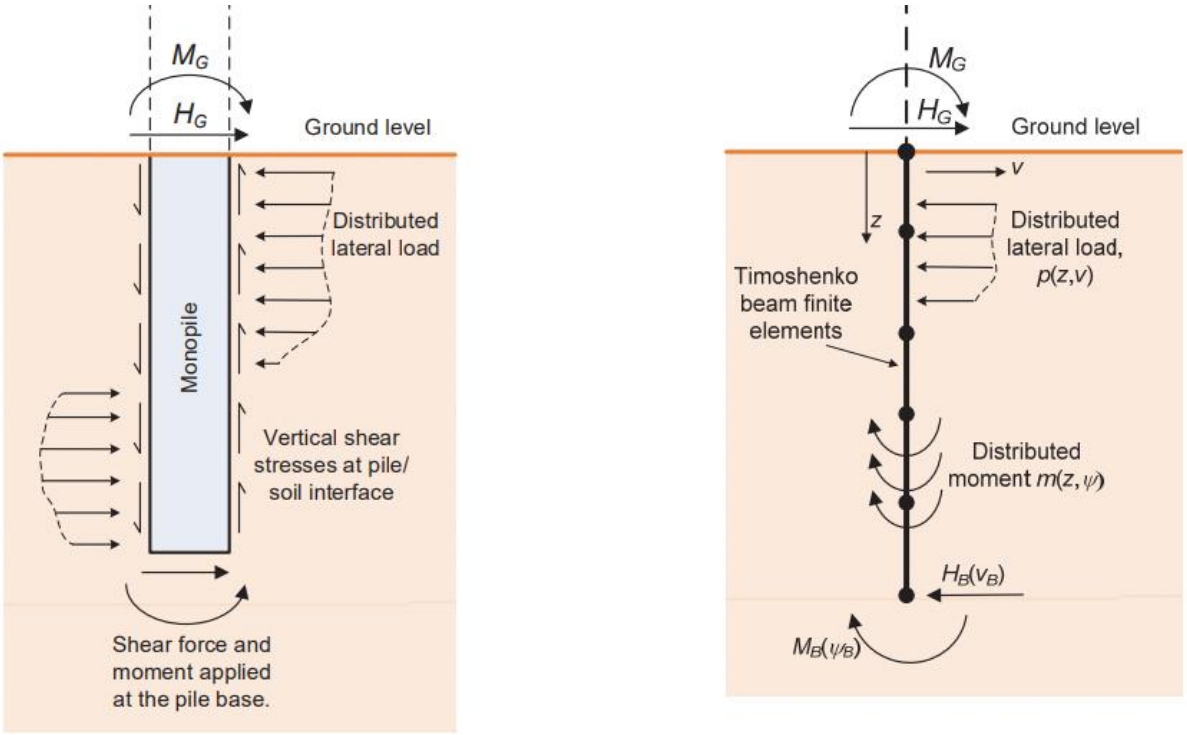

Figure 17: Conceptual (left) and 1D FE (right) model adopted in the PISA project (Byrne, et al., 2017)

Simplified pile-soil interaction for the rigid pile

A different approach from the *p-y* method to the modelling of the laterally loaded rigid pile in sand is proposed by Wang, et al. (2022) and makes use of the simplified pile-soil interaction illustrated in Figure 18 (Petrasovits and Award 1972; Leblanc et al. 2010). In this model the pile experiences a horizontal load (*H*) and consequently rotates around a single point located at depth (*d*). The lateral soil pressure (*P*) is defined according to the vertical effective stress and a net pressure coefficient (*K*). This simplified interaction model can help to unify the response of piles of varying dimensions loaded at varying eccentricities.

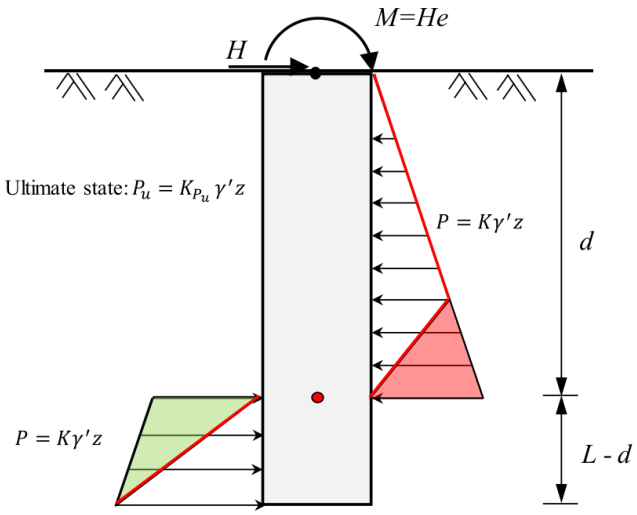

Figure 18: Simplified pile-soil interaction model from Wang, et al. (2022)

Richards, et al. (2021) showed that the stress dependency of the stiffness of the load-deflection response of a short pile under lateral monotonic loading can be successfully captured by the normalization method proposed by Leblanc, et al. (2010). Here the load (*H*) and the groundline displacement (y_0/D) are respectively normalized by ($DL^2\gamma'$) and ($p_a/L\gamma'$)$^\eta$, where η is related to the shear modulus and is generally taken at 0.5. Building upon this, Wang, et al. (2022) showed that the moment-rotation response relative to the rotation centre can be unified for piles of varying diameter and loading eccentricity (e) by taking the moment as $H(e + 0.75L)$ and normalizing it by ($DL^3\gamma'$). In this way, the effects on the rigid pile response under lateral load of stress level, pile diameter and loading eccentricity are accounted for. The depth of the rotation centre was found to vary slightly with the loading eccentricity, but a value of 0.75*L* was found to be sufficiently representative for all pile load tests. These conclusions were drawn using a set of *FEA* with load tests on piles with aspect ratios between 3-7.5 in a uniform medium dense sand (D_r = 0.65) represented by a hypoplastic model, with a range of loading eccentricities between 5-100m.

This method of characterizing the response of a laterally loaded pile is very simple and straightforward and has successfully been used by Wang, et al. (2022) as the basis of rotational spring model that uses only one moment-rotation spring located at the rotation centre to predict the pile response. A clear advantage of this approach over the PISA model is that it is much less complex, with only one spring to calibrate. However, it makes the important assumptions that the soil is drained and homogeneous and the assumed failure mechanism does limit the applicability of the method to rigid piles (which should make it relevant to the design of most *OWT* foundations). Furthermore, it was proposed based on a set of numerical simulations and has not yet been validated with empirical test results. This is done here using the results from the lab tests that are performed in the TU Delft geotechnical centrifuge.

Part 2. Evaluation of load-deflection predictions CPT-based p-y methods

2.1 PLT database

In order to evaluate the performance of the various CPT-based p-y methods, a pile load test (*PLT*) database was created with load-deflection data from a total of 39 tests. These *PLT*'s were gathered mainly from previous research and in the case of tests 32 through 39 from a new testing programme performed at the TU Delft geotechnical centrifuge. The test data gathered from the literature originates from 12 studies and concerns *PLT*'s conducted both in the field and in the lab. In total, the database contains 16 lab tests and 23 field tests. An overview of these *PLT*'s including all of their locations, soil conditions, pile dimensions and data sources is provided in Appendix B.

Data collection

For the tests in Wang et al. (2020) and the newly performed testing programme at the TU Delft, the original data could be accessed and used directly. For the other sources, the *CPT* profiles and load-deflection curves need to be extracted from the publications. In this regard, the online image analysis tool WebPlotDigitizer was used to obtain the datapoints from the curves in each paper (Rohatgi, 2021). Figure 19 shows the software interface.

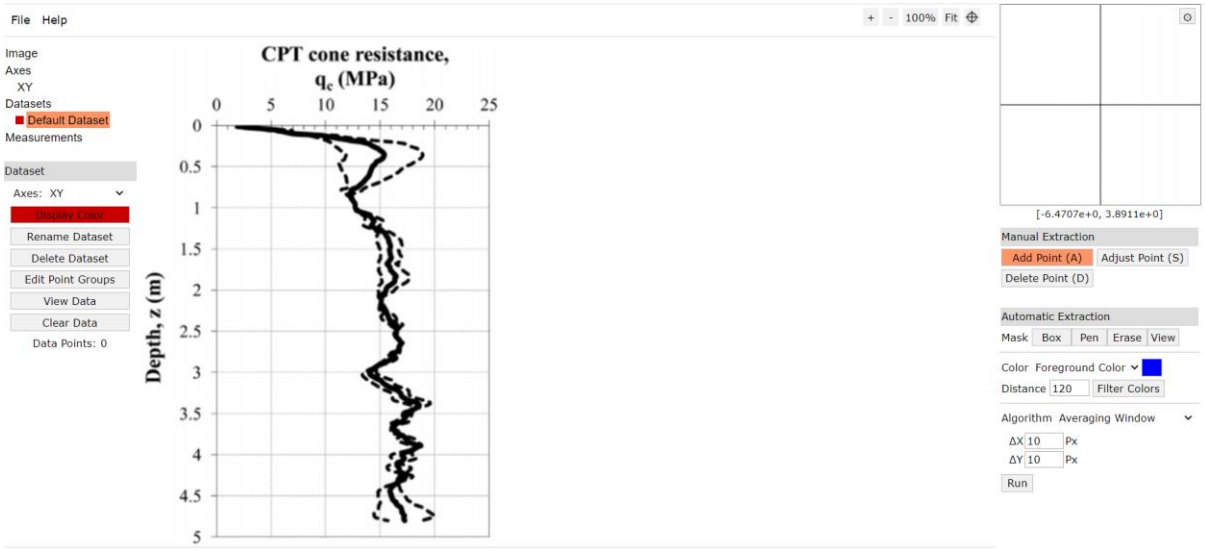

Figure 19: WebPlotDigitizer interface

It should be noted that this process involves some loss of data. Nevertheless, the resulting data are considered to sufficiently approximate the original curves. Figure 20 shows a typical example of a data trace collected using this method. This is a field test performed by Xue, et al. (2016) at the site of Blessington, Ireland. Both the *CPT* profile from the test site and the measured load-displacement response were presented in the paper. Following the proposed method in this study, the *CPT* profile and the load-displacement have been approximated as the red dots in the figure. it should be noted that for the pile loading test, the original test curve is approximated as a monotonic one instead of the original curve which resulted from static loading, in order to best compare it to results from simulated monotonic *PLT*'s

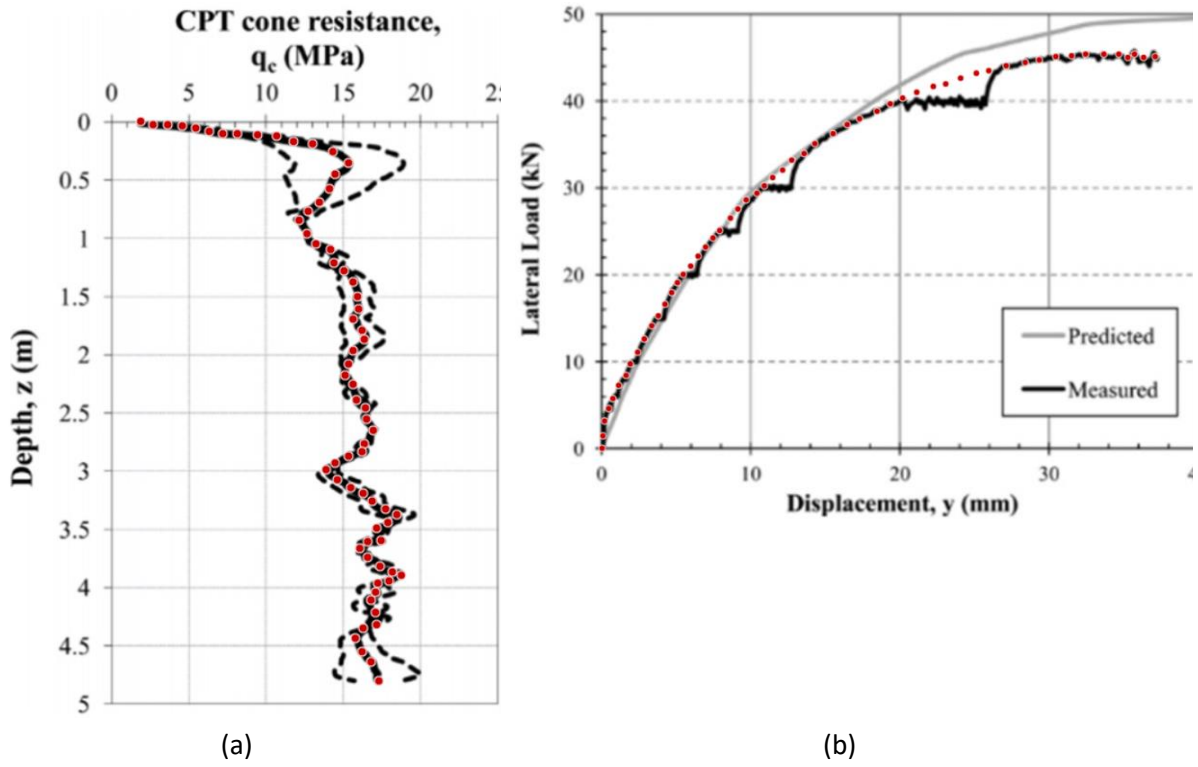

Figure 20: Typical example of CPT- (a) and H-y (b) data traces collected using WebPlotDigitizer from (Xue, et al., 2016)

Database characteristics

There are a number of ways to judge the representativeness of the *PLT* database with respect to the typical *OWT* monopile foundation characteristics. A table with relevant information for every individual test is provided in Appendix B, in this section the main takeaways are discussed. The first things to consider are the dimensions- and aspect ratios of the piles from the tests. According to Kirkwood (2016) the diameters of monopiles that are installed offshore in Europe usually exceed 6m and their aspect ratios are typically lower than 8. Furthermore, current trends indicate that even larger diameters and smaller aspect ratios will become commonplace, with foundations of D = 10m and L/D = 3 being under consideration.

Figure 21 and Figure 22 respectively show a scatter plot of the absolute pile dimensions and a distribution of the aspect ratio for the *PLT*'s in the database. It is clear that the diameters of the test piles are significantly- to much smaller than those of typical monopiles used on offshore wind farms, with the majority being under 1m. This is to be expected for field tests since full scale test setups are usually prohibitively expensive, though the prototype dimensions of the lab tests are also still on the small side. However, when looking at the arguably more important aspect ratio the database seems much more representative of offshore monopile foundations that are being built in Europe. The vast majority of piles fall in the range of $L/D < 8$. Consequently (depending on the test soil conditions), most of the piles likely behave rigidly as opposed to flexibly. This means that the composition of the dataset is different from those the methods of Novello (1999) and Dyson and Randolph (2001) were derived from, possibly leading to a poor performance of these methods.

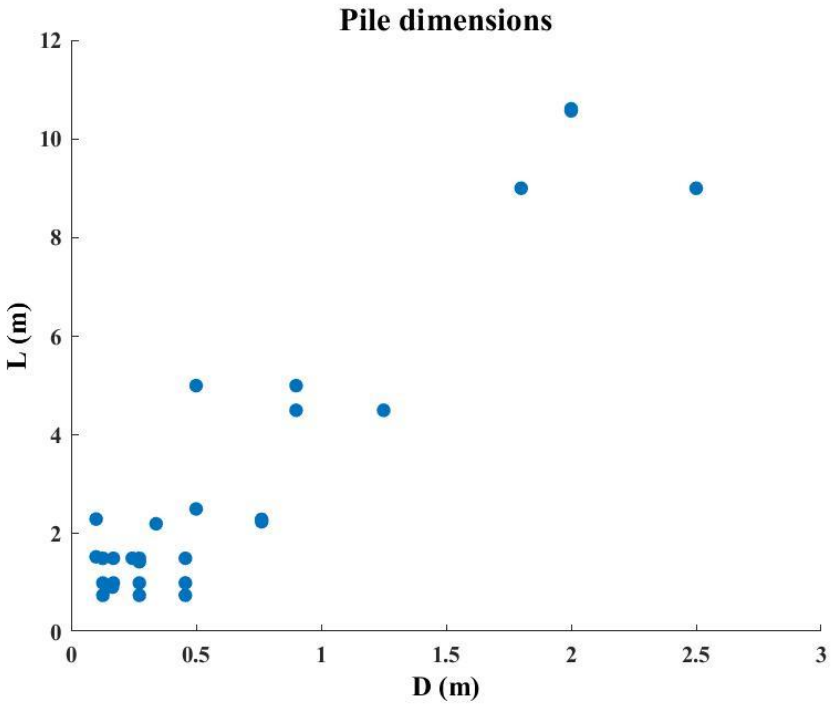

Figure 21: Database composition with regard to pile dimensions

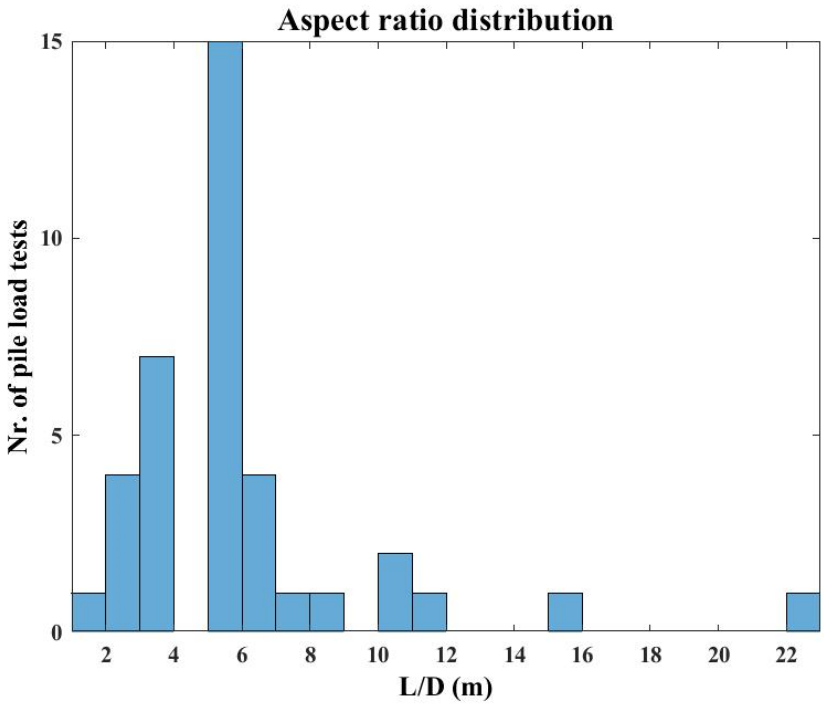

Figure 22: Database composition with regard to aspect ratio

An additional relevant characteristic of a *PLT* is the range of displacement that is applied to the pile. As stated in Section 1.2.1, according to Byrne et al. (2015b) the capacity of a monopile is usually defined by either a groundline displacement (y_0) of *D*/10 or a ground rotation (θ) of 2°. If we consider a rigidly rotating pile that is assumed to have its centre of rotation at a typical depth of 0.75*L* (Wang, et al., 2022), the following equations apply:

$$\tan \theta_{failure} = \frac{y_{0failure}}{0.75L} \tag{30}$$

$$y_{0failure} = \frac{D}{10} \tag{31}$$

Substituting $y_{0\ failure}$ and considering that $\theta_{failure}$ = 2°, we get:

$$\frac{L}{D} = \frac{1}{(10 * 0.75 \tan 2)} = 3.82 \tag{32}$$

Therefore we can state that both types of failure are reached at the same groundline displacement of D/10 for *L/D* = 3.8. This means that failure is first reached through displacement if L/D > 3.8. For smaller aspect ratios failure is first reached through groundline rotation. Since (as can be seen in Figure 22) a majority of the tested piles have an aspect ratio of more than 3.8, ground displacement usually determines whether the bearing capacity is reached. Figure 23 shows the distribution of the maximum groundline displacements of the *PLT*'s in the database. The groundline displacement of 22 tests exceeds *D*/10. Considering the groundline rotation as well, only 7 *PLT*'s fail to meet either of the *ULS* criteria. Therefore it can be stated that the performance of the *CPT*-based models regarding the prediction of pile response at both small- (*SLS*) and large (*ULS*) displacements is adequately assessed.

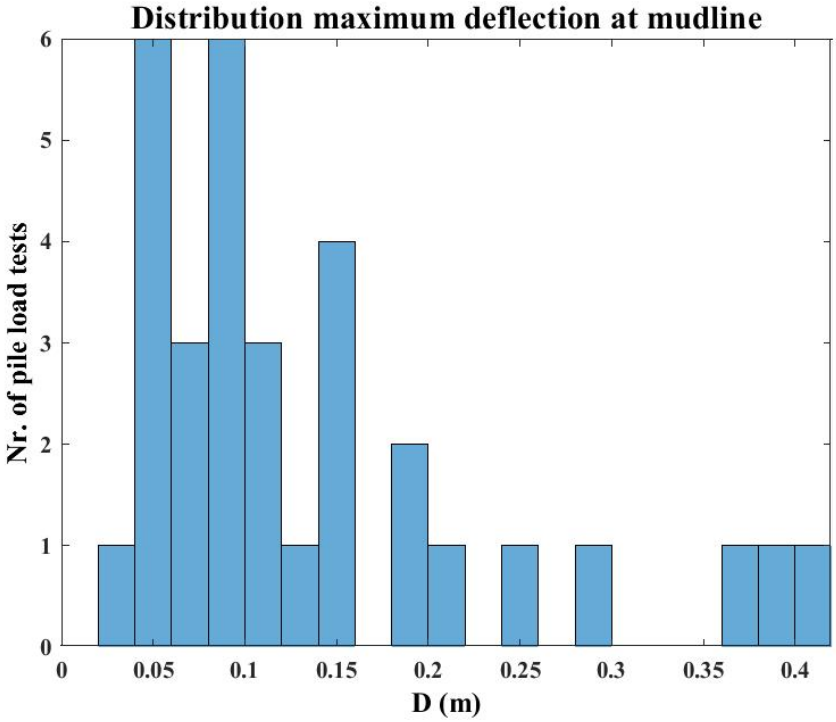

Figure 23: Database composition with regard to maximum pile displacement at the mudline

2.2 Pile-response model

In order to perform the calculations necessary to generate pile-response predictions for a given p-y method, some type om computational model is needed. In this case, a modified version of the MATLAB model that was originally built by L.J. Prendergast (2016) is used. Because it is constructed in said environment, it is possible to make adjustments as needed.

2.2.1 Model characteristics

The pile is represented in 1D as a series of 'n' beam elements. These beam elements are connected at their ends by nodes which have two possible degrees of freedom (2-DOF), namely displacement and rotation. Because the beam elements are connected at their ends, adjacent elements share a node and have the same amount of displacement and rotation at this point, as can be seen in Figure 24 .

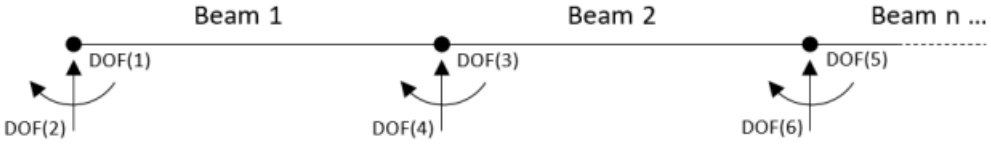

Figure 24: Series of beam elements with shared nodes and two degrees of freedom per node

The displacement of the pile is calculated in accordance with Hooke's law:

$$[Y] = \frac{[F]}{[K]}$$

where the force vector [F] and the stiffness matrix [K] are used to produce vector [Y], which contains the displacement- and angle of rotation of each beam node. The stiffness matrix consists of both a beam stiffness matrix and a spring stiffness matrix. The beam stiffness matrix is determined according to Euler-Benouilli beam theory. A local (single beam element) stiffness matrix is shown in Figure 25.

$$\begin{pmatrix} \frac{12EI}{L^3} & \frac{6EI}{L^2} & -\frac{12EI}{L^3} & \frac{6EI}{L^2} \\ \frac{6EI}{L^2} & \frac{4EI}{L} & -\frac{6EI}{L^2} & \frac{2EI}{L} \\ -\frac{12EI}{L^3} & -\frac{6EI}{L^2} & \frac{12EI}{L^3} & -\frac{6EI}{L^2} \\ \frac{6EI}{L^2} & \frac{2EI}{L} & -\frac{6EI}{L^2} & \frac{4EI}{L} \end{pmatrix} \begin{pmatrix} x_1 \\ \theta_1 \\ x_2 \\ \theta_2 \end{pmatrix}$$

DOF number: 1, 2, 3, 4

Figure 25: Euler-Bernouilli local beam stiffness matrix

The soil strength is represented by translational springs that are attached to the beam nodes, which are deformed in the lateral direction. They add an additional stiffness Ks to the displacement component of their corresponding nodes, which is calculated using one of the *p-y* formulations from Table 8. The resulting global stiffness matrix is shown in Figure 26.

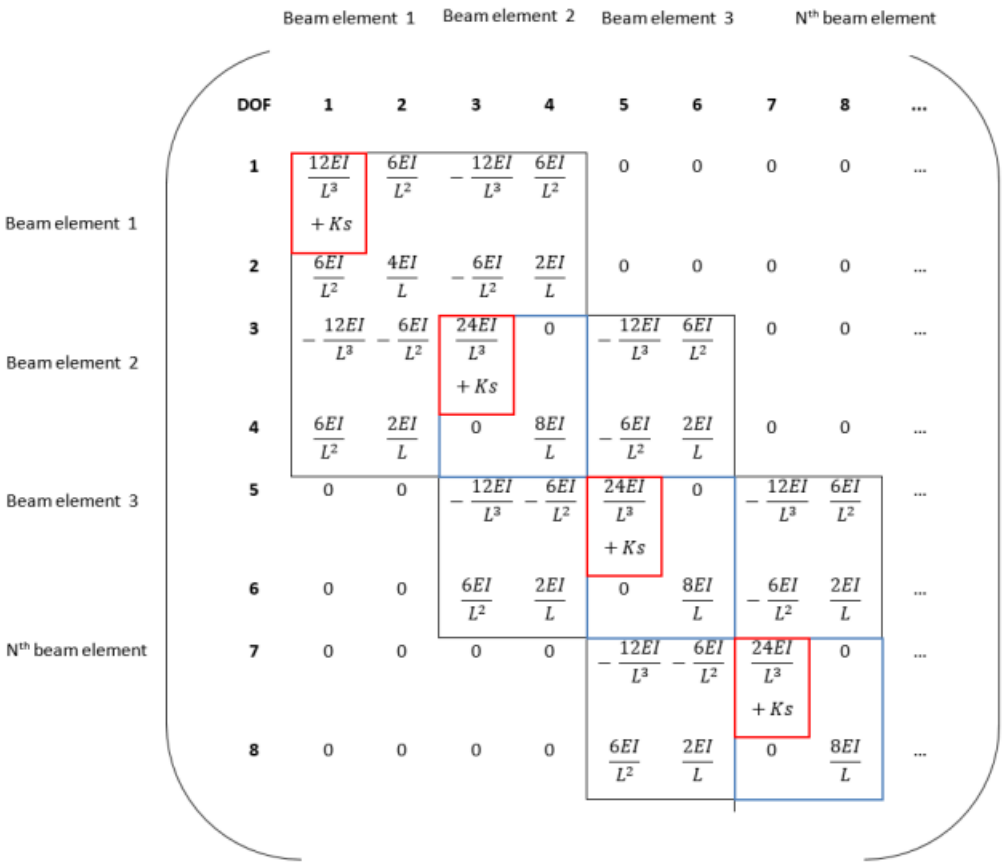

Figure 26: Global stiffness matrix, with spring stiffness at the nodes (outlined in red)

The pile load test simulations performed with this model are displacement-controlled. Thus, a maximum pile head displacement is defined, as well as displacement increment which is equal to the maximum displacement over the number of displacement steps (usually 200). For each step, the global stiffness matrix is calculated according to the above process and subsequently the forces and displacements are calculated at all the nodes. Finally the forces and displacements are taken at the mudline for all the steps to generate the predicted *H-y* response.

2.2.2 Model validation

As mentioned before, a previously constructed 1D *FE* pile-response model in MATLAB was used to run *PLT* simulations and generate load-predictions based on the *CPT*-based *p-y* methods. In order to test the validity of the in-house MATLAB beam-spring model, its load-response predictions for a typical *PLT* case are compared to those generated from a third party software. This "*LAP*" (Lateral Analysis of Piles) is a web-based application for *FE* calculations on the behaviour of vertical piles subjected to lateral loads. It was developed by J. P. Doherty (2020) at the University of Western Australia and is freely available for academic use.

The validation case is that of *PLT* number 10 from Murphy, et al. (2016), with a pile of 1.5m embedded length and a diameter of 0.245m placed in a homogeneous sand layer that is loaded at an eccentricity of 0.4m. The groundwater table is located far below the pile tip (-13m) and therefore the soil is assumed to be dry. A schematic view of the testing conditions together with a CPT profile from the site (Garryhesta, Ireland) can be seen in Figure 27.

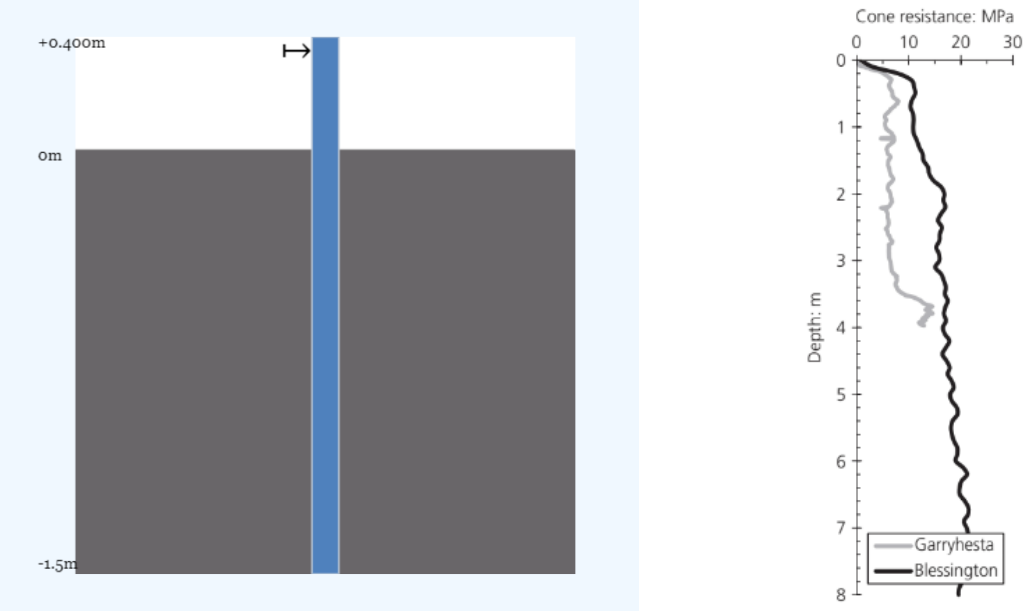

Figure 27: Schematic view of the test setup (a) and a CPT profile (b) of the validation case

In both the MATLAB beam-spring model and the LAP model, the soil is represented by springs according to the Winkler-spring method and the definition of the springs is taken from Suryasentana & Lehane (2014), as detailed previously in Section 1.2.4 The springs were defined using the measured *CPT* data from Murphy et al. (2016) Consequently, beam-spring simulations were performed using both the in-house MATLAB programme and the LAP to load the pile to a maximum displacement of 0.2*D* at the loading point. The computed load-deflection results from two programmes are presented in Figure 28. As shown in the figure, the computed load-deflection curves are close to each other with a maximum difference of around 4%. Additionally, Figure 29 and Figure 30 show that although the two bending moment profiles differ somewhat, the predicted deflection profiles are nearly identical. It can be concluded that the in-house MATLAB model can be deemed sufficiently reliable for the execution of the required *PLT* simulations.

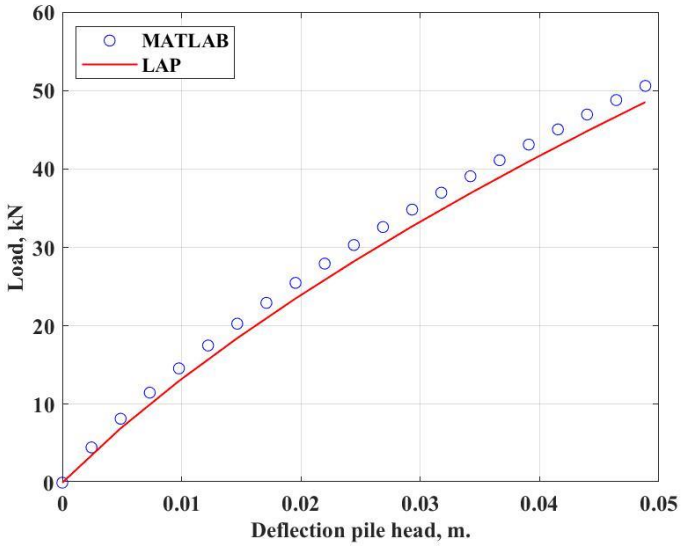

Figure 28: Comparison of load-deflection results from simulations in both the MATLAB- and LAP models

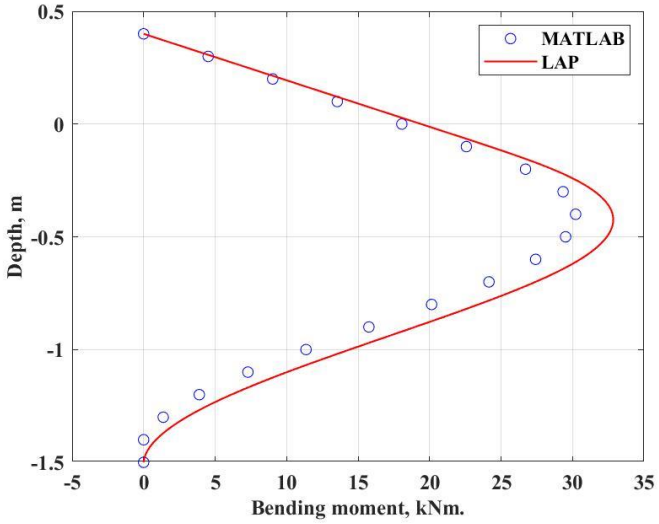

Figure 29: Comparison of bending moment profiles from simulations in both the MATLAB- and LAP models

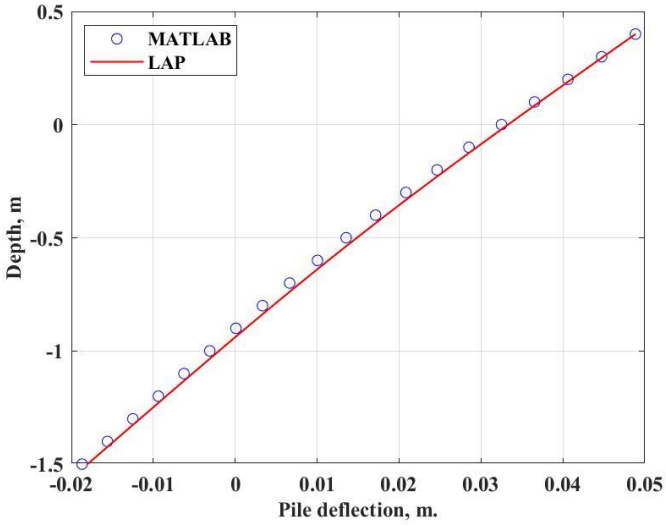

Figure 30: Comparison of deflection profiles from simulations in both the MATLAB- and LAP models

2.3 Results

2.3.1 Typical load-deflection results

The predictions of the various *CPT*-based *p-y* models can be assessed in quantitative ways (as is done in Sections 2.3.2 and 2.3.3). However several conclusions can also be drawn on a qualitative basis when looking at some typical load-deflection results. For instance, there is a clear difference in the change in stiffness of the pile response with increasing displacement between the power-law based *p-y* methods from Novello (1999), Dyson & Randolph (2001) and Li, et al. (2014) on the one hand and the methods from Suryasentana & Lehane (2014;2016) on the other. Figure 31 shows a typical pile load test result, where the power-law based methods predict a marginally stiffer response at small displacements and a less stiff response at larger displacements. The results for all 39 *PLT*'s in the database can be viewed in Appendix A and the test specifications can be found in Appendix B.

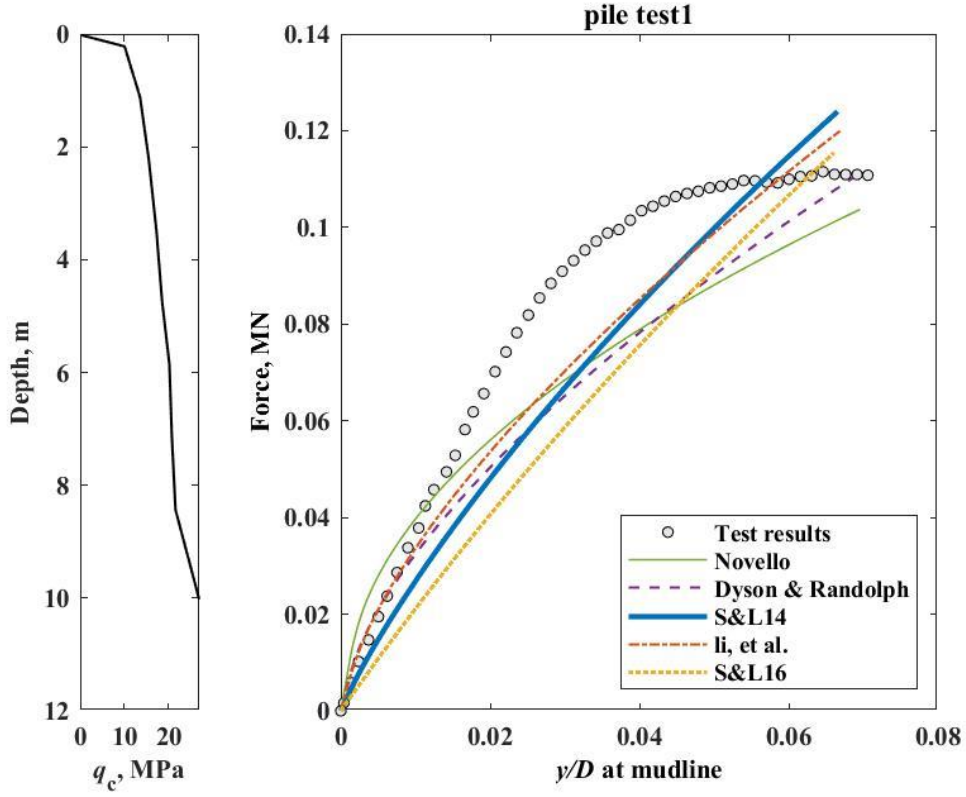

Figure 31: Typical PLT result, measurement data from Doherty, et al. (2012)

Furthermore, in the simulations of most *PLT*'s, the *CPT*-based *p-y* methods all exhibit a similar shortcoming in the prediction of the pile behaviour. As can be seen in Figure 32 and Figure 33, in all cases the measured *H-y* curve from the pile test shows a non-linear transition from an initial stiff response at small displacements to a less stiff response at large displacement. This can likely be attributed to the degradation of soil stiffness with strain until the shear strength is reached, as the shear strain of the soil around the pile increases with the pile displacement. However, it is clear in all the cases that the studied *CPT*-based *p-y* methods can only predict a gradual decrease in stiffness, without a clear transition to the ultimate state. For the models by Novello (1999), Dyson & Randolph (2001) and Li, et al. (2014) this can be expected, since they use a power function to define the p-y curves, whose soil resistance will always increase with displacement and will never reach an ultimate value. However, this also occurs for the models from Suryasentana & Lehane (2014;2016) which do have an explicitly defined ultimate soil resistance. This suggests that none of the methods can adequately capture the whole range of non-linear response of laterally loaded piles, from small to large deflections.

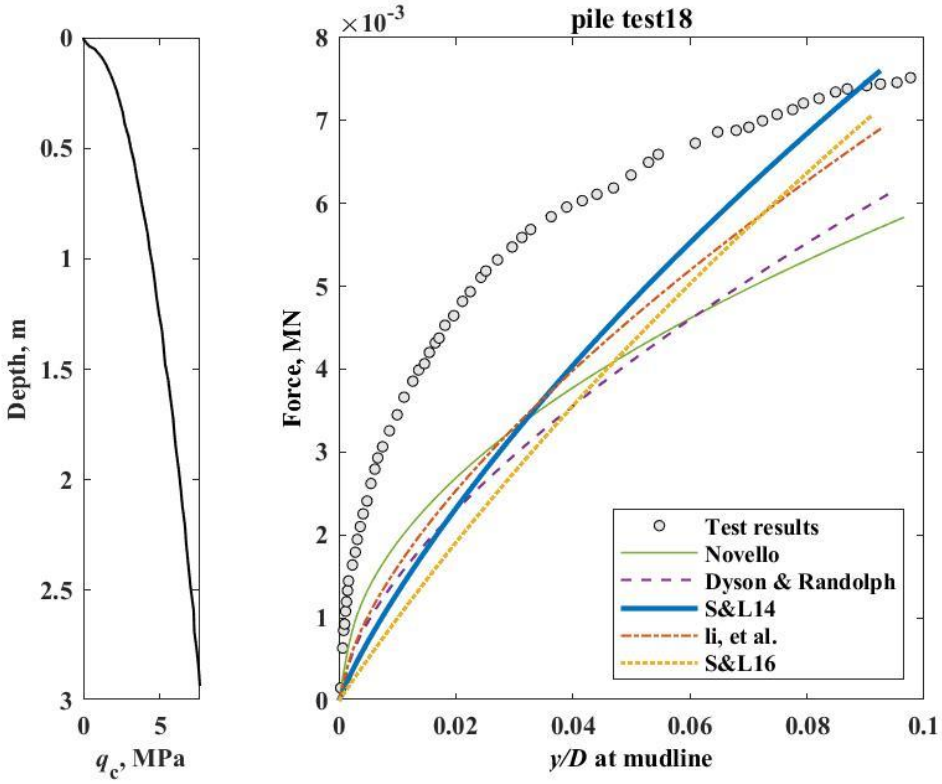

Figure 32: Typical PLT result, measurement data from Wang, et al. (2020)

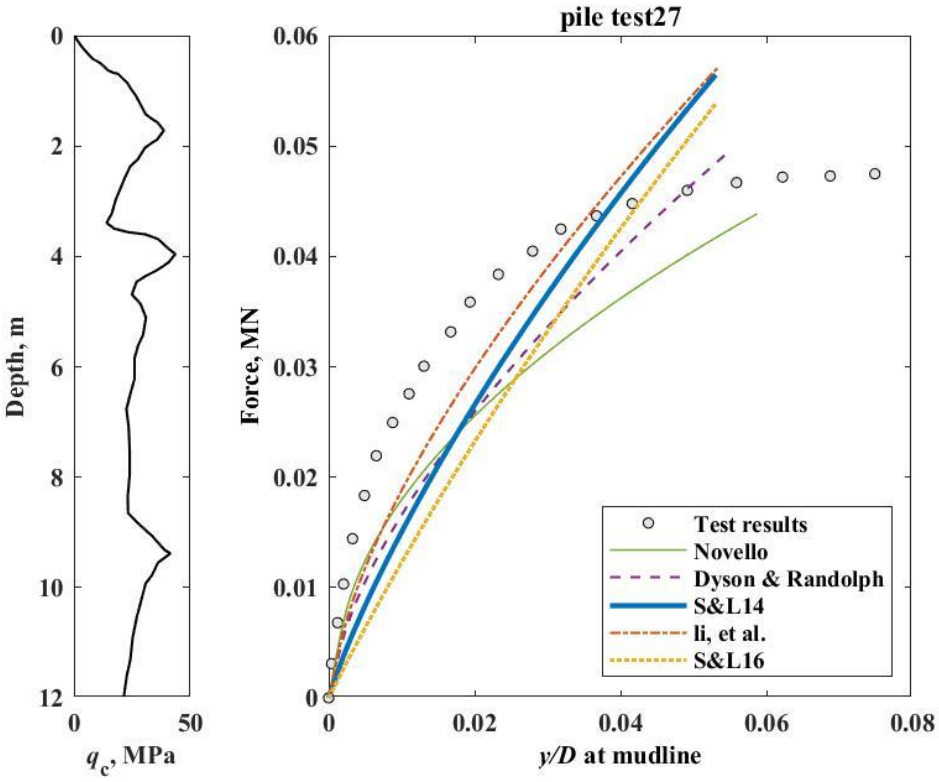

Figure 33: Typical PLT result, measurement data from McAdam, et al. (2019)

2.3.2 Method accuracy

In order to make quantitative comparisons between the performance of the various *p-y* methods, an 'accuracy metric' η is used. It was originally conceived by Burd, et al. (2019) to assess the accuracy of the predictions of the PISA model. This metric is defined according to Equation 33 and its meaning is further illustrated in Figure 34 (note that the curves for the '3D- and 1D *FE* model' in this case correspond to the measured- and predicted *H-y* curves).

$$\eta = \frac{(A_{ref} - A_{diff})}{A_{ref}} = \frac{(\int H_{measured} - \int \left| H_{predicted} - H_{measured} \right|)}{\int H_{measured}} \tag{33}$$

Metric η quantifies the fit of the predicted load-displacement curve to the measured curve over a given range of displacement for a given pile load test.

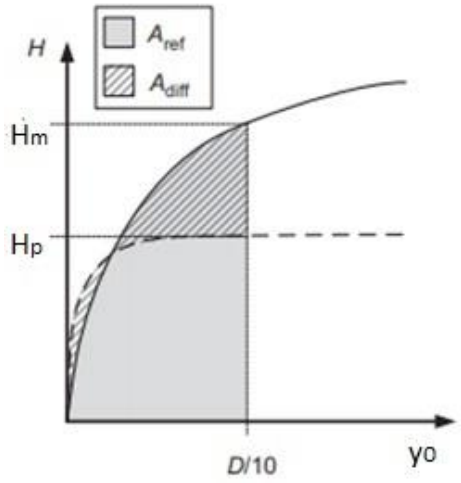

Figure 34: Illustration of the definition of the accuracy metric after Burd, et al. (2019)

In order to compare the accuracy of the different *p-y* methods for both the initial- and the ultimate response, η is evaluated at $0 < y < 0.025D$ and $y > 0.025D$ respectively.

Accuracy by method

From each of the 38 *PLT*'s, a value for η is obtained for the initial- and ultimate response for each *CPT*-based *p-y* method. The accuracy metric values of all the individual pile load tests for both the initial- and ultimate response can be found in Appendix C. In order to represent the variation in accuracy between tests, a histogram with the distribution of η over the 38 *PLT*'s is plotted for each case. Figure 35a through -j shows these distributions. The accuracy metric values of all the individual pile load tests for both the initial- and ultimate response can be found in Appendix C. Since η cannot (by definition) exceed 1, the distribution of a set of highly accurate predictions is expected to have a peak frequency at η just under 1, with a rapidly decreasing tail towards the smaller values of η. However, this is only partly the case since both for the initial- and the ultimate response the methods frequently produce predictions with an accuracy of 0.8 or lower. In most cases, η ranges between 1 and 0, meaning that the predicted load deviates from the measurements up to 100% of the measured load. In fact, for the initial responses predicted by the model from Novello (1999) and the ultimate responses predicted by

Suryasentana & Lehane (2014;2016), several *PLT* predictions have negative values of η, indicating a very significant overestimation of the pile head load.

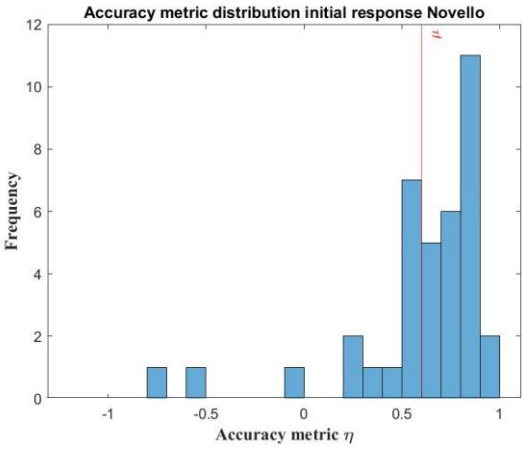

(a)

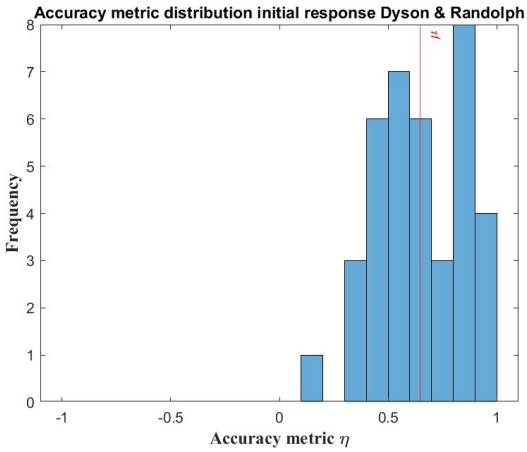

(b)

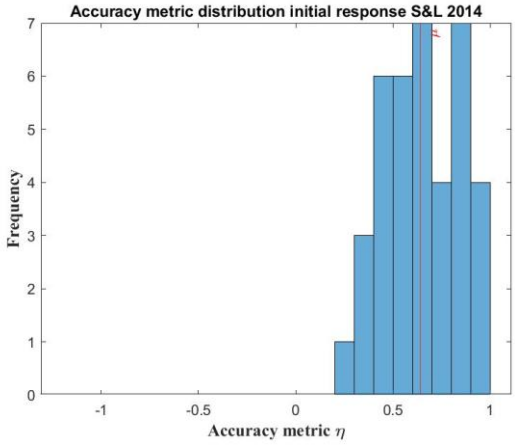

(c)

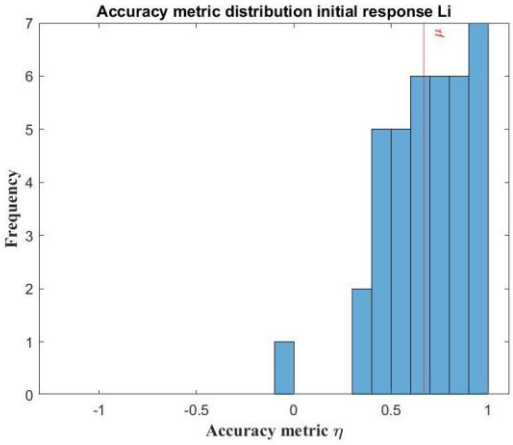

(d)

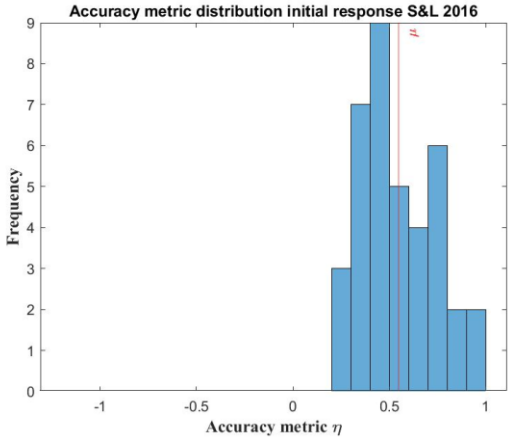

(e)

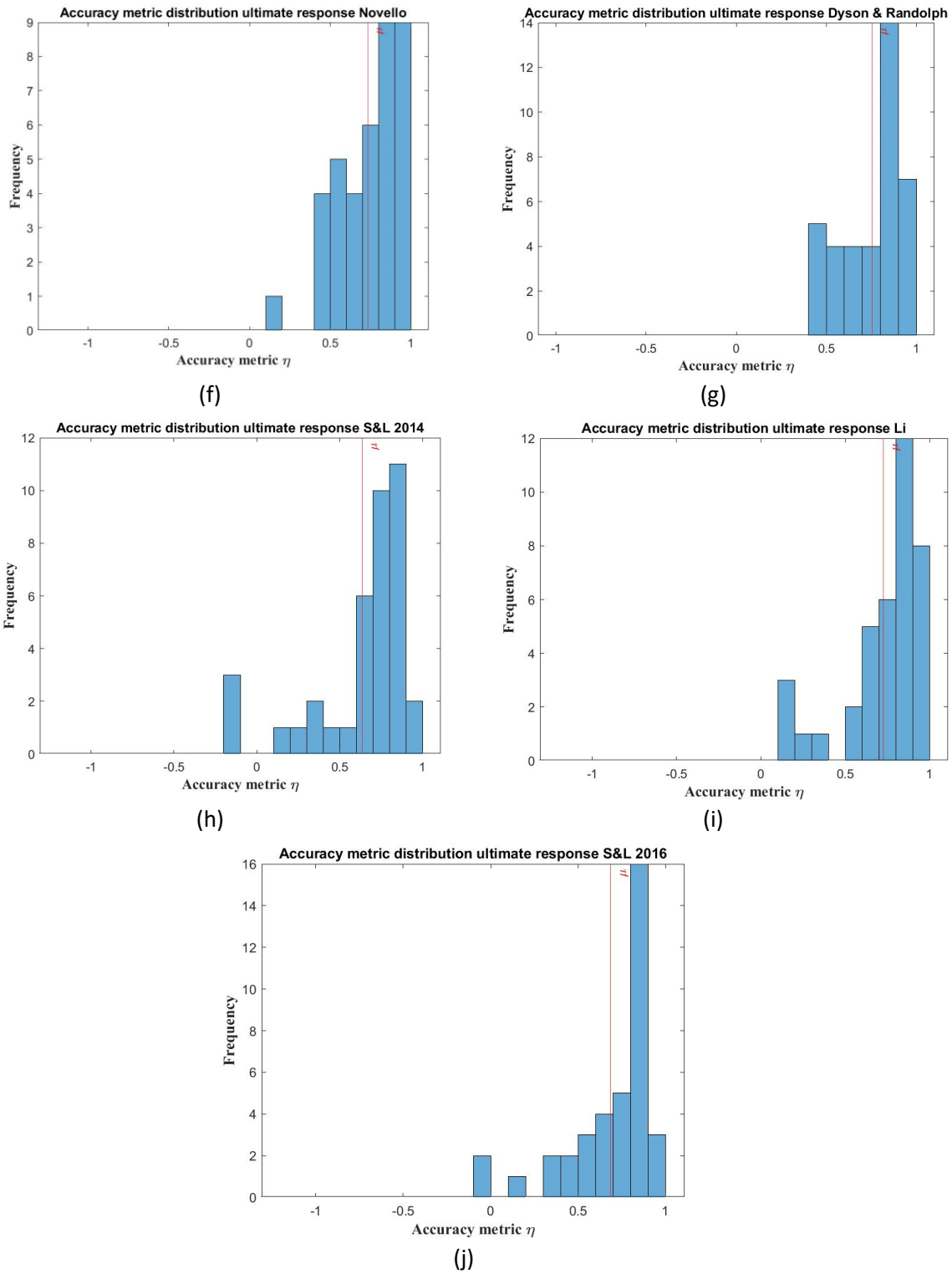

Figure 35: Distribution of the accuracy scores of p-y methodl predictions per PLT for the initial- and ultimate response respectively

The aforementioned trend of large tails with strongly inaccurate predictions holds true for all methods. As Table 11 shows, the predictions generated with the methods from Dyson & Randolph (2001) and Li, et al. (2014) are on average overall the most accurate, with the former having the highest mean η values for the ultimate response and the latter having the highest accuracy up to a groundline displacement up to 0.025D. Another trend is that for all methods except that from

Suryasentana & Lehane (2014), the ultimate response is predicted more accurately on average than the initial one.

Table 11: mean values per CPT-based p-y method for the initial- and ultimate response

CPT-based *p-y* methods	$\eta_{initial}$	$\eta_{ultimate}$
Novello	0.600	0.733
Dyson & Randolph	0.648	0.755
Suryasentana & Lehane 2014	0.640	0.636
Li et al.	0.671	0.726
Suryasentana & Lehane 2016	0.549	0.686

Correlations accuracy with pile characteristics

Additional to the overall accuracy of the methods predictions, the correlation between accuracy and the most important pile characteristics is assessed. The chosen characteristics are the pile aspect ratio (*L/D*) and the rigidity of the pile behaviour. These two characteristics are chosen because (as mentioned in Section 1.2.4) the empirical datasets that the methods from Novello (1999), Dyson & Randolph (2001) and were derived from mostly contain tests on long- and flexible piles. This is in contrast to the methods developed by Suryasentana & Lehane (2014;2016), which were derived from a set of numerical simulations with a broader range of rigid- to flexible- and short- to long piles.

To characterize the rigidity of the pile, the dimensionless criterion put forth by Poulos & Hull (1989) is adopted:

$$Rigidity = \frac{E_p I}{(L^4 E_s)} \tag{34}$$

Where E_p is the Young's modulus of the pile, *I* is the section moment of inertia of the pile, *L* is the pile's embedded length and E_s is the soil Young's modulus. Therefore, it is clear that the longer the pile, the smaller the section bending stiffness (i.e. *EI*) of the pile and the smaller the soil stiffness, the more flexible the overall behaviour of the pile is. However, it should be noted that this definition relies upon the elastic modulus of the soil E_s, which is not known for the relevant *PLT*'s. Previous work such as that from Robertson (2009) has shown that the elastic modulus is strongly correlated to the cone resistance in drained soils. Therefore the cone resistance at the depth of the pile tip is taken as a proxy for the soil stiffness. This means that the resulting values of the rigidity criterion cannot be used to categorize the piles as behaving either rigidly or flexibly according to the ranges specified in Poulos and Hull (1989). Nevertheless, they can be used in their own right as a relative indication of rigidity, which can in turn be correlated with the accuracy of the method predictions.

Looking at the correlation between the accuracy of the method predictions and the aspect ratios of the piles for the initial response, there does not seem to be a strong relationship. Figure 36 and Figure 37 show scatter plots of the aspect ratio with the prediction accuracy for Dyson & Randolph (2001) and Suryasentana & Lehane (2016) with a linear trend. They respectively respectively show a low positive correlation (meaning that the accuracy increases with increasing pile length) and no correlation, which is similar to the other *CPT*-based *p-y* methods (a complete list of plots for all methods can be found in Appendix D).

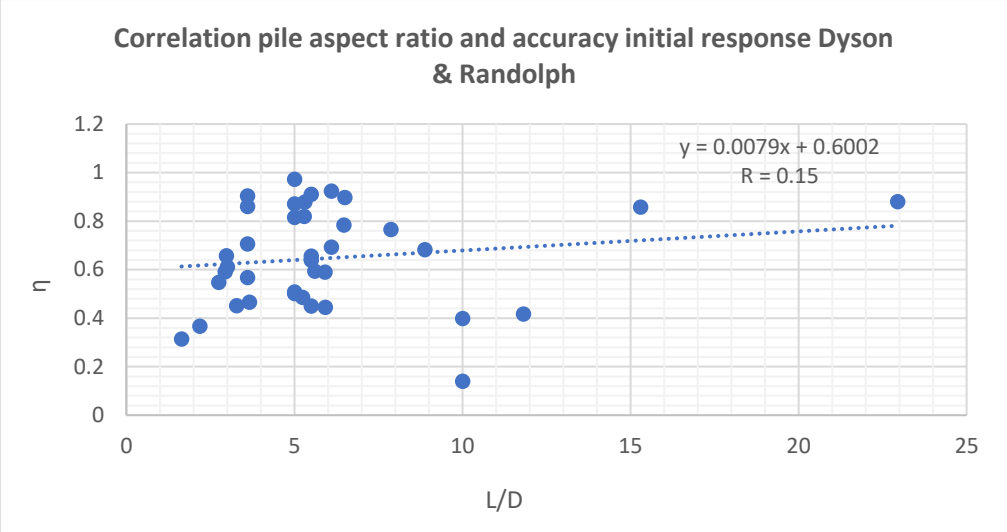

Figure 36: Scatter plot showing the correlation between pile aspect ratios and H-y prediction accuracy for Dyson & Randolph (2001) for the initial response

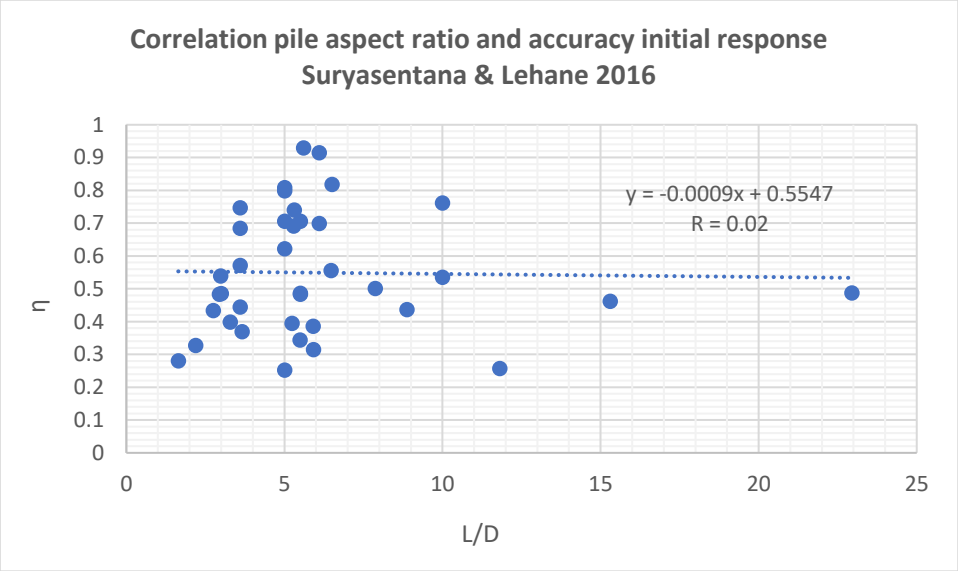

Figure 37: Scatter plot showing the correlation between pile aspect ratios and H-y prediction accuracy for Suryasentana & Lehane (2016) for the initial response

The picture is somewhat different for the ultimate response. Figure 38 and Figure 39 show the scatter plots for the predictions from Novello (1999) and Suryasentana & Lehane (2014) respectively. The first contains a weak negative trend, the second shows a moderate negative correlation (meaning decreasing accuracy with increasing pile length). The remaining models match this trend with weak to moderate negative correlations.

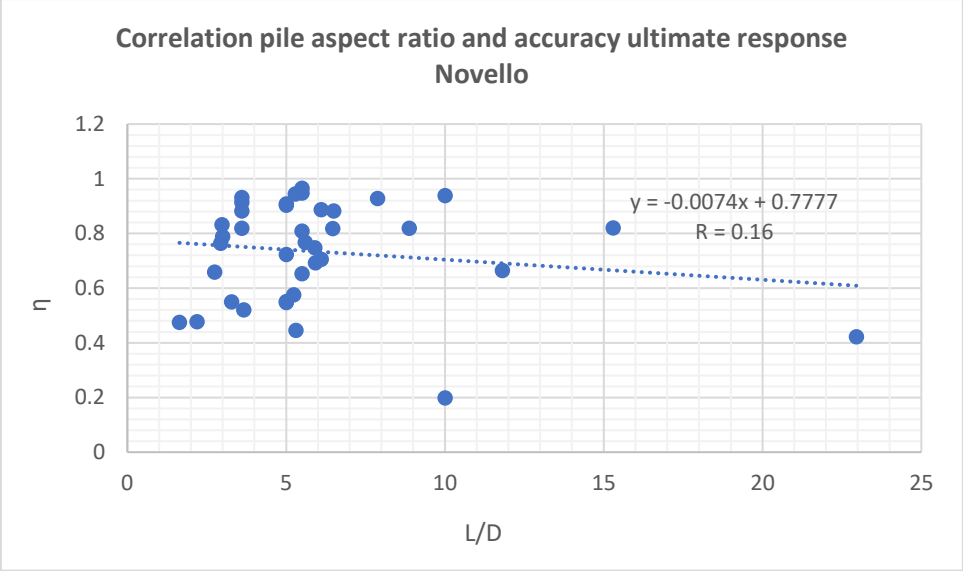

Figure 38: Scatter plot showing the correlation between pile aspect ratios and H-y prediction accuracy for Novello (1999) for the ultimate response

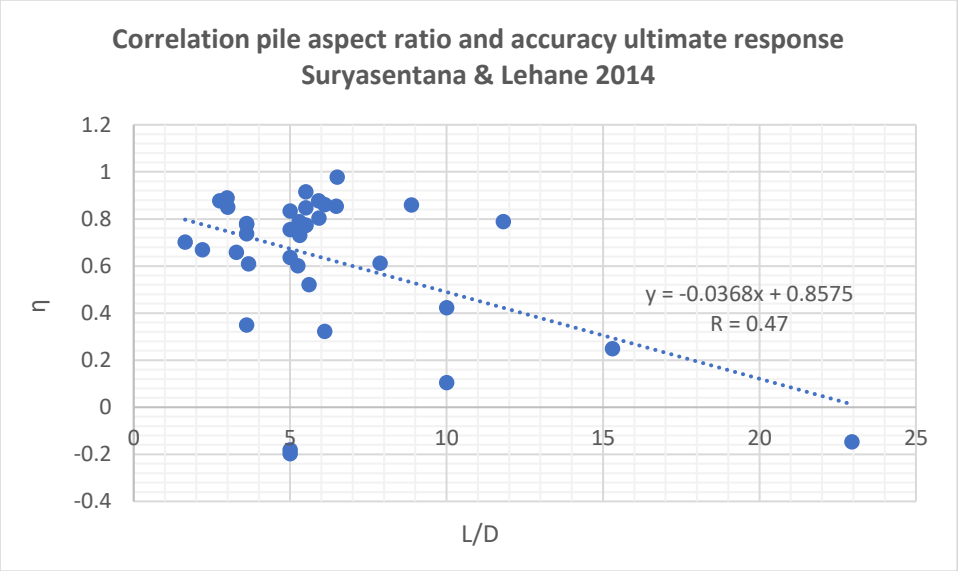

Figure 39: Scatter plot showing the correlation between pile aspect ratios and H-y prediction accuracy for Suryasentana & Lehane (2014) for the ultimate response

The strongest trend can be observed for the relationship between the rigidity of the pile behaviour and the prediction accuracy for the initial response. With the exception of Novello (2001), all methods show a moderately strong negative correlation (meaning decreasing accuracy with increasing rigidity), and none except Novello (1999) have many outlier accuracy values. This is illustrated in Figure 40 and Figure 41 (note the log scale on the rigidity-axis).

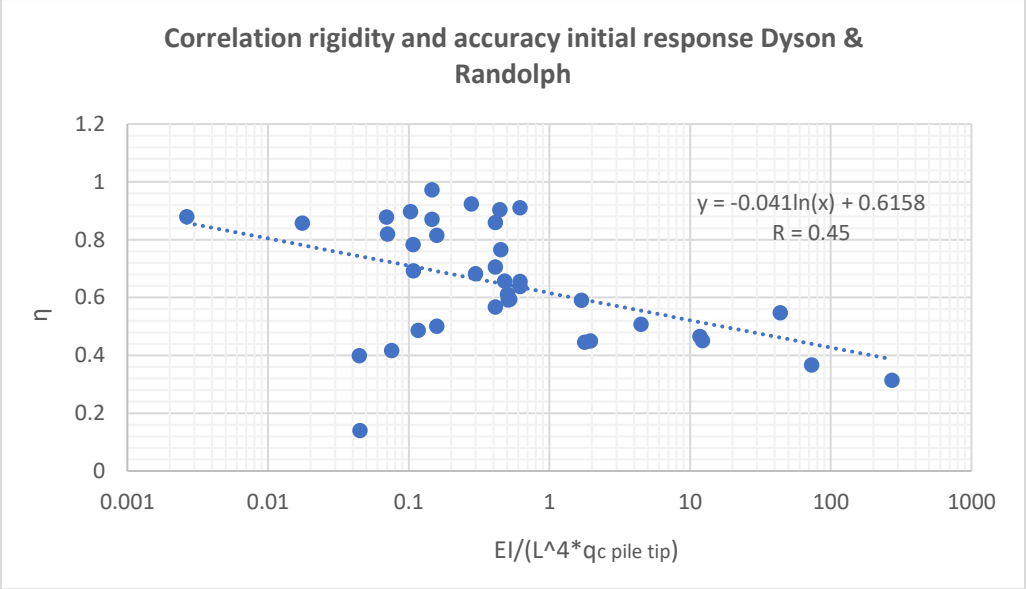

Figure 40: Scatter plot showing the correlation between pile behaviour rigidity and H-y prediction accuracy for Dyson & Randolph (2001) for the initial response

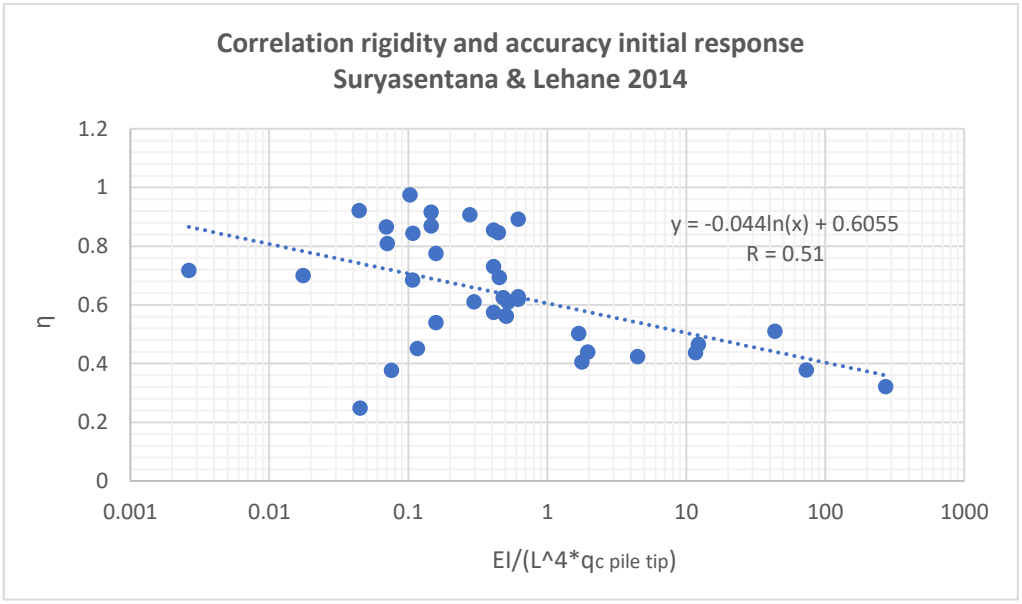

Figure 41: Scatter plot showing the correlation between pile behaviour rigidity and H-y prediction accuracy for Suryasentana & Lehane (2014) for the initial response

Looking at the ultimate response, the trend in the relationship between the accuracy and the rigidity of the pile behaviour is less strong for most methods. This is shown in Figure 42 and Figure 43. A difference with the initial response is that the trend changes to a positive correlation for Suryasentana & Lehane (2014), Li, et al. (2014) and Suryasentana & Lehane (2016), (meaning increasing accuracy with increasing pile behaviour rigidity).

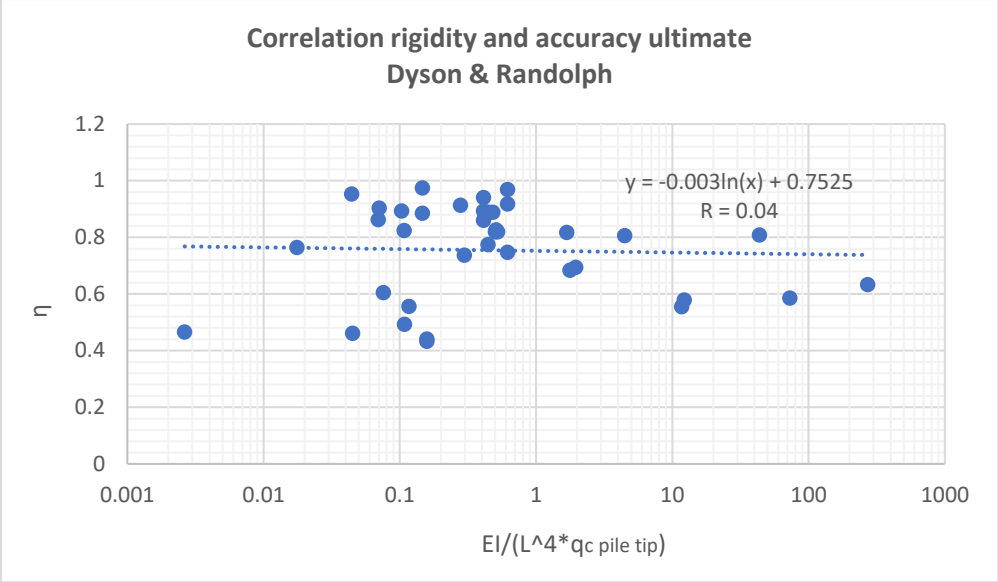

Figure 42: Scatter plot showing the correlation between pile behaviour rigidity and H-y prediction accuracy for Dyson & Randolph (2001) for the ultimate response

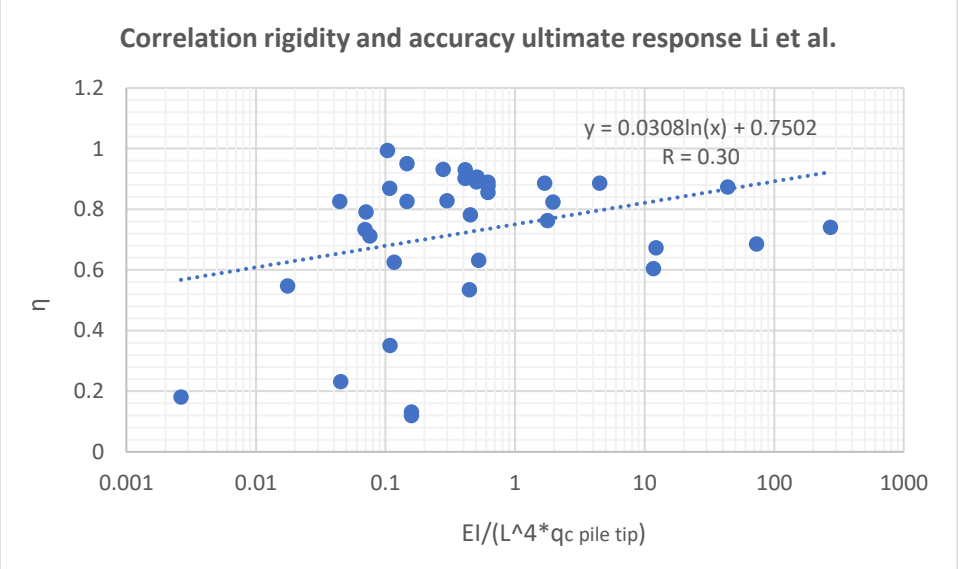

Figure 43: Scatter plot showing the correlation between pile behaviour rigidity and H-y prediction accuracy for Li, et al. (2014) for the ultimate response

Taking all the aforementioned into consideration, a few general observations can be made. Table 12 shows an overview of all the calculated correlation coefficients (*R*) for correlations with the accuracy metric *η*. Perhaps with the exception of the correlation between the pile behaviour rigidity and prediction accuracy at larger displacements, no real relationships seem to exist for Novello (1999). However, for the other methods the relationship between rigidity and accuracy for the initial response seems convincing. Though the correlations for the initial response with the aspect ratio are less strong, it does seem that at small displacements all methods except Novello perform better for relatively long and flexible piles. Although the trends are less strong, the opposite looks to be the case for the

ultimate response. Here mainly Suryasentana & Lehane (2014) and Li, et al. (2014) show better performance for relatively short and rigid piles.

Table 12: Overview all correlations per CPT-based p-y method

	Aspect ratio ($\frac{L}{D}$)				**Rigidity ($\frac{EI}{(L^4E_s)}$)**			
	Initial		**Ultimate**		**Initial**		**Ultimate**	
	R	**+ or -**	**R**	**+ or -**	**R**	**+ or -**	**R**	**+ or -**
Novello	0.07	-	0.16	-	0.02	-	0.16	-
D&R	0.15	+	0.24	-	0.45	-	0.04	-
S&L 2014	0.10	+	0.47	-	0.51	-	0.40	+
Li et al.	0.15	+	0.41	-	0.37	-	0.30	+
S&L 2016	0.02	-	0.32	-	0.47	-	0.23	+

2.3.3 Method bias

In order to show whether a method tends to over- or underpredict developed loads at a given displacement, a 'ratio metric' ρ is employed. This metric is defined according to Equation 35.

$$\rho = \frac{H_{predicted}}{H_{measured}} \tag{35}$$

For $\rho < 1$ the predicted loads are smaller than the measured loads at the given displacement. Therefore, the soil strength is underestimated and the method is conservative. For $\rho > 1$, the soil strength is overestimated and the method is unconservative. Similarly to the prediction accuracy, the bias is evaluated at two points of normalized displacement to compare the initial- and the ultimate response. These chosen points are y = *D*/100 and y = *D*/10 respectively.

Bias by method

In order to show the trends in the biases of the method predictions, lognormal distributions are generated of the calculated ρ values from all 38 *PLT*'s in the database for the five methods. An example of such a distribution and the underlying histogram can be seen in Figure 44. The distributions for all the cases can be found in Appendix D.

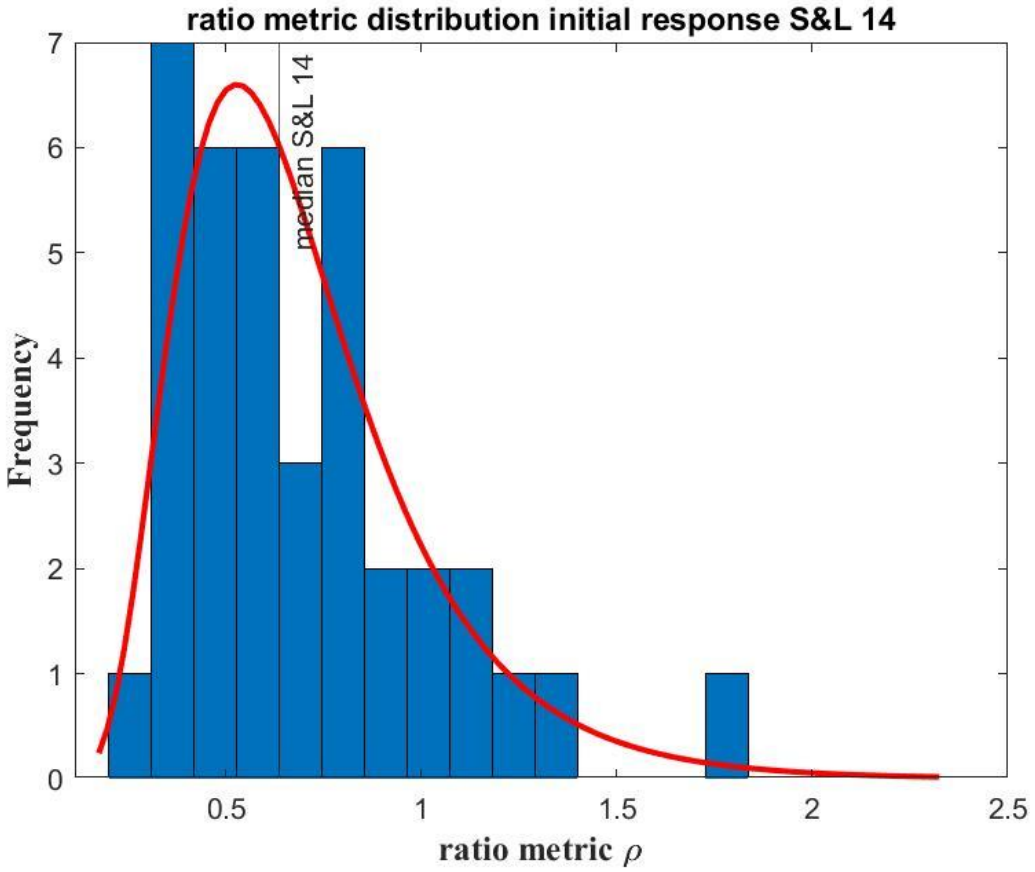

Figure 44: Histogram and fitted distribution ratio metric values for the initial response predicted by Suryasentana & Lehane (2014)

Subsequently, lognormal probability density functions are fitted to these distributions in order to compare the methods with minimal clutter. The ratio metric values of all the individual pile load tests for both the initial- and ultimate response can be found in Appendix C.

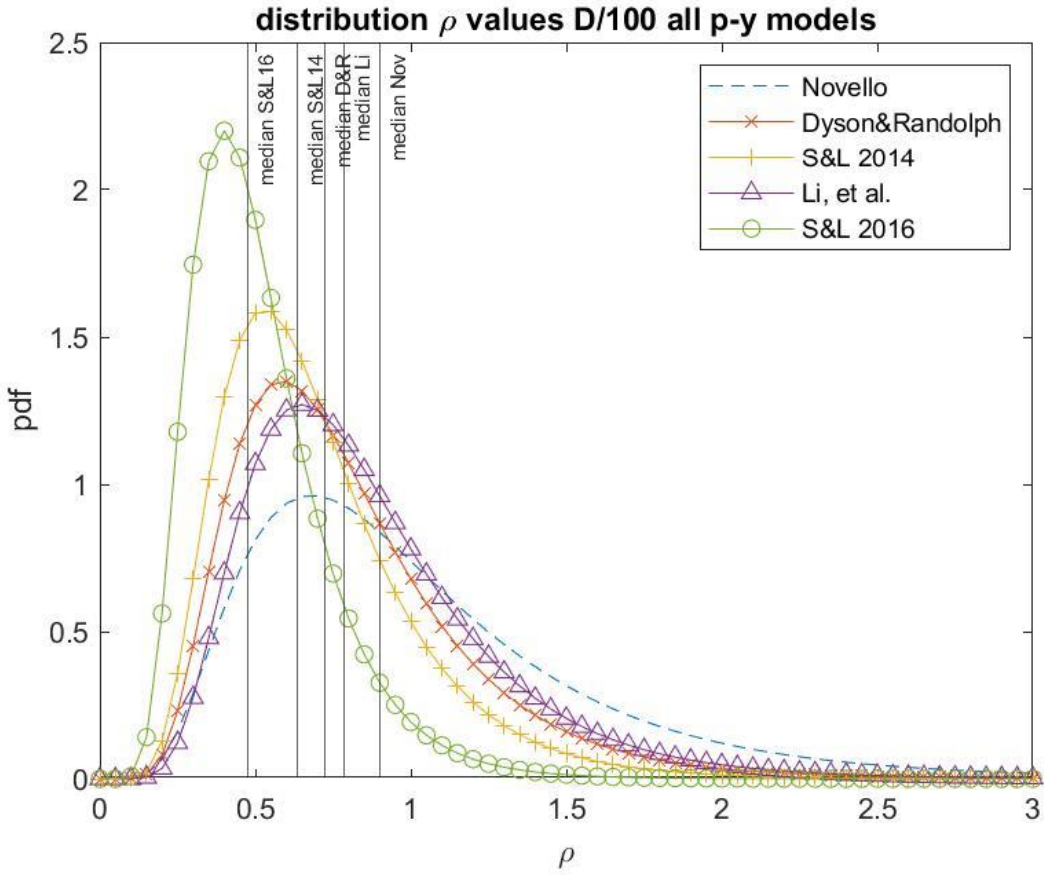

Figure 45: Probability density functions of rho values per CPT-based p-y method at a displacement of D/100

Figure 45 shows the probability density functions of ρ for the five methods at a small normalized displacement of $D/100$. In this case, all methods show mostly conservative predictions, with the median prediction resulting from the method of Suryasentana & Lehane (2016) underestimating the developed load by over 50% (median values for all methods are given in Table 13). Furthermore, the coefficients of variation (CV) range from 0.436 to 0.569, indicating a very high relative variability. This makes sense when looking at the wide spread of ρ values shown in Figure 45.

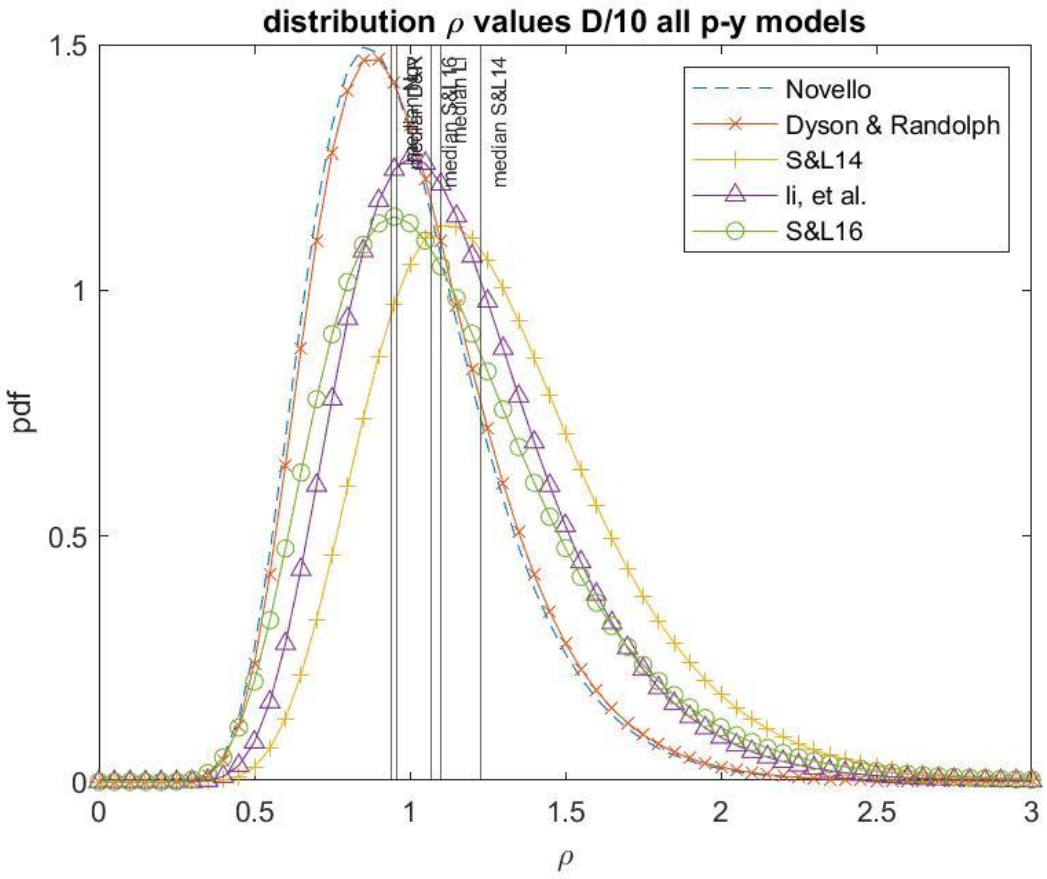

Figure 46: Probability density functions of rho values per CPT-based p-y method at a displacement of D/10

As can be seen in Figure 46, at a normalized displacement of *D*/10 the median values of *ρ* are closer to 1 compared to those for a displacement *D*/100, which points to less of a bias in the predictions. Additionally, the coefficients of variation are lower than those at *D*/100 (ranging between 0.302 and 0.307), indicating a smaller relative variability in the predictions. This all matches the results from Section 2.3.2 that show more accurate predictions at large displacements. However, all methods have median values close to- or higher than 1, indicating either a neutral or unconservative prediction bias.

Table 13: median ρ values per CPT-based p-y method for the initial- and ultimate response

CPT-based p-y method	$\text{Median}_{D/100}$	$\text{CV}_{D/100}$	$\text{Median}_{D/10}$	$\text{CV}_{D/10}$
Novello	0.901	0.569	0.942	0.302
Dyson & Randolph	0.721	0.478	0.957	0.302
Suryasentana & Lehane 2014	0.636	0.453	1.227	0.307
Li et al.	0.786	0.462	1.101	0.305
Suryasentana & Lehane 2016	0.474	0.436	1.069	0.355

2.4 Conclusions & Discussion

Looking at the overall quality and characteristics of the input data from the database an number of observations can be made. Firstly, the nature of the data collection process likely introduces some error in both the calculated *p-y* method accuracies and -biases. With the exception of the data from Wang et al. (2020) and the lab tests performed specially for this study, the source data were not available and the data were instead extracted from approximated curves. This means that the input *CPT* data for the MATLAB pile-response model and the *H-y* measurement data that the various *p-y* method predictions are compared to contain some amount of additional error compared to the source. However, the accuracy of the predictions on average is relatively low, the variation in the accuracy of the predictions is comparatively large and the dataset is decently sized with 38 *PLT*'s (which should mean that the errors cancel out on average, assuming the error introduced by the data collection process is random in nature). Therefore this error is not likely to severely impact the validity of the conclusions from this study. Secondly, as discussed in Section 2.1 the composition of the *PLT* database is reasonably representative with respect to pile dimensions, pile aspect ratios and *PLT* displacement ranges when looking at the most relevant application of the design of short- to medium length monopile foundations.

A qualitative analysis of the *H-y* curves of the individual *PLT*'s yields two insights into the tendencies of the different *CPT*-based *p-y* methods. Firstly as mentioned previously, there appears to be a difference in the change in stiffness of the pile response with increasing displacement between the power-law based *p-y* methods from Novello (1999), Dyson & Randolph (2001) and Li, et al. (2014) on the one hand and the methods from Suryasentana & Lehane (2014;2016) on the other. The power-law based methods predict a marginally stiffer response at small displacements and a less stiff response at larger displacements. Secondly, in the clear majority of cases the studied *p-y* methods only predict a gradual decrease in stiffness, without a clear transition to weak behaviour. This shows that even though the methods from Suryasentana & Lehane (2014;2016) do have an ultimate soil resistance built in, most likely none of the methods adequately capture this behaviour.

Table 14: Mean η- and median ρ values per method

CPT-based p-y method	$\eta_{initial}$	$\eta_{ultimate}$	$\rho_{D/100}$	$\rho_{D/10}$
Novello	0.600	0.733	0.901	0.942
Dyson & Randolph	0.648	0.755	0.721	0.957
Suryasentana & Lehane (2014)	0.640	0.636	0.636	1.227
Li et al.	0.671	0.726	0.786	1.101
Suryasentana & Lehane (2016)	0.549	0.686	0.474	1.069

As can be seen in Section 2.3 and summarizing Table 14, for all *p-y* method except that from Suryasentana & Lehane (2014) the ultimate response predictions are more accurate than those for the initial response. Furthermore, all methods generate predictions that are slightly- to strongly conservative for a displacement of *D*/100, whereas all methods are either neutral or unconservative for a displacement of *D*/10. The latter can perhaps be explained by the absence of an ultimate soil pressure in the methods from Novello (1999) and Li et al. (2014) and a structural overestimation of the ultimate soil pressure in the methods from Suryasentana & Lehane (2014) and Suryasentana & Lehane (2016). Generally, the *H-y* predictions show a larger average bias and a lower accuracy at small displacements. This is not ideal since behaviour at small displacements is most relevant for the compliance with failure criteria of monopile structures (Byrne et al., 2015b), although the conservative bias of the predictions at small displacements can at least be considered safe. The reason for the

comparatively low accuracy could however lie outside of shortcomings of the *p-y* methods and it could instead be due to a lack of data density in these small displacement ranges or a higher sensitivity to uncertainties in soil conditions. Something that should be noted when making these inferences is that a substantial number of pile load tests is not included in the calculations for ρ at $D/10$, because their maximum displacement at y_0 is lower than this. By contrast, all pile load tests are included in the calculations for η in both the initial- and ultimate displacement range.

Comparing the predictions from the different *p-y* methods against each other, an surprising pattern emerges. In the ultimate displacement range (>0.025D), the methods from Novello (1999) and Dyson & Randolph (2001) produce the most accurate predictions. In the initial displacement range, the method from Li, et al. (2014) performs best. It can be concluded that overall the methods from Dyson & Randolph and Li, et al. (2014) provide the best predictions. By contrast, the more advanced methods from Suryasentana & Lehane (2014;2016) which incorporate an ultimate soil resistance, as well as an initial stiffness and a factor relating to the *GWT* depth in case of the latter mostly produce predictions of lesser accuracy.

However, in general it can be concluded that the *H-y* predictions produced with all the *CPT*-based *p-y* methods are of a relatively low accuracy. Even though (as can be seen in Appendix C) for most cases the most common value of η is between 0.8 and 0.9 (which is reasonably accurate), there is typically a large tail of much lower values. In comparison, the study from Burd, et al. (2019) which uses the same accuracy metric but a different 1*D* pile-response model developed in the PISA project (that incorporates additional soil reaction components), finds much more accurate predictions for a laterally loaded pile in marine sand. It should be noted that in this case the predictions from the 1*D* model were compared to data from pile load tests in a 3*D FEM* instead of those from field- or lab tests. Additionally, the soil reaction curves were obtained directly from those *PLT*'s, as opposed to the soil friction angle or the cone resistance as would be the case for the API- and *CPT*-based methods respectively. Nevertheless, the accuracies of their predictions all fall within the range of $0.89 < \eta < 0.98$. Because of the aforementioned difference in the way the soil reaction curves were obtained, worse performance is perhaps expected. However, the difference is of such magnitude that for the purpose of predicting the response of laterally loaded and mostly rigid piles, the accuracy of the *CPT*-based *p-y* methods should probably be deemed insufficient. This is perhaps not entirely unexpected, given the fact that the models were mainly derived from PLT's with substantially larger aspect ratios than a typical monopile.

Finally, as discussed in Section 2.3.2 the performance of the *p-y* methods with regard to prediction accuracy appears to be somewhat dependent on the dimensions and the rigidity of a given laterally loaded pile. For all methods except Novello (1999), performance is greater for relatively long- and flexible piles for the initial response. As previously mentioned, this makes sense considering the datasets from which they were developed, which mostly contain long, flexible piles. The relationships between prediction accuracy and pile characteristics seem less strong for greater normalized displacements. However, mainly the methods from Suryasentana & Lehane (2014) and Li, et al. (2014) do show better performance for shorter and more rigid piles. This is less easily explained and partly contradicts the findings for the initial response, though it should probably be given less weight.

In summary, keeping the aforementioned caveats into consideration the following conclusions can be drawn:

- All *CPT*-based *p-y* methods fail to properly capture weak behaviour at large displacements. This likely means that even Suryasentana & Lehane (2014;2016) don't accurately model ultimate soil pressures.

- All methods except that from Suryasentana & Lehane 2014 are less accurate at small- than at large displacements.
- All methods are on average conservative at a displacement of D/100
- All methods are either neutral or unconservative in their predictions at a displacement of D/10. This is potentially due to the absence- or overestimation of the ultimate soil pressure.
- Overall Dyson and Randolph (2001) and Li, et al. (2014) generate the most accurate predictions and Suryasentana & Lehane (2014;2016) generate the least accurate ones.
- All methods generate relatively inaccurate predictions in general when compared to a benchmark from Burd, et al. (2019).
- All methods except Novello (2001) are more accurate for long and flexible piles at small displacements.
- Suryasentana & Lehane (2014) and Li, et al. (2014) are more accurate for short and rigid piles at large displacements, though this trend is less clear.

Part 3. Centrifuge study on laterally loaded piles in sand: experimental methods

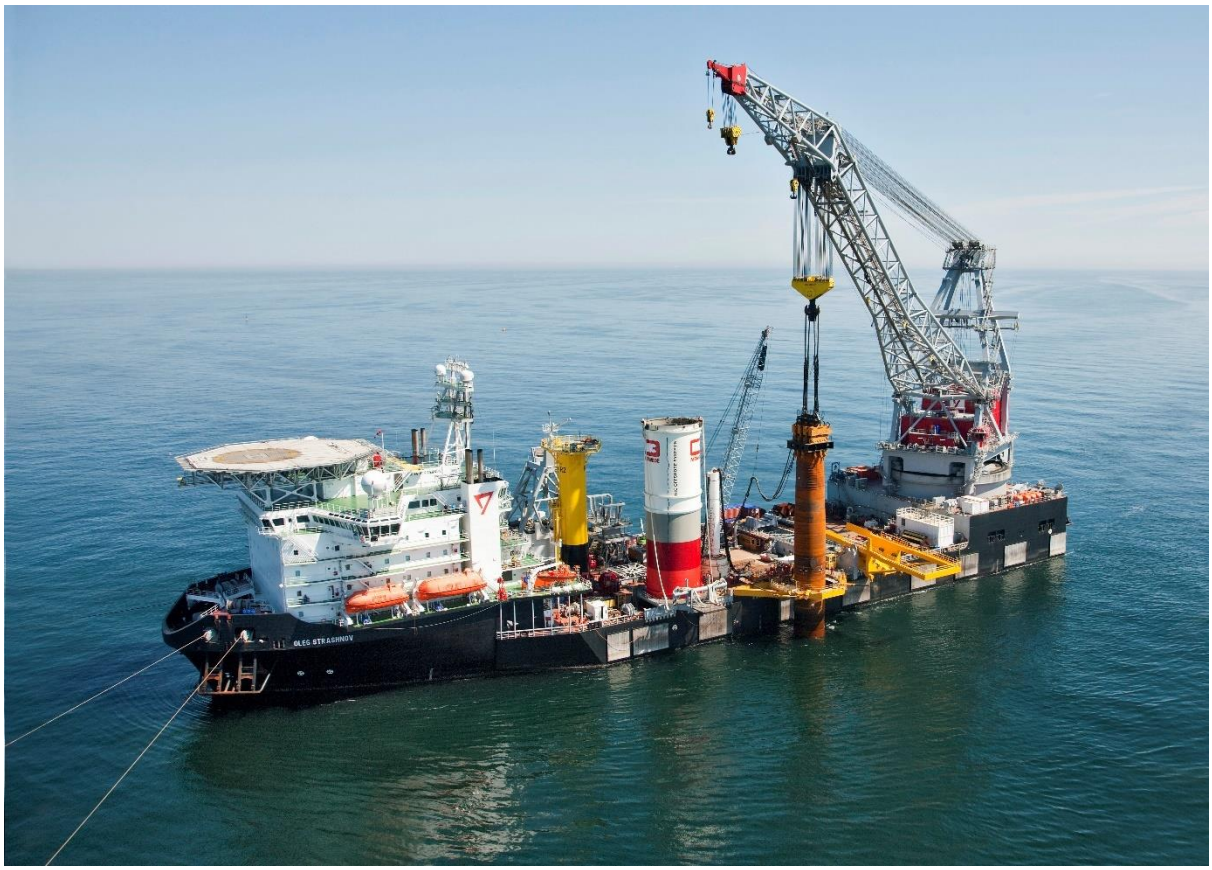

3.1 Centrifuge modelling

3.1.1 Centrifuge modelling principles

The main principle of geotechnical centrifuge testing is the enabling of small scale models to undergo the same stresses as a full scale prototype. This is achieved by accelerating the model. In a centrifuge test, a mass body is rotating at a constant radius and constant speed. The mass is experiencing a given radial centripetal acceleration $r\omega^2$, where r is the distance between the mass and the centrifuge spinning axis and ω is the angular velocity. By normalizing the centripetal acceleration with the gravitational acceleration g, a relationship can be defined between the centripetal acceleration and the factor n by which the acceleration is increased relative to the gravitational acceleration, as shown in Equation 36 (Muir Wood, 2004). An illustration of the concept of increased acceleration in a centrifuge is shown in Figure 47.

$$n = \frac{r\omega^2}{g} \tag{36}$$

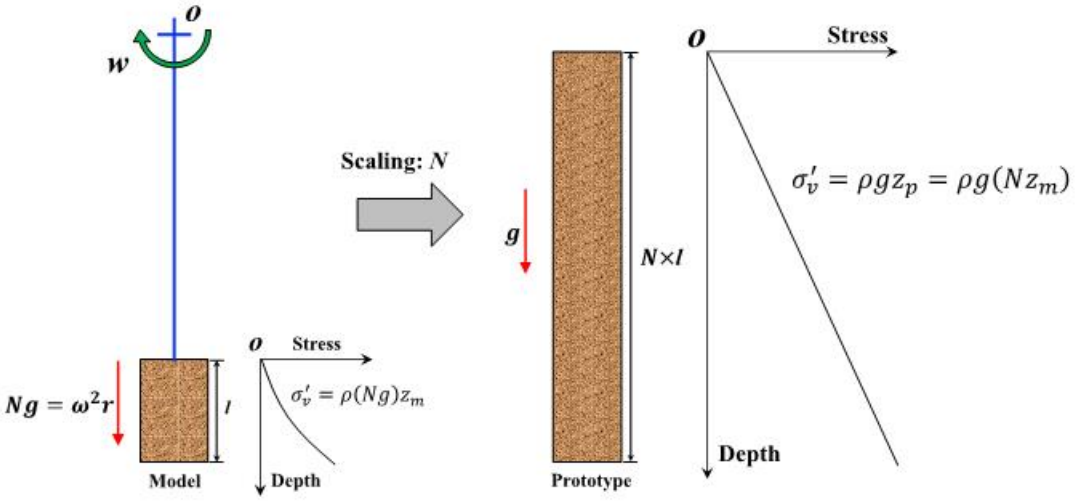

Figure 47: Conceptual illustration of the scaling of gravitational acceleration through rotation in a centrifuge

Centrifuge scaling laws describe the relationship between the magnitude of a physical quantity in a model and that in the corresponding prototype as a function of the acceleration level n. Relevant scaling factors for physical quantities at a given acceleration for this study are presented in Table 15 (Taylor, 1995).

Table 15: Scaling factors relevant to the centrifuge tests in this study

Physical quantity	Scaling factor (Model/Prototype)
Gravitational acceleration	N
Length	1/N
Area	$1/N^2$
Volume	$1/N^3$
Settlement	1/N
Stress	1
Strain	1
Force	$1/N^2$
Density	1
Mass	$1/N^3$
Flexural rigidity	$1/N^4$
Bending moment	$1/N^3$

At prototype scale, the gravitational acceleration of the earth is uniform over the entire soil depth range. In a scale model used in centrifuge testing the acceleration varies slightly over the depth as a result of a varying radius (Taylor, 1995). This leads to under-stress compared to the prototype in the top part of the model and over-stress in the bottom part. These stress deviations can be expressed as a function of the model height (H) and the nominal radius (r_e), as shown in Equation 37. Illustrations of the definitions of these terms can be seen in Figure 48.

$$R_{under} = R_{over} = \frac{H}{6 * r_e} \tag{37}$$

Considering a typical model height for this study of 145mm and a nominal radius for the TU Delft centrifuge of 1300mm (Allersma, 1994), the resulting under- or over-stress ratio comes to 1.86%. This is a relatively small deviation from the stresses in a prototype setting and it is therefore considered to be acceptable.

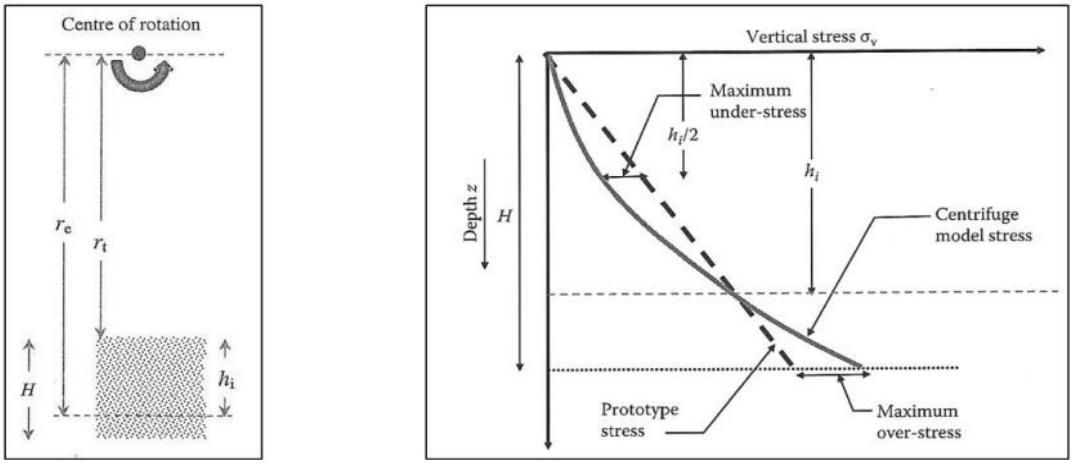

Figure 48: illustrations of radii and dimensions in centrifuge modelling (left) and over-/under-stress as a function of depth in a centrifuge model (right) (Madabushi, 2017)

3.1.2 TU Delft geotechnical centrifuge

The centrifuge tests were performed using the beam centrifuge at the Geo-Engineering section of the TU Delft. The nominal diameter of the rotating arm of the centrifuge is 2.5 m and it has a maximum carrying capacity of 30 kg at a maximum acceleration of 300 g (Zhang & Askarinejad, 2019). The strongbox with the experiment setup is placed on a platform that is mounted on a hinge, which causes the platform to swing upwards during a centrifuge flight. A schematic cross section of the centrifuge is shown in Figure 49**Error! Reference source not found.**. More specific information about- and applications of the TU Delft geotechnical centrifuge are described by Allersma (1994).

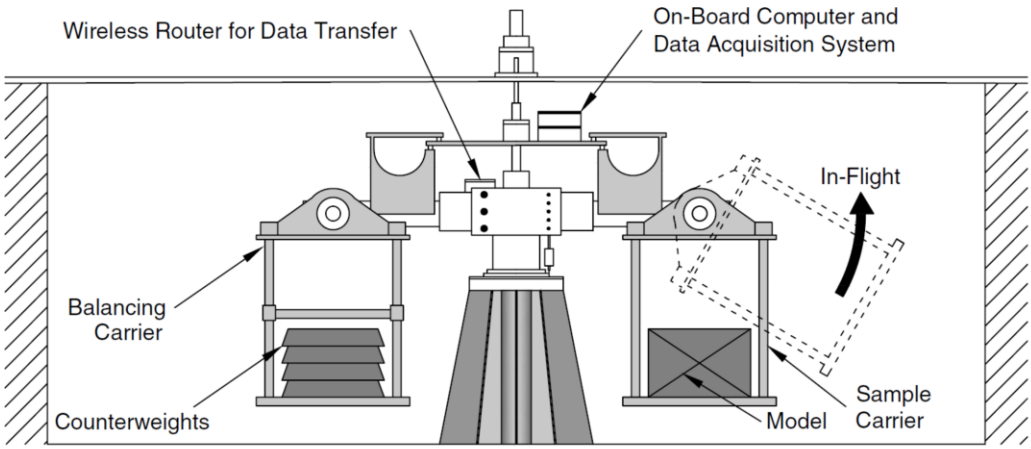

Figure 49: Schematic layout of the TU Delft geotechnical centrifuge

3.2 Mini-CPT

To further the CPT based design method for the laterally loaded pile, a mini-CPT was developed at TU Delft. Figure 50a shows a sketch of the developed mini-CPT at TU Delft centrifuge lab. As shown in the figure, the penetrator has a diameter of 7.5 mm with a standard 60 degrees cone tip. The cone tip is made of steel and connected with a steel inner rod. The inner rod has a diameter slightly smaller than the outer tube. A Teflon ring is installed between the inner rod and the outer tube, allowing to constrain the verticality of the rod without applying additional friction force.

During the test, the soil pressure acting on the cone tip is transferred to the inner tube and measured as a total force by the load cell connected with the inner tube. The load cell has a measurement as range of 2.65 kN, which is equal to a tip resistance (q_c) of 60 MPa. The whole penetrator is designed in a modular mode, which allows for changing the component independently based on the requirement of the tests. The penetrator has a maximum depth of 150 mm, which is equivalent to a depth of 15 m in protype at a centrifuge acceleration of 100g. The mini-CPT can be easily installed on the load actuator in the lab. A photo of the mini-CPT installed on the actuator from previous test is presented in Figure 50b.

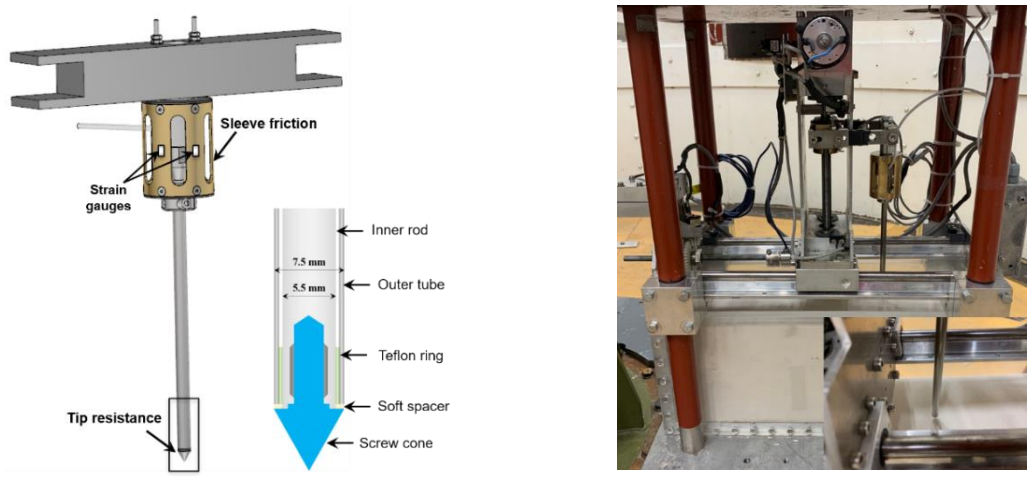

Figure 50: The TU delft mini-CPT schematically (a) and in real life (b)

3.3 Sample preparation

3.3.1 Soil properties

The soil used in the centrifuge tests of this study is Geba sand. This is a sub-angular, sub-rounded sand supplied by Eurogrit. The most important properties of this sand are summarised in Table 16. More detailed information on it can be found in Zhang & Askarinejad (2019). For Geba sand and the selected pile diameter of 18mm, the ratio of the pile diameter over the average grain size (D/d_{50}) is about 164. This is larger than the ratios suggested for laterally loaded piles by Remaud (1999), Nunez et al. (1988) and Klinkvort (2012), which are 45, 60 and 121 respectively.

Table 16: Properties of the Geba sand

Property	**Sand**
Group symbol based on USCS[#]	SP
Median grain size, d_{50} (mm)	0.11
Curvature coefficient, Cc	1.24
Uniformity coefficient, C_U	1.55
Specific gravity, G_s	2.67
Maximum void ratio, e_{max}	1.07
Minimum void ratio, e_{min}	0.64
Critical friction angle, φ (º)	35

Note: [#] Unified Soil Classification System (USCS) (ASTM D2487)

3.3.2 Sample preparation procedures

Method A

The first method for the preparation of sand samples involves the sand raining machine developed at the TU Delft centrifuge lab. As shown in the Figure 51, the sand is stored in a triangle-shaped hopper first. A line-styled gap located at the bottom ridge of the sand hopper can be opened manually. The open width can be adjusted by a spiral calliper. By screwing the spiral calliper, the gap width can be adjusted to produce different thicknesses of the "sand curtain". This allows to control the sand grains' raining intensity and generate different relative density seabed. Meanwhile, the height of sand hopper can also be adjusted by driving two vertical servo motor belts. In the end, by changing the opening, the height and the speed, sand samples with a wide range of density can be prepared.

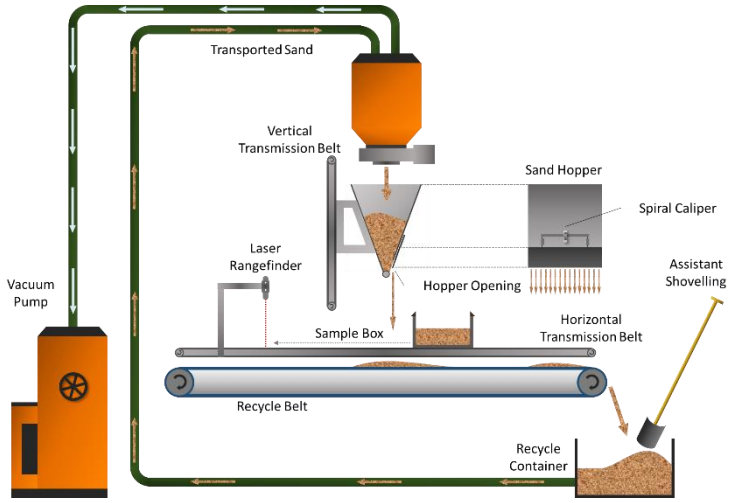

Figure 51: Schematic illustration of the TU Delft Sand rainer

For the Geba sand used in this study, extensive calibration work has been performed as shown in Figure 52. Based on the calibration results, uniform sand sample with a relative density ranging from 20% to 80% can be prepared.

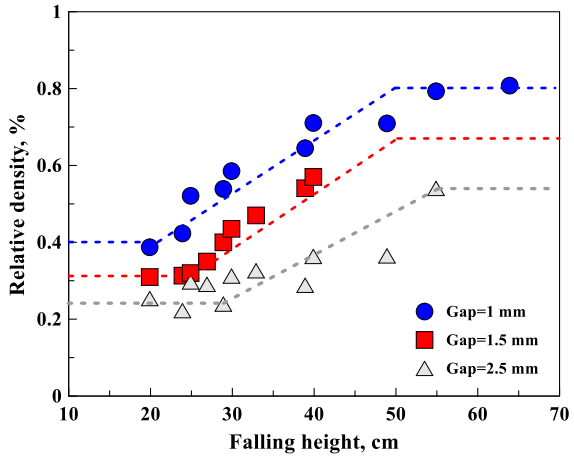

Figure 52: Calibration results of the Geba sand for the sand rainer

Method B

The second sample preparation method is based on hand raining, combined with vibration to densify the sample up to the required relative density. As can be seen in Figure 53a, the sand is poured into a bucket with a row of holes in the bottom. This produces a sand curtain, which is moved back and forth across the model box, at a constant height from the sand surface.

(a) (b)

Figure 53: Illustrations of the sand raining- (a) and vibrating (b) processes

Subsequently, the model box with the sample is placed on a platform (as shown in Figure 53b) and vibrated at a set intensity for a varying amount of time, depending on the required relative density. Finally, the sample is placed on a scale and weighed, after which the achieved D_r can be checked using Equations 38 and -39.

$$e = \left(\frac{G_s \gamma_w}{\gamma_d}\right) - 1 \tag{38}$$

$$D_r = \left(\frac{e_{max} - e}{e_{max} - e_{min}}\right) \tag{39}$$

3.3.3 Validation of preparation techniques through CT scanning

The hand raining process from method B is less controlled than the mechanical sand rainer from method A, but it is less time consuming. Furthermore, the vibration that follows the former might destroy some of the internal layering structure that results from the raining process and may therefore lead to a more homogenous sample. This is theoretically beneficial to the repeatability and the representativeness of the centrifuge tests.

To check the homogeneity- and compare the internal structure of samples produced with the two aforementioned methods, CT scans were conducted of several samples. Subsequently, using the average relative density that can be calculated from the weight of a sample and the darkness of the greyscale from the CT image, cross sections from these scans were analysed to quantify the relative density of the sand in 2D throughout the sample.

The procedure for scanning the sand samples consists of either one of the aforementioned sand deposition methods in the model box. Two types of model boxes are used for this purpose. The first one is a cylindrical plastic box, with inner dimensions of 250x170mm (diameter x height). The second one is a rectangular wooden box with inner dimensions of 410x150x165mm (length x width x height). Optionally, a pvc pipe is installed in the sample at 1*g* using a special device to hold it in place, in order to assess the influence of the installation procedure on the soil density around the model pile (discussed further in Section 3.5.1). Finally, the sample is loaded into the TU Delft Geoscience & Engineering macro CT-scanner. This scanner is a Siemens Somatom Volume Zoom, originally meant for medical applications with a maximum resolution of 0.3mm.

Figure 54 shows a sample that was prepared with the sand rainer in the cylindrical model box, with an average D_r of 0.83. The sample shown in Figure 55 was prepared through hand raining and has an average D_r of 0.75 after vibration. It is clear that both sample preparation techniques result in a layering in sand density. However, where the spatial variation in density is mostly constant throughout the sample when the sand rainer is used (with only a looser layer at the very top), there is a clear difference between top- and bottom in the hand rained sample. It appears that the vibration impacts the top of the sample much more than the bottom, resulting in a less layering and a higher density. This is not necessarily a problem (especially since the model piles with L=95mm mostly fall within the uniform dense zone), but when considering the results it should be taken into account that most of the soil around the pile is denser than the average value of the sample suggests.

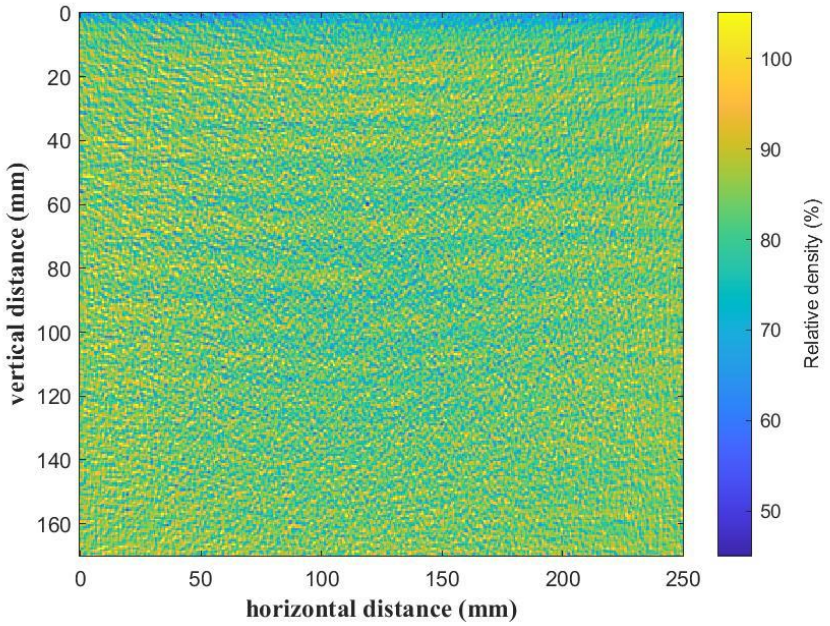

Figure 54: Processed CT scan of a sample prepared with the sand rainer with an average Dr of 0.83

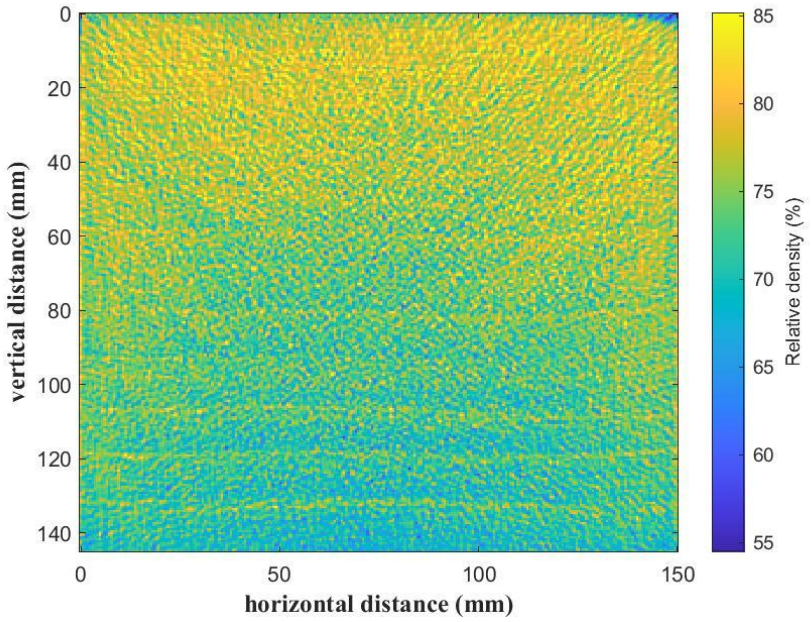

Figure 55: Processed CT scan of a sample prepared by hand raining with an average Dr of 0.75

Something that speaks in favour of the hand raining preparation method is that it has a narrower overall relative density distribution. As is shown in Figure 56, the difference between the 2σ values for the relative density in the hand raining sample is 0.83-0.66 = 0.17, whereas for the sand rainer sample it is 1.0-0.67 = 0.33. This means that there is overall less variation in density for samples that are prepared by hand raining.

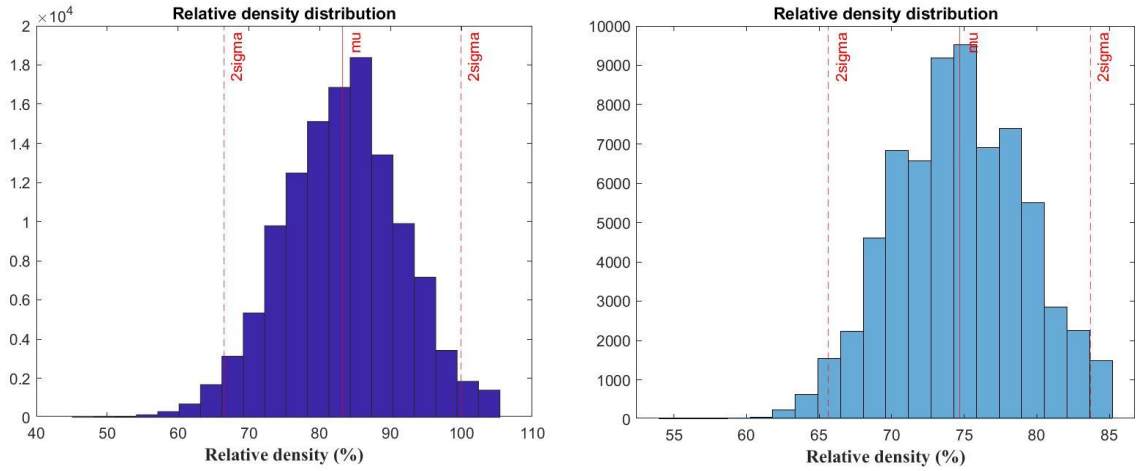

Figure 56: Relative density distributions of the sample prepared with the sand rainer (left) and the sample prepared by hand raining (right)

3.3.4 Repeatability CPT tests & interchangeability sample preparation methods

In order to assess the repeatability of the CPT tests and also check the consistency of the results for the different sample preparation methods, a number of tests were performed on samples with an overall relative density of 80%. Figure 57 shows the results from these tests.

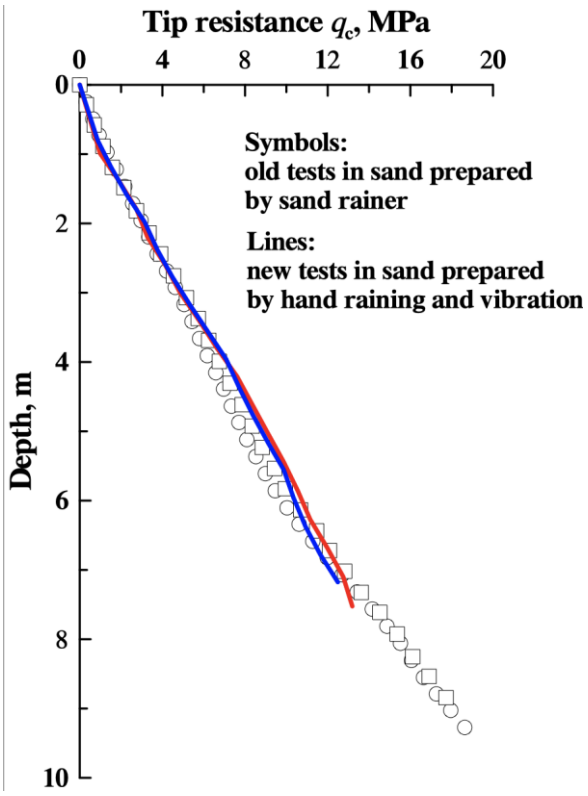

Figure 57: CPT profiles from tests on samples with similar relative density but different preparation techniques

It can be concluded that for an equal D_r, the measured tip resistances are nearly identical between tests. Additionally, the differences between sample preparation methods seem to be negligible. Because of this and the fact that both preparation methods produce acceptably homogeneous samples, the hand raining method is chosen for the monotonic centrifuge pile load tests since it is considerably less cumbersome and time-consuming.

3.4 Model piles

3.4.1 Model piles & instrumentation

Based on the pile dimensions used in existing offshore wind farms, two typical pile aspect ratios are selected in this study, namely *L/D* = 5 (for pile 1 with *D* = 18mm) and *L/D* = 3.6 (for pile 2 with *D* = 25mm) (Negro et al. 2017). However, only the 18 mm diameter model was instrumented with the strain gauges for measuring the bending moment and derive the p-y curves. The model piles are made of aluminium tubular. The wall thickness is set to be 1 mm for pile 1 and 1.5mm for pile 2. For the centrifugal acceleration most frequently used in this study (i.e. 100g), the corresponding prototype monopile diameters are 1.8 m for pile 1 and 2.5m for pile 2. According to the scaling laws presented

in Table 15, the wall thicknesses in prototype are t = 1mm × 100 = 0.1m and t = 1.5mm x 100 = 0.15m respectively when the pile is made of aluminium.

Poulos and Hull (1989) pointed out that the behaviour of laterally loaded pile is mainly controlled by the flexural rigidity (i.e. E_pI_p, where E_p is Young's modulus of pile and I_p is section area moment of inertia of the pile). Therefore, by assuming the same flexural rigidity, the equivalent wall thickness of monopile made of steel can be calculated as follows:

$$E_{\text{aluminium}}\frac{\pi(D^4-(D-2t_{\text{aluminium}})^4)}{64}=E_{\text{steel}}\frac{\pi(D^4-(D-2t_{\text{steel}})^4)}{64} \qquad (40)$$

where $E_{\text{aluminium}}$=72 MPa is the Young's modulus of aluminium; E_{steel}=210 MPa is the Young's modulus of steel; D is pile diameter; $t_{\text{aluminium}}$ is the wall thickness of monopile made of aluminium; t_{steel} is the wall thickness of monopile made of steel. Therefore, the calculated wall thickness of the steel monopile is 0.031m for pile 1 and 0.045 for pile 2. The D/t value for the steel prototype pile is 58 for pile 1 and 51 for pile 2, which matches the expected range from 39 to 80 presented by Byrne et al. (2015b) for offshore wind turbines. In addition, the API (2011) requires that the minimum wall thickness of monopile is D/100 + 6.35 mm. The selected wall thickness satisfies the requirement of the API code for both piles.

Strain gauges are instrumented on model pile 1 to be able to calculate the bending moment along the pile during different stages of the tests. The bending moment is used to derive the *p-y* curves at different depths according to Equation 8. As shown in Figure 58, a total of 15 of strain gauges are installed on the embedded parts of the model pile with an aspect ratio of 5. Two pairs of additional strain gauges are also installed above the ground surface, which can be used to double check the moment and force applied by the actuator.

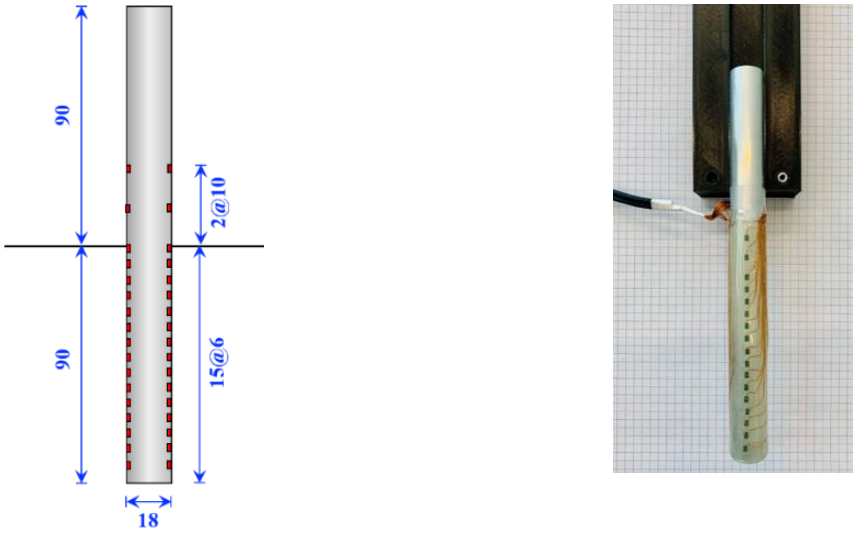

(a) (b)

Figure 58: Schematic (a) and real life (b) strain gauge instrumentation plan for the model

Considering the small diameter of the model pile, the FLA-03-23-1LE strain gauge (Tokyo Measuring Instruments Lab. 2020) is used, which has a resistance of 120 Ω and a length of 2 mm. The strain gauge can accurately measure the strain to a level of 10^{-6}. The extension wire of the strain gauge is made of polyurethane with a diameter of 0.14 mm. Photos of a typical strain gauge and the instrumented model pile in a strain gauge calibration test setup are presented in Figure 59.

(a) (b)

Figure 59: Photo of (a) strain gauge, (b) instrumented pile

3.4.3 Strain gauge calibration

In order to verify the accuracy and consistency of the used strain gauges, a cantilever beam test was performed on the 18mm diameter model pile. A moment was induced in the pile by loading one end while the other was fixed and subsequent voltage measurements of the strain gauges were recorded. In Figure 60 can be seen a plot of these measurements for three strain gauges at 0.067m, 0.079m and 0.095m from the loading point. It shows both that the measurement closely approximate a linear trend and that this trend is very consistent between strain gauges. Therefore they are deemed accurate and reliable.

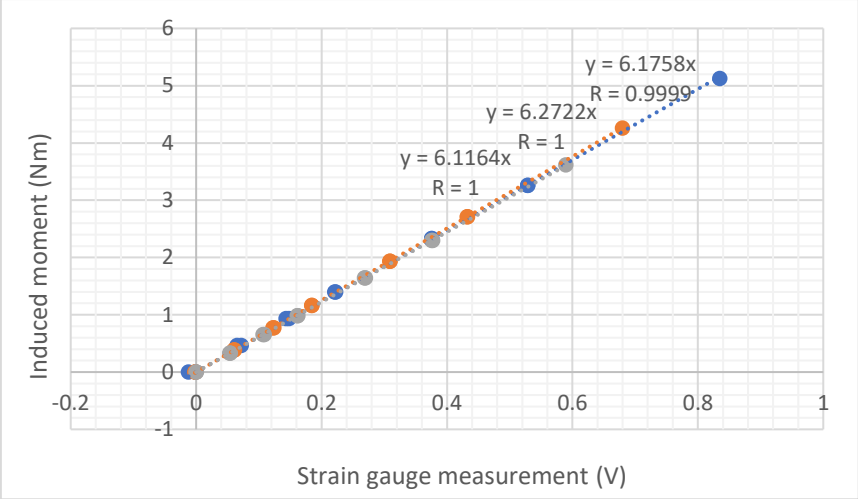

Figure 60: Calibration results for three strain gauges at different places along the model pile

3.5 Two-dimensional loading system

3.5.1 Loading system specifications

In the centrifuge tests, a two-dimensional servo actuator is used to apply lateral loads on the pile head (as shown in Figure 61a). It is capable of applying loads under either load control- or displacement control conditions. The applied lateral loads are measured continuously using a load cell during the tests. Two displacement sensors are also installed at different heights to measure the pile deflection. The measured deflection is used to calculate the displacement and rotation at the mudline. The pile is loaded laterally and monotonically at an eccentricity of either $e = L$ or $e = 2L/3$. The load is applied to the pile through a specially designed 3D printed component that can be lowered to the correct eccentricity, as shown in Figure 61b.

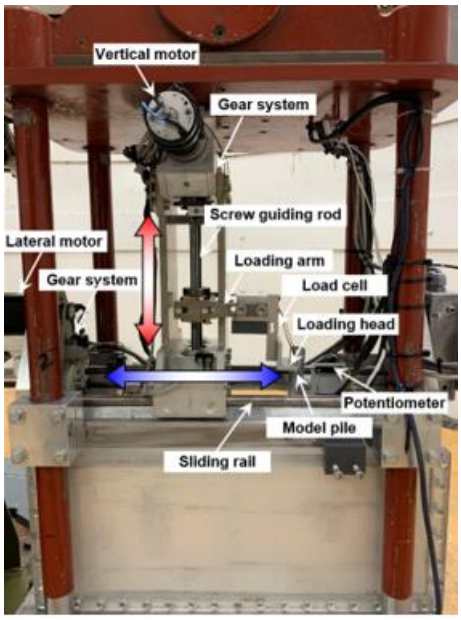

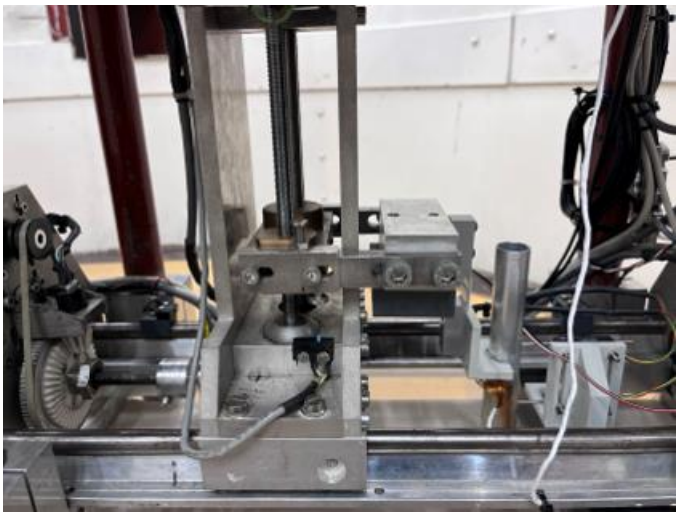

(a) (b)

Figure 61: A typical model setup for the model pile, (a) labelled picture of the test setup, (b) close-up of a typical test setup

3.5.2 Pile installation procedure

A monopile foundation will normally be hammered to the target depth. However, it is difficult to simulate the installation process and apply the lateral loading at the same time in the centrifuge. Although jacking the pile at Ng is an option, the required force for the installation at Ng is out of the limit of the actuator. Furthermore, the installation by hammer or jacking will disturb the soil stress state around the model pile. This influence might be minimal for a prototype monopile due to the large pile diameter comparing with the disturbed interface. However, due to the small diameter of the model pile, the influence of installation will be much larger for the tests in the centrifuge. Therefore the installation is completed using the vertical actuator at 1g, similar to a "wished in place" condition. This means that installation effects of monopile foundations are not accounted for.

In order to assess the disturbance of the soil surrounding the pile that is caused by the aforementioned installation process, more CT scans were made of samples before- and after pile installation. In this case a pvc pipe was installed instead of the normal aluminium one in order to show both the soil in- and outside of the pile. Figure 62 and Figure 63 show a sample with a mean relative density of 75% that was prepared using the hand raining method, with- and without a pile installed. They show that although there is clear and substantial soil disturbance inside the model pile (mainly due to plugging), the disturbance of the soil surrounding the pile is limited. This means that the cone resistance profiles from undisturbed samples found in the centrifuge tests will likely be reasonably representative for the soil surrounding the installed piles. It should be noted that Figure 63 seems to show a pile that extends up to the bottom of the model box. However, this is due to visual artifacts from the CT scan.

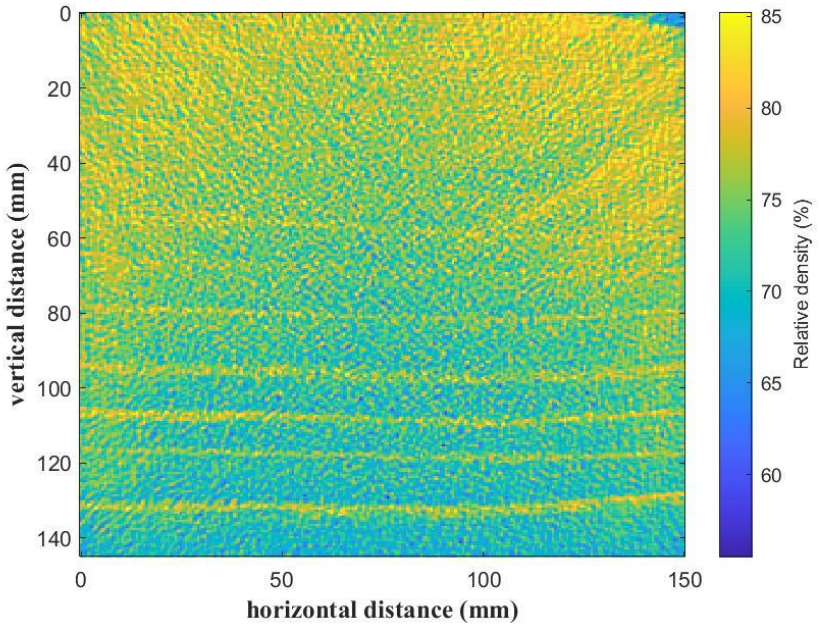

Figure 62: Processed CT scan of an undisturbed sample with mean Dr of 75% prepared through hand raining

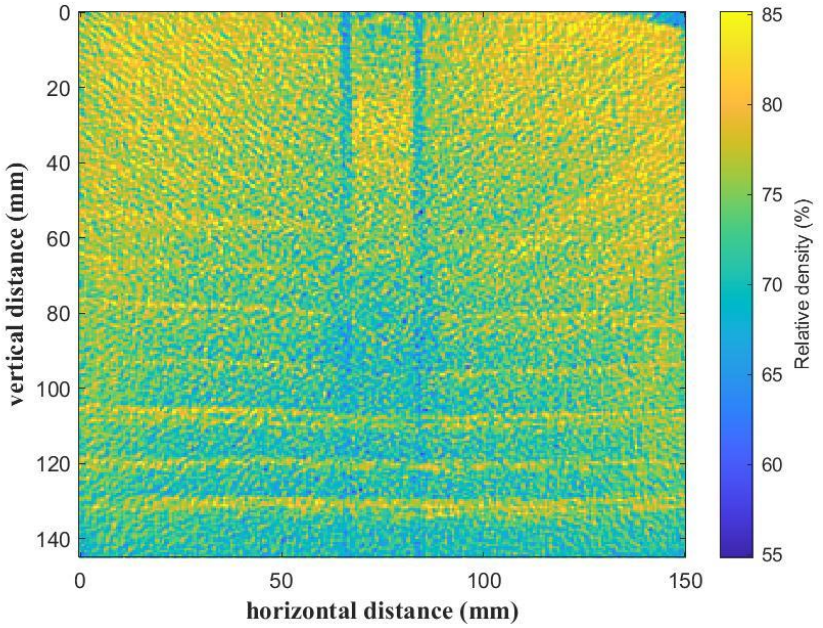

Figure 63: Processed CT scan of a sample with mean Dr of 75% prepared through hand raining with pile installed

3.5.3 Loading system performance

Testing has been done to show the reliability of the actuator. Figure 64 shows the results from a load-controlled test on the horizontal actuator. The input force was cyclically varied and subsequently measured using a load cell. It can be seen that the force produced by the actuator very closely and consistently follows the intended target curve.

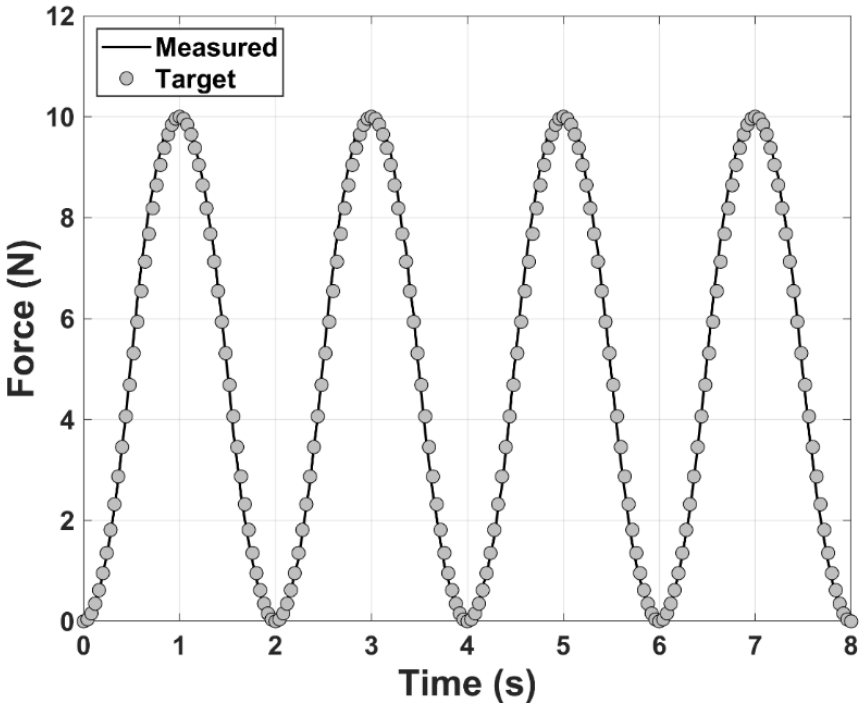

Figure 64: Target- and measured loads from a cyclical test of the horizontal actuator

3.7 Testing programme

Due to unforeseen difficulties with the vertical actuator, it was decided to minimize the number of CPT tests. For this reason, CPT tests were performed only at 50g and 100g acceleration and solely on samples with a relative density of 0.8. As can be seen in figure, previous CPT tests in the centrifuge have shown that equal acceleration levels and equal soil relative densities lead to very similar results (see Figure 57 from Section 3.3.4). Thus, a single CPT test was used for corresponding load tests of equal N and D_r. In order to increase the variety of pile load test scenarios and therefore the general applicability of the results, the loading eccentricity was also varied. Even though only samples with a relative density of 0.8 were used (as opposed to a range of loose-dense samples), these tests should still be representative of offshore soil conditions in much of Northern Europe (Bjerrum, 1973). Finally, for tests 5 through 8 a pile with a diameter of 25mm without strain gauges was used. The data from these centrifuge tests are included in the analyses from Part 2 and Section 4.3 of this study, but these measurements cannot be used to construct *p-y* curves and are therefore excluded from the analysis in Section 4.2 . Tests 9 through 12 are only used for the analysis in Section 4.3 , because no CPT-data could be obtained for tests at 25g.

Table 17: Test matrix for centrifuge pile load tests

Test NO.	D_r	*D* (mm)	*L* (mm)	*e* (mm)	*N* (g)	Strain gauges *(y/n)*
1	0.8	18	90	90	100	Yes
2	0.8	18	90	60	100	Yes
3	0.8	25	90	90	100	No
4	0.8	25	90	60	100	No
5	0.8	25	90	90	100	No
6	0.8	18	90	90	50	Yes
7	0.8	18	90	60	50	Yes
8	0.8	25	90	90	50	No
9	0.8	18	90	90	25	Yes
10	0.8	18	90	60	25	Yes
11	0.8	25	90	90	25	No
12	0.8	25	90	60	25	No

Part 4. Centrifuge study on laterally loaded piles in sand: interpretation of the results

4.1 Load-deflection & bending moment comparisons

In order to assess the performance of the *CPT*-based *p-y* models for the cases of rigid laterally loaded piles presented in this study, both their predicted load transfer- and *p-y* curves are compared. In this section load-deflection curves and bending moment profiles are presented, including those predicted by the API model.

4.1.1 Derivation of groundline rotation and -displacement

If we want to most accurately determine the pile rotation and displacement at the mudline throughout a load test, it is not sufficient to use the *LVDT* displacement measurements and the difference in height between them in order to derive the pile rotation angle. This is because it inherently requires the assumption that the pile rotates entirely rigidly. Therefore a more sophisticated method from Burd, et al. (2020) is used to calculate the groundline rotation, where the above-ground structure is modelled as a Timoshenko beam with a given flexural- and local shear stiffness.

In this, the bending moment *M* can be defined as

$$M = -EI\frac{d\psi}{dz} \tag{41}$$

where *EI* is the local flexural stiffness, ψ is the rotation of the pile cross section and *z* is the depth (positive in the downward direction, z=0 at the groundline). The rotation of the neutral axis of the pile θ (which is equal to $-(\frac{dv}{dz})$ where *v* is the lateral displacement) can be defined as

$$\theta = \psi + \gamma_{xz} \tag{42}$$

where γ_{xz} is the shear strain, which in Timoshenko beam theory is assumed to be uniform across the cross section and is given by

$$\gamma_{xz} = \frac{S}{\kappa AG} \tag{43}$$

where *S* is the shear force and *κAG* is the local shear stiffness (where *κ* is a shear factor taken at 0.3). *E* and *G* are assumed to be 69GPa and 26.54GPa respectively. The bending moment and the shear force induced in the above ground structure can be defined as

$$M = H(h + z) \tag{44}$$

$$S = \frac{dM}{dz} = H \tag{45}$$

where *e* is the loading eccentricity. Equations 41 and -43 through -45 are substituted into Equation 42 and subsequently integrated to produce

$$\theta = -\frac{H}{EI}\left(hz + \frac{z^2}{2}\right) + \left(\frac{H}{\kappa AG}\right) + a \tag{46}$$

and integrated again to give

$$v = \frac{H}{EI}\left(\frac{hz^2}{2} + \frac{z^3}{6}\right) - \left(\frac{H}{\kappa AG} + a\right)z + b \tag{47}$$

where *a* and *b* are parameters to be determined iteratively for every loading step and *b* is equal to the groundline displacement v_0. Solving Equations 46 and -47 46 and using the LVDT- and load cell data finally allows for the calculation of the groundline rotation and displacement of the pile.

4.1.2 Load-deflection response

Figure 65 shows the load-deflection responses for the eight centrifuge tests performed at 50- and 100g. The tests at 25g have not been included, because no good *CPT* data could be gathered from them and therefore no pile-response simulations could be performed with the *CPT*-based *p-y* models. From the generated load-deflection curves, a few observations can be made. Firstly, as shown previously by Choo & Kim (2015), it is very clear that the stiffness of the initial response predicted by the API model is far too great. This means that it is consistently unconservative in the displacement range that is relevant to the SLS and ULS ($y_0 < 0.10D$) for a monopile foundation and it supports the notion that as a design method for short and rigidi piles it can be considered unsafe.

By contrast, beyond a groundline displacement of around 0.15*D* the API model seems to outperform the CPT-based models, because unlike them it shows a fast decrease in stiffness and it reaches a clear ultimate resistance. However, the transition from initial stiffness to ultimate resistance is actually too abrupt and the predicted ultimate resistance is consistently lower than the measurements.

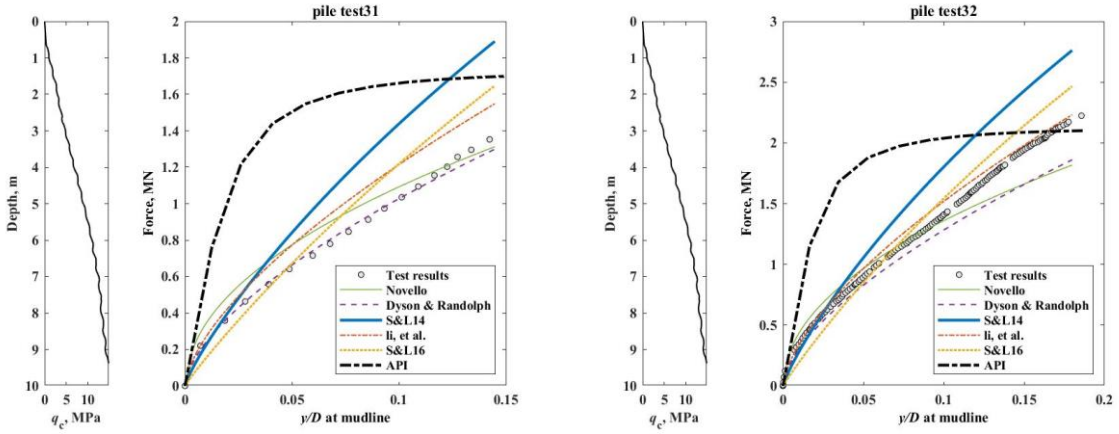

(a) (b)

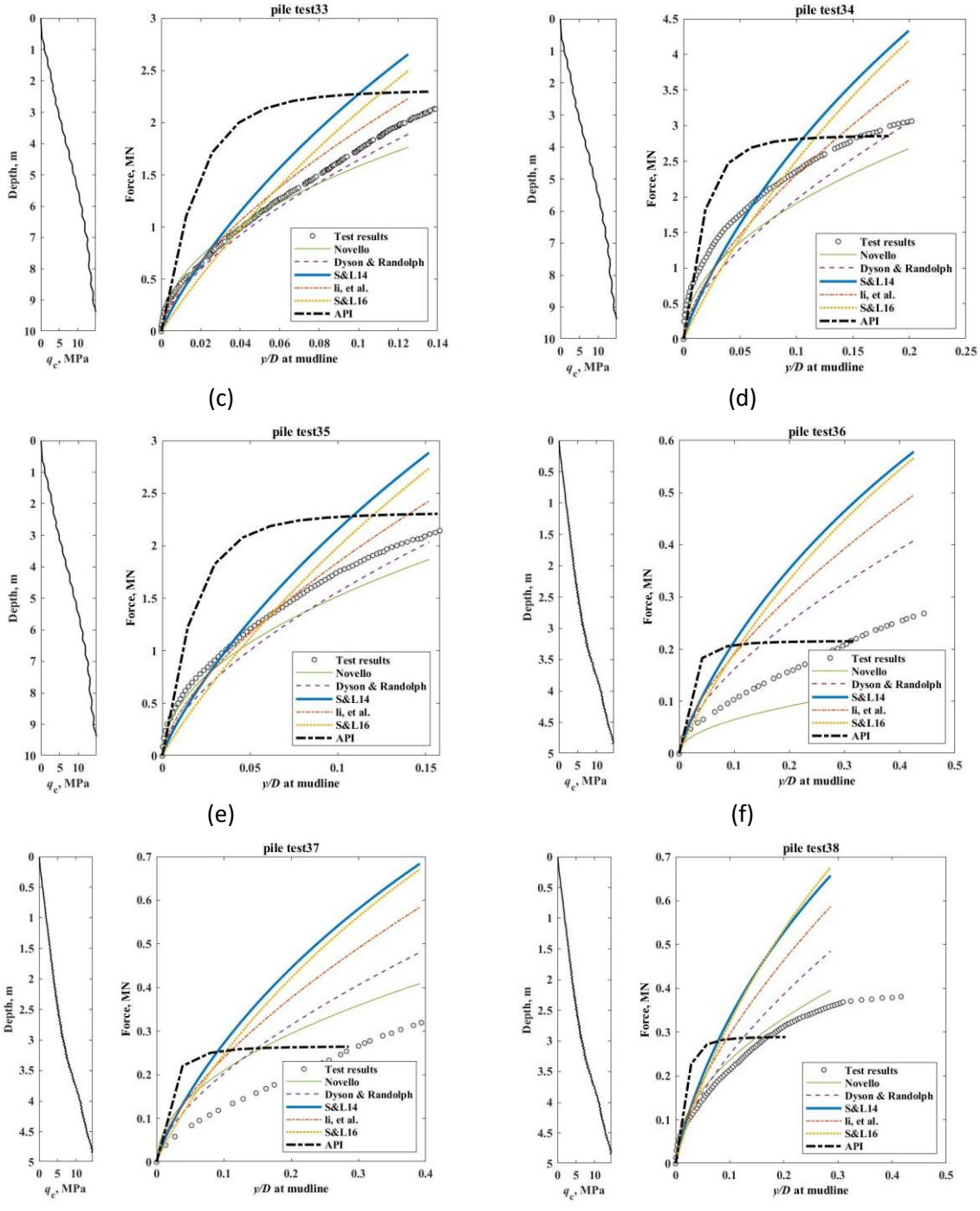

Figure 65: Predicted and measured load-deflection response for PLT31 through 38

4.1.3 Bending moment

Additionally to the comparison of load-deflection response for pile tests 31 through 38, a few observations can be made from the predicted bending moments. Figure 66 shows the bending moment profiles at the maximum groundline displacement for the aforementioned tests. Unsurprisingly, the magnitude of the predicted bending moments differs more between models for the cases where the predicted loads differ more as well. Furthermore, the bending moment is consistently greatest at a depth of around 1D. Finally, the models from Novello (1999) and API (2011) predict the largest bending moments at a slightly greater depth than the other models.

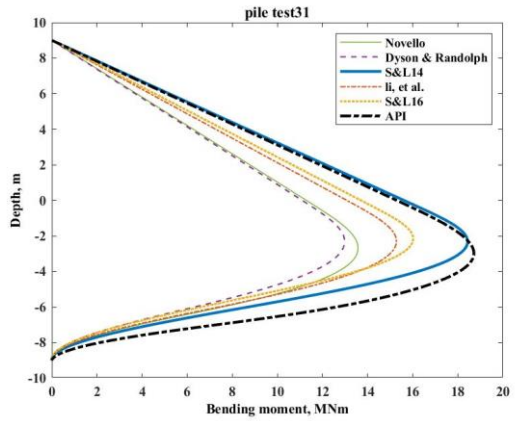
pile test31
Novello
Dyson & Randolph
S&L14
li, et al.
S&L16
API
Depth, m
Bending moment, MNm

(a)

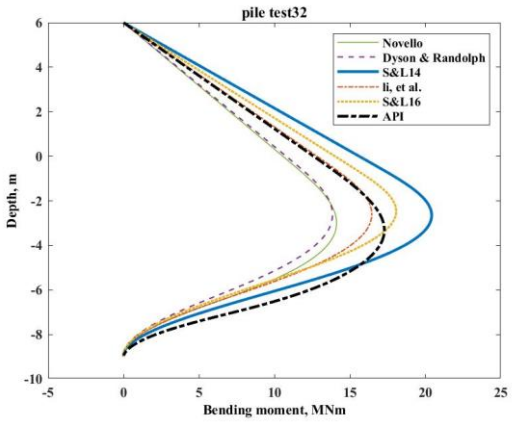
pile test32
Novello
Dyson & Randolph
S&L14
li, et al.
S&L16
API
Depth, m
Bending moment, MNm

(b)

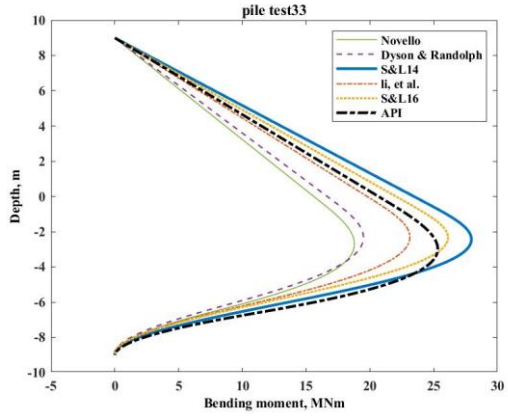
pile test33
Novello
Dyson & Randolph
S&L14
li, et al.
S&L16
API
Depth, m
Bending moment, MNm

(c)

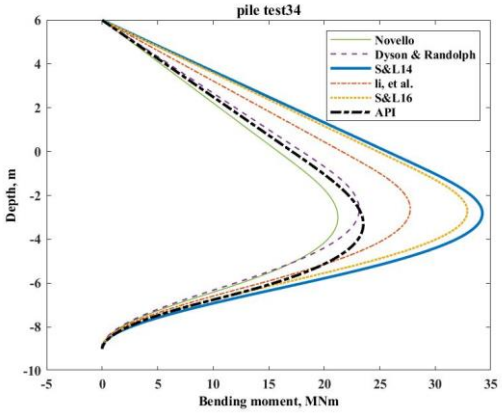
pile test34
Novello
Dyson & Randolph
S&L14
li, et al.
S&L16
API
Depth, m
Bending moment, MNm

(d)

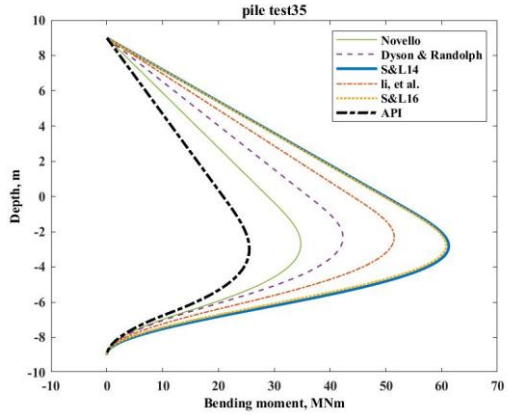
pile test35
Novello
Dyson & Randolph
S&L14
li, et al.
S&L16
API
Depth, m
Bending moment, MNm

(e)

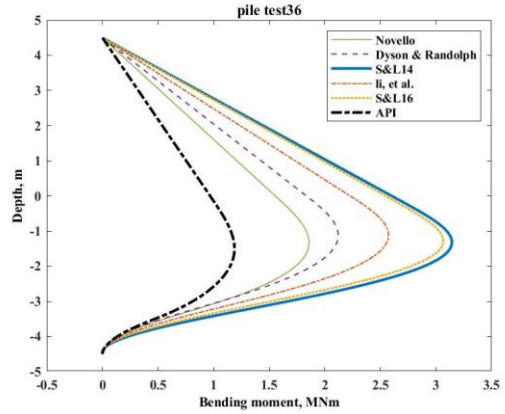
pile test36
Novello
Dyson & Randolph
S&L14
li, et al.
S&L16
API
Depth, m
Bending moment, MNm

(f)

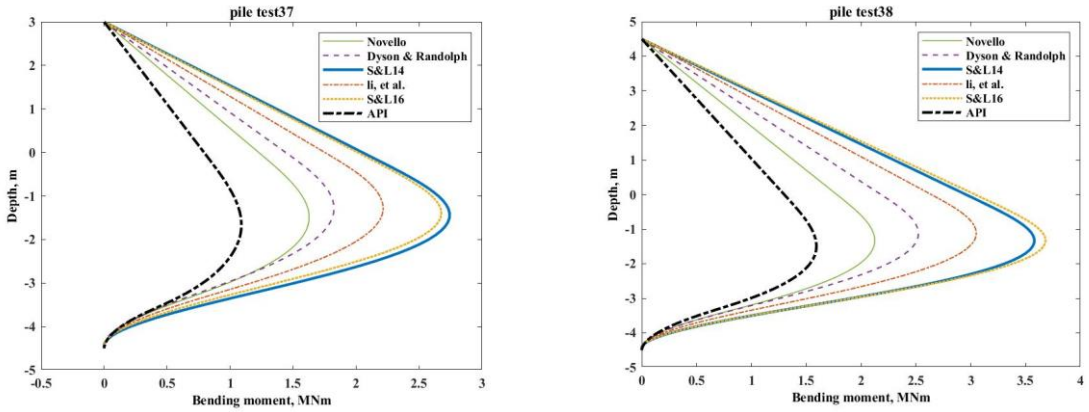

(g) (h)

Figure 66: Predicted bending moment profiles at maximum displacement for PLT31 through 38

4.2 Pile-soil interaction & *p-y* predictions

The main aims of the centrifuge pile load tests in this study are twofold: to assess the accuracy and behaviour of the predictions of several *CPT*-based *p-y* methods at various depths and to assess the role of pile diameter and stress level on the load transfer response of a rigidly rotating pile to see whether the responses can be unified through normalization. This is done through lab tests on a rigid laterally and monotonically loaded pile in a homogenous dense sand. Originally, all tests on the 18mm diameter pile were meant to be used in the analysis of both of these parts. However, due to problems with the measurements of the bending moment data, ultimately only PLT 32 (test number 2 from Table 17) is used to analyse *p-y* predictions.

As is previously explained in Section 1.2.3, deriving rotation- or deflection profiles for a pile load test involves the single- or double integration of the bending moment profiles respectively. Conversely, the shear force- and soil resistance profiles are derived through single- and double differentiation of the bending moment profiles respectively. Furthermore, as stated by Yang & Liang (2019), the integration of discrete strain- and bending moment data with respect to depth does not incur numerical errors and likely even minimizes measurement errors of the strain gauges. However, (double) differentiation of discrete data will amplify measurement error and therefore produce highly inaccurate soil resistance profiles. Therefore, several numerical techniques have been proposed to fit accurate continuous curves to discrete bending moment data to maximize the accuracy of the resulting resistance profiles.

4.1.1 Bending moment profiles

As mentioned, several curve fitting techniques have previously been proposed to fit continuous curves to discrete bending moment data, including high-order global polynomial-, piecewise polynomial-, cubic spline- and cubic to quintic B-spline curve fitting. Yang & Liang (2019) and Haiderali & Madabhushi (2016) both compared several of these techniques through field load tests and 3D *FEA* respectively. The former found that a piecewise cubic polynomial fitting method lead to the smallest error in the deflection predictions resulting from the *p-y* method. The latter found the cubic- and cubic B-spline methods to provide optimal p-y curves for both the small- and large diameter pile. In this case however, a modified 5^{th} order polynomial function (see Equation 48) is used. This is because cubic spline or piecewise polynomial methods, though very accurate when applied to good datasets with

little error, can easily lead to irregular and inaccurate fitted *M* profiles when there are insufficient numbers of data or the error is too large as was demonstrated by Truong (2017).

$$\varphi = \frac{M}{EI} = az^5 + bz^4 + cz^3 + dz + e \tag{48}$$

The polynomial function is solved using the non-linear least-squares method. To derive the deflection profiles, the curvature (φ) is integrated twice. To solve for the integration constants, the groundline displacement and -rotation are used. These are in turn determined using Timoshenko beam theory, as described in section 4.1.1. This has previously been shown to be valid for short, drilled shafts (Yang, et al. 2019).

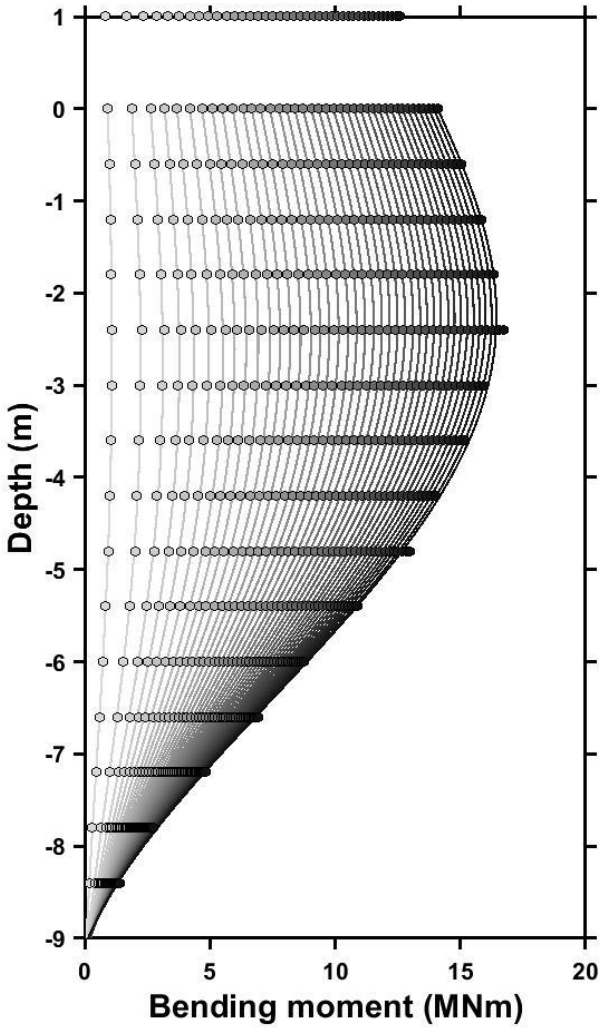

Figure 67: Bending moment data and fitted curves for PLT 32

As can be seen in Figure 67, the resulting fitted bending moment curves are a reasonable match to the measurement data points from the load test. Furthermore the curves are smooth and do not show any irregularities that might lead to unrealistic outcomes after double differentiation.

4.1.2 Shear force profiles

After differentiating the fitted bending moment profiles, the shear force profiles shown in Figure 68 are produced. They show reasonable and expected results, with a maximum shear force at the depth with the maximum bending moment slope which is around the centre of rotation of the pile. Furthermore, there is a shear force of zero at the depth with peak bending moment and the derived curves match the plotted force measurements at the mudline.

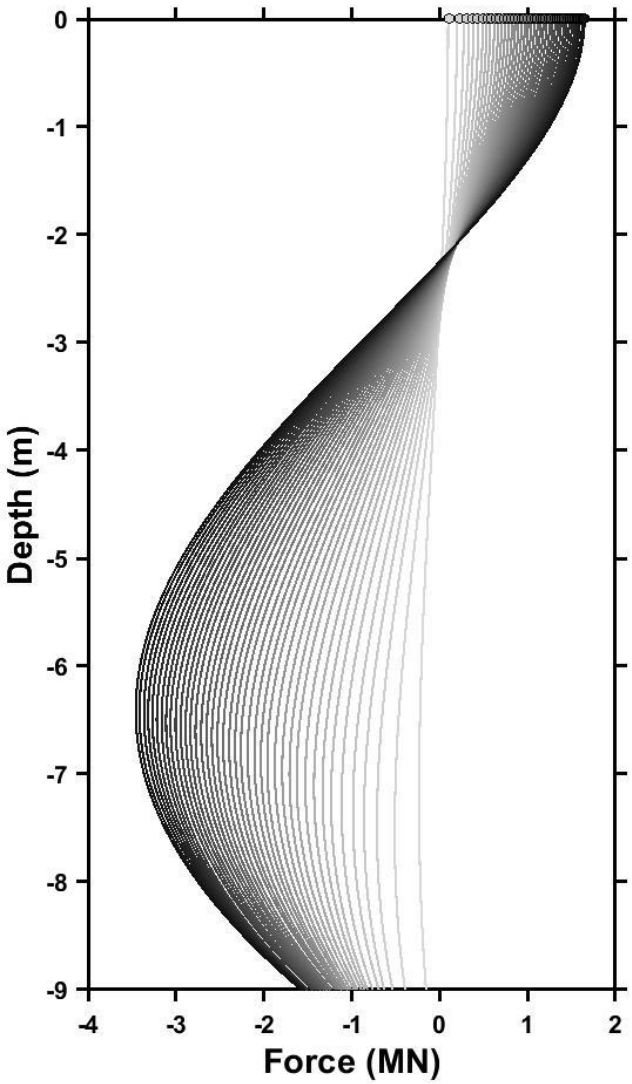

Figure 68: Shear force profiles for PLT 32

4.1.3 Soil resistance profiles

Ultimately, double differentiation of the bending moment profiles generates the soil resistance curves shown in Figure 69. The resistance profiles noticeably differ from the kind that is shown in Figure 7 and Figure 10 for a flexible pile. The resistance decreases to zero around a depth of around 6.7m, which is equal to 0.75 times the embedded length of the pile.

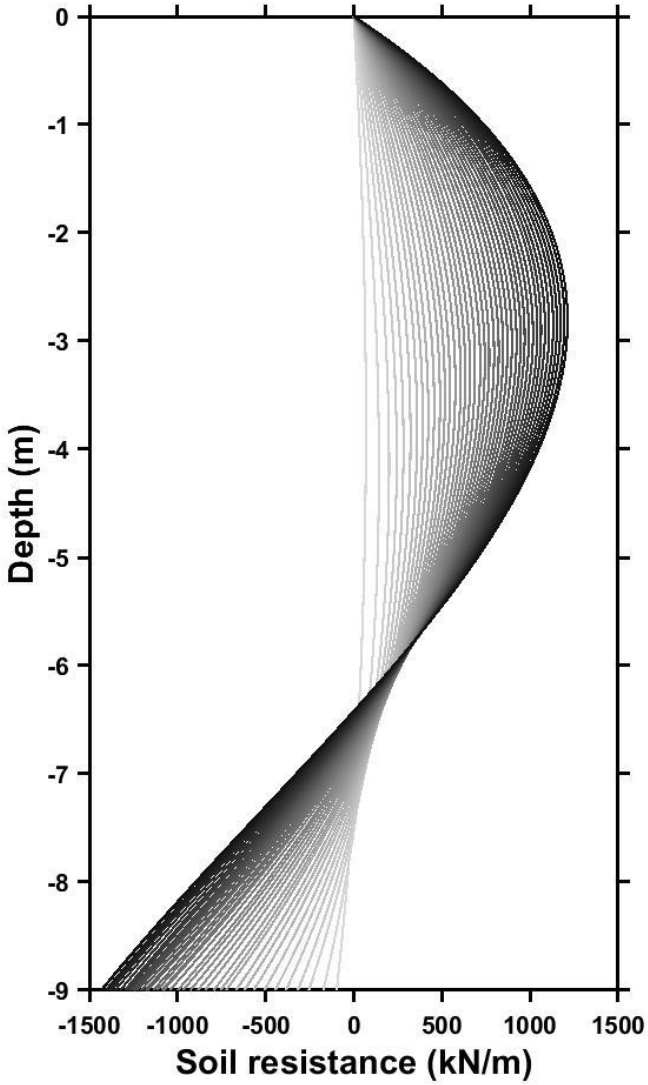

Figure 69: Soil resistance profiles for PLT 32

4.1.4 Deflection profiles

Integrating the bending moment profiles twice produces the deflection profiles of the pile throughout its displacement range. As Figure 70 shows, the deflection curves seem to fit the measurement data from the LVDT's (located at heights of 0.045 and 0.085m) reasonably well. Additionally, the deflection curves show a mechanism of nearly completely rigid rotation, with a centre of rotation a depth of around 0.75 times the embedded length. This matches the conceptual behaviour assumed in the rotational spring method as outlined in Section 1.2.5.

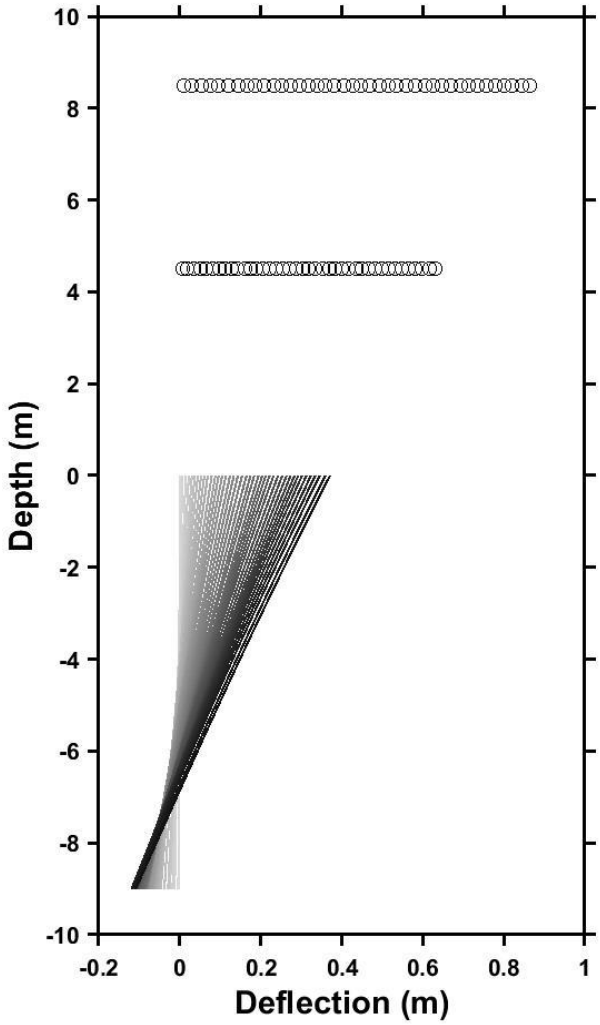

Figure 70: Deflection profiles for PLT 32

4.1.5 *p-y* curves

Individual p-y curves from the profiles shown in Section 4.1.3 can be plotted. Combining these with predictions from the *CPT*-based *p-y* methods at various depths produces the plots shown in Figure 71a through h.

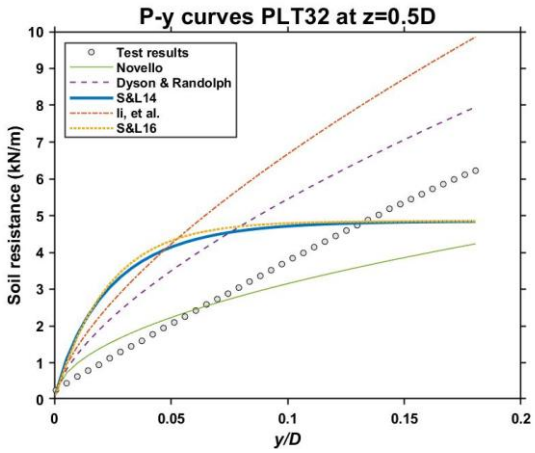

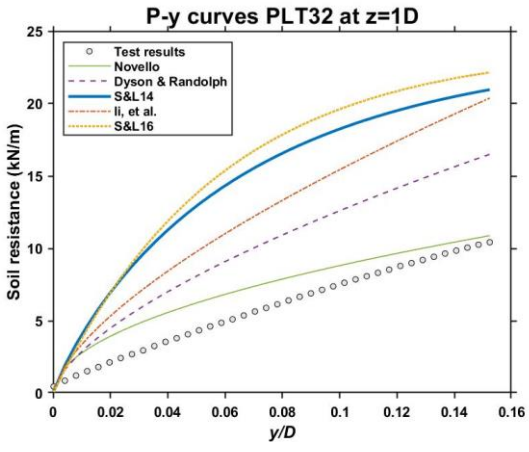

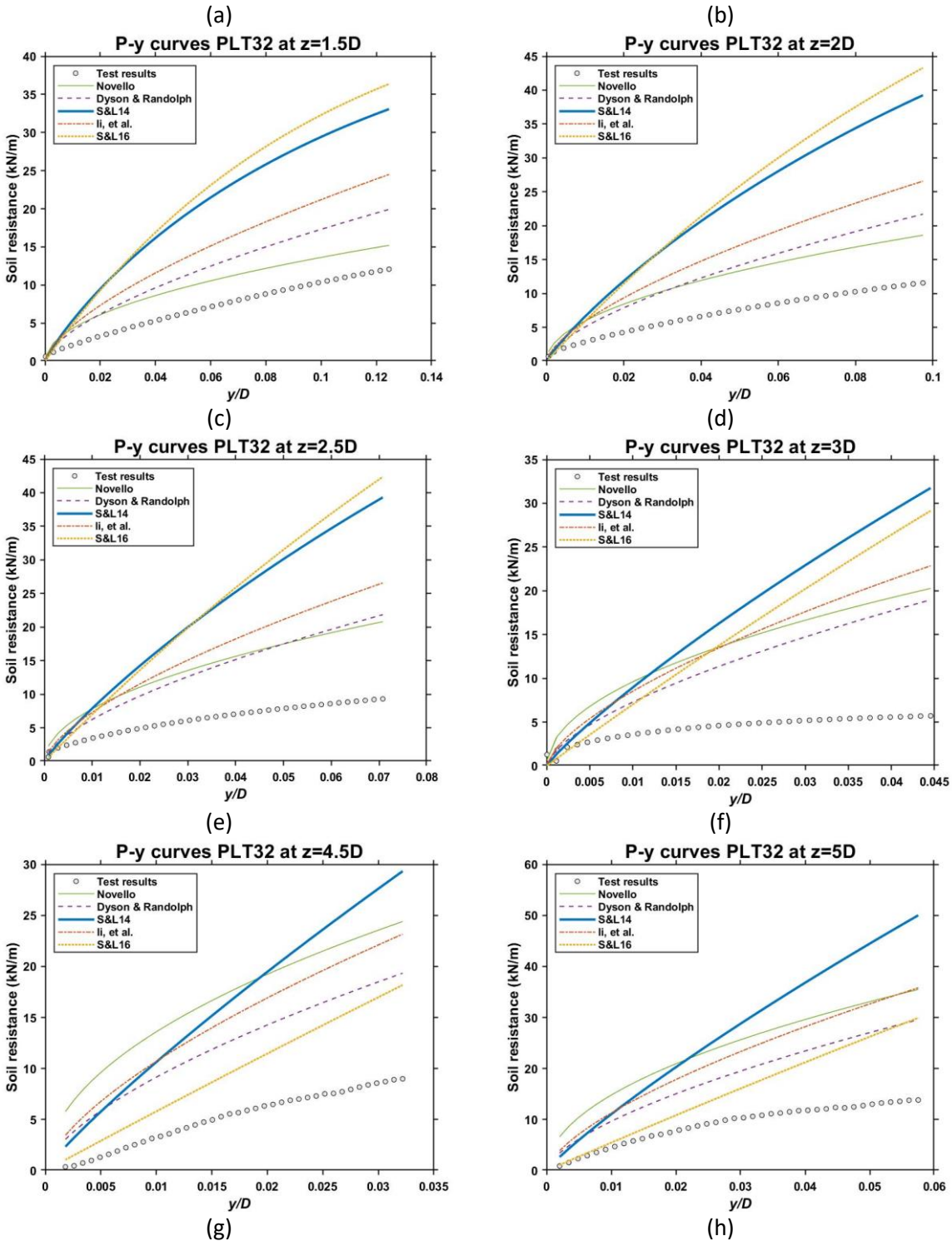

Figure 71: P-y curves at depths of 0.5-5D for PLT 32

From these *p-y* curves a number of things can be observed. Firstly at a very shallow depth of 0.5*D* the ultimate resistance of the methods by Suryasentana & Lehane (2014) and Suryasentana & Lehane (2016) is reached (though it is not congruent with the measured resistance). Beyond this depth the ultimate resistance is not reached and is therefore likely strongly overestimated. This is in accordance with the findings from chapter 2, where it was found that both methods from Suryasentana & Lehane consistently predict increasing loads at large displacements even though a maximum load is reached in the measurements.

Furthermore, all *p-y* methods tend to overestimate the soil resistance by a factor of 2-3 along the entire profile except for their predictions at very shallow depths. The methods from Dyson & Randolph (2001) and Novello (1999) do this the least overall. By contrast however, as Figure 72 shows, the

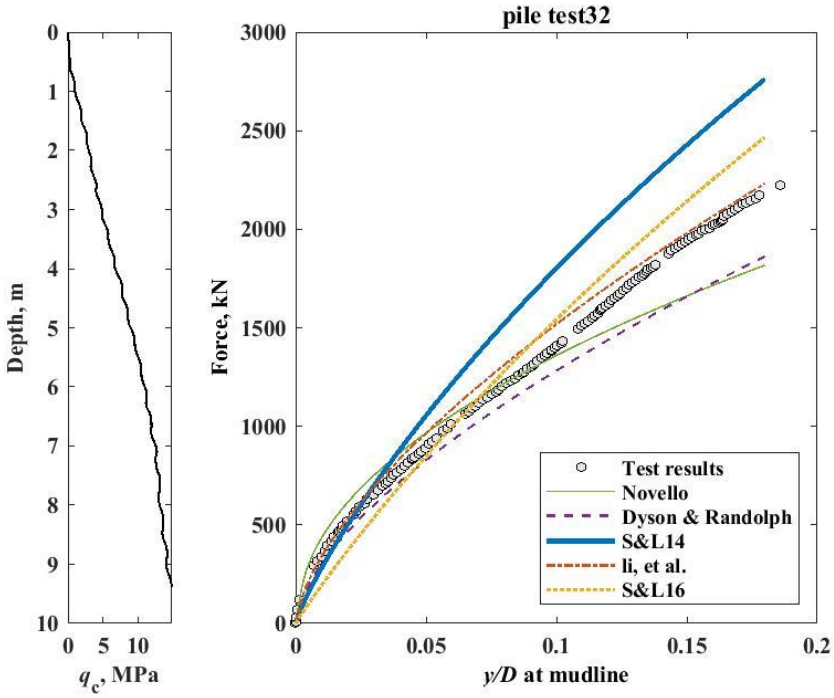

Figure 72: H-y measurements and predictions for PLT 32

resulting *H-y* predictions are much more accurate. Additionally, it is shown in Section 2.3.3 that on average all methods except that from Dyson & Randolph (2001) are unconservative when predicting load-displacement behaviour at a displacement of D/10 (meaning that they overestimate the developed load at a given displacement), though decidedly less so than for these *p-y* curves. This apparent contradiction can likely be explained by the assumption that the overestimations of the soil resistance forces developed above- and below the centre of rotation largely cancel each other out. This is possible because even though a greater part of the embedded length (around 0.75L) is located above the rotational centre, the vertical effective stresses and therefore soil resistances are greater below the centre of rotation (as can be seen in Figure 669 from Section 4.1.3).

4.3 Unification of rigid pile response through normalization

A different approach from the *p-y* method to the modelling of the laterally loaded rigid pile in sand is presented by Wang, et al. (2022) and makes use of the simplified pile-soil interaction illustrated in Figure 73. In this model the pile experiences a horizontal load (*H*) and consequently rotates around a single point located at depth (*d*). The lateral soil pressure (*P*) is defined according to the effective stress and a net pressure coefficient (*K*). This simplified interaction model can help to normalize the response of piles of different diameters.

Additionally, Richards et al. (2021) showed that the stress dependency of the stiffness of the load-deflection response of a short pile under lateral monotonic loading can be successfully captured by the normalization method proposed by Leblanc, et al. (2010). Here the load (*H*) and the groundline

displacement (y_0/D) are respectively normalized by $DL^2\gamma'$ and $(p_a/L\gamma')^\eta$, where η is related to the shear modulus and is generally taken at 0.5.

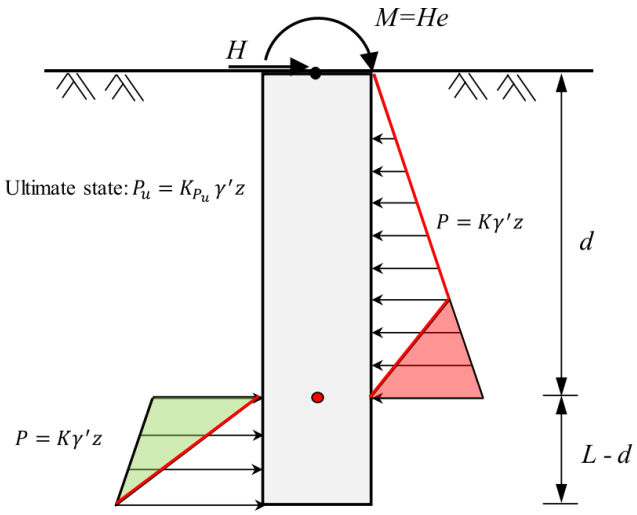

Figure 73: Simplified pile-soil interaction model from Wang, et al. (2022)

4.2.1 Load-rotation response

Figure 74 shows the results from all the centrifuge load tests from table, with the applied load plotted against the groundline rotation, which is normalized similarly to the normalization of displacement as per Leblanc, et al. (2010) to account for varying stress levels. As can be expected, Figure 74 shows varying loads for a given amount of rotation depending on the prototype pile dimensions (influenced both by model pile dimensions and centrifuge acceleration). Additionally it shows very similar results for piles of equal prototype dimensions, indicating consistency of the pile load tests.

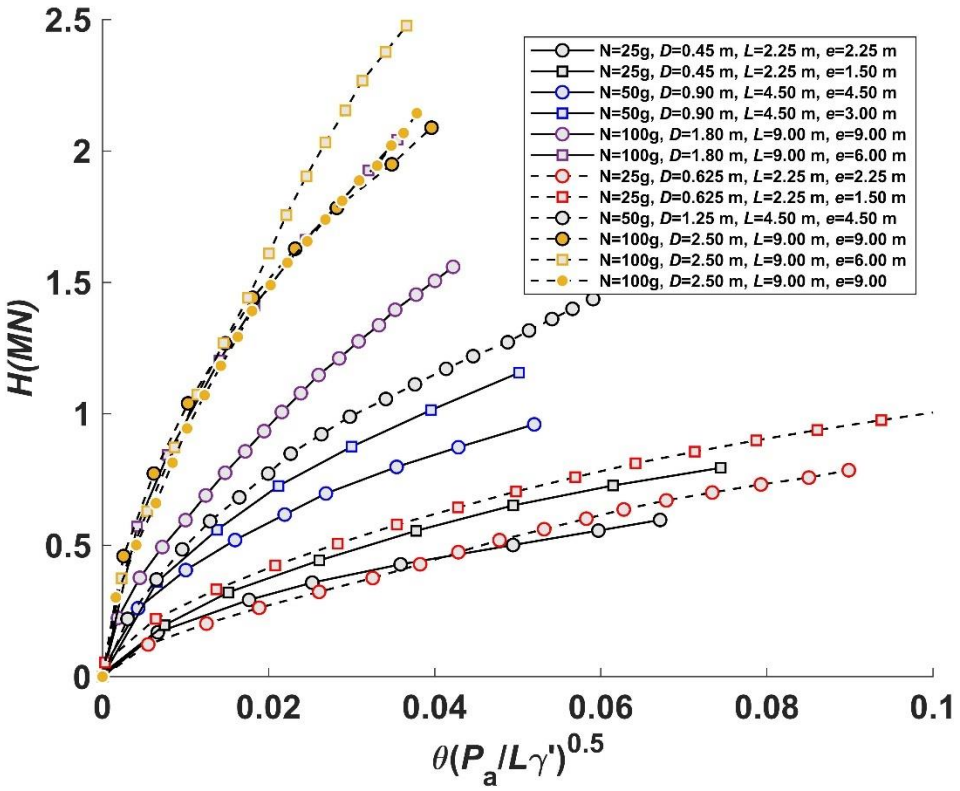

Figure 74: Load-rotation curves for all centrifuge PLT's performed for this study

4.2.2 Effect diameter on rigid pile response

Numerical investigations by Wang, et al. (2022) confirmed that the load-rotation response at the mudline for rigid piles with varying diameters in homogeneous sands can be unified by normalizing H by $DL^2\gamma'$ and that similarly the moment-rotation response can be unified by normalizing M by $DL^3\gamma'$. This normalization is in agreement with that from Leblanc, et al. (2010) and should account for both varying pile diameter and stress level. The same type of normalization is applied to the results of three centrifuge tests from this study which were performed on a sand of 80% relative density and piles with an embedded length and eccentricity of 9m at prototype scale, the product of which is shown in Figure 75. The three Moment-rotation curves are indeed unified after this normalization. This supports the notion that for a rigidly rotating laterally loaded pile in a uniform sand, the aforementioned normalized load transfer response is independent of pile diameter.

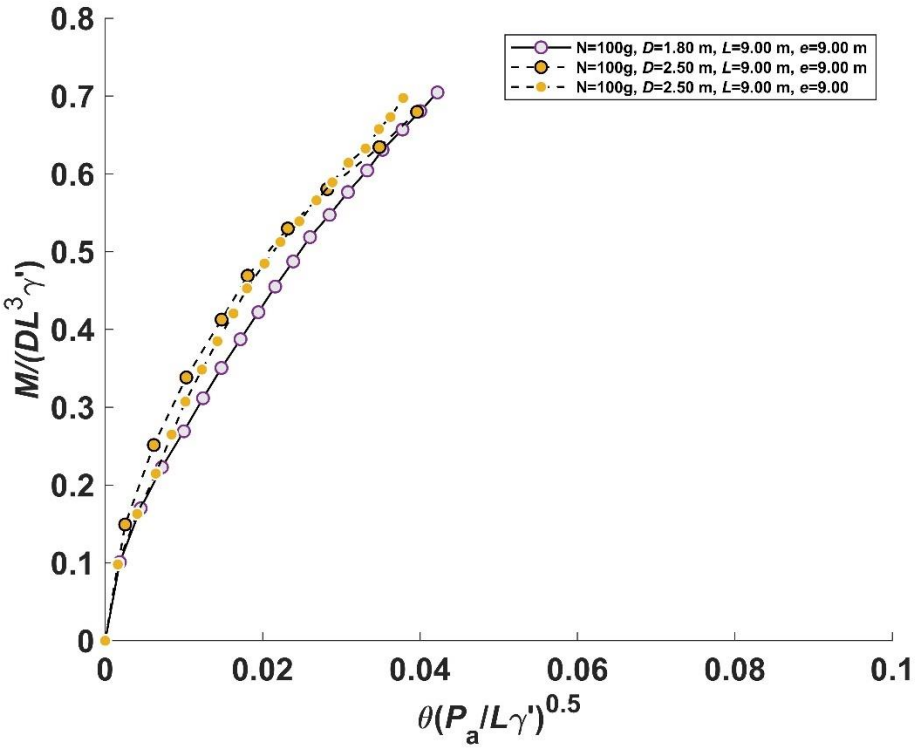

Figure 75: Unified moment-rotation curves for piles of 9m length in sand of 80% Dr, with moment at the mudline

4.2.3 Effect loading eccentricity on rigid pile response

Wang, et al. (2022) showed that for a rigid pile under lateral load, changing forces and moments at varying eccentricities (*e*) are the result of a changing loading arm relative to the rotation centre. Assuming the latter is located at a depth of 0.75*L*, this means that the response of a rigid pile under lateral load can be unified by defining the results as a moment relative to the rotation centre, as shown in Equation 49.

$$M_r = H(e + 0.75L) \tag{49}$$

By normalizing this moment by ($DL^3\gamma'$), the response of piles of varying dimensions loaded at varying eccentricities were unified. After applying this type of normalization to all of the centrifuge load test results from this study, the curves in Figure 766 are produced. This figure shows that the previously varying load transfer curves have now indeed collapsed into a narrow band, suggesting that for these empirical pile load tests a normalized moment-rotation response can be defined that captures the effects of pile diameter, stress level and loading eccentricity. However, the curves are not completely unified, as would theoretically be expected according to the simplified pile-soil interaction model.

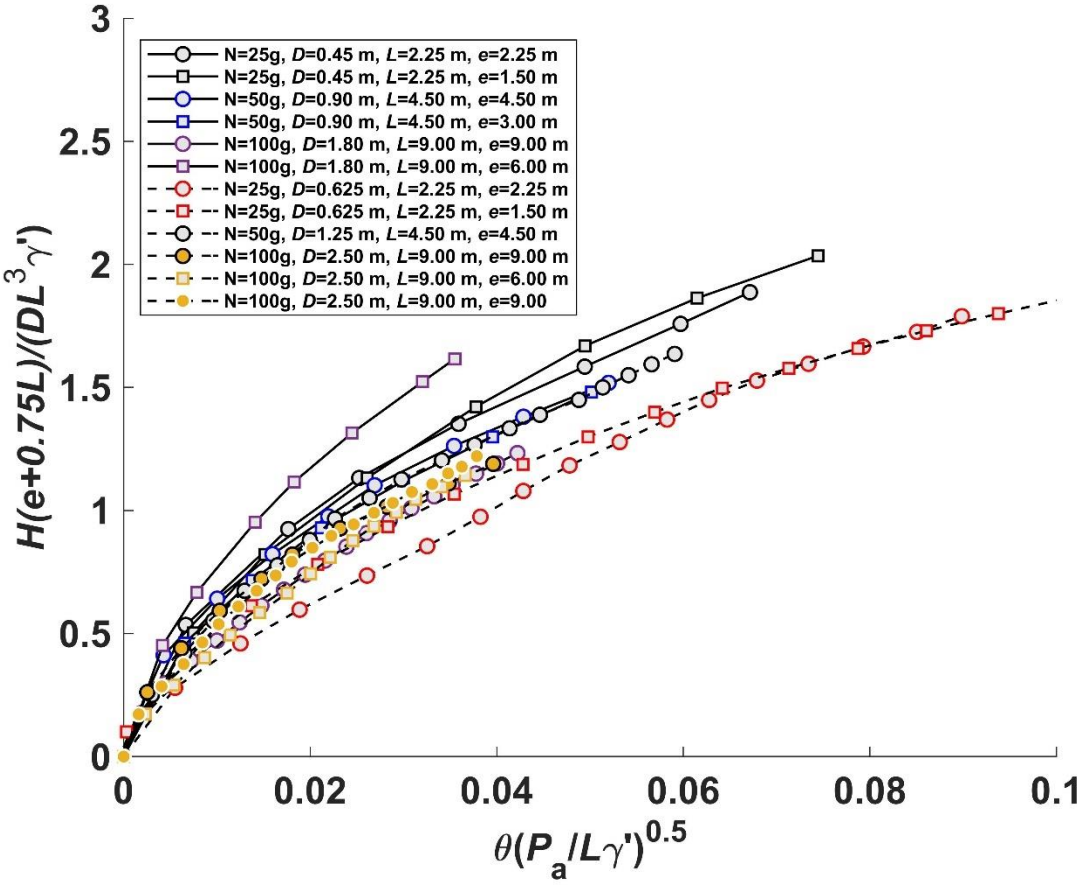

Figure 766: Normalized Moment-rotation curves for all centrifuge PLT's performed for this study

There are several possible explanations as to why this is not the case. One thing that has been shown before by Wang (2022) is that the depth of the rotational centre of a rigid laterally loaded pile decreases slightly with an increasing loading eccentricity (see Figure 777). This leads to a slightly lower normalized pile moment capacity at large loading eccentricities

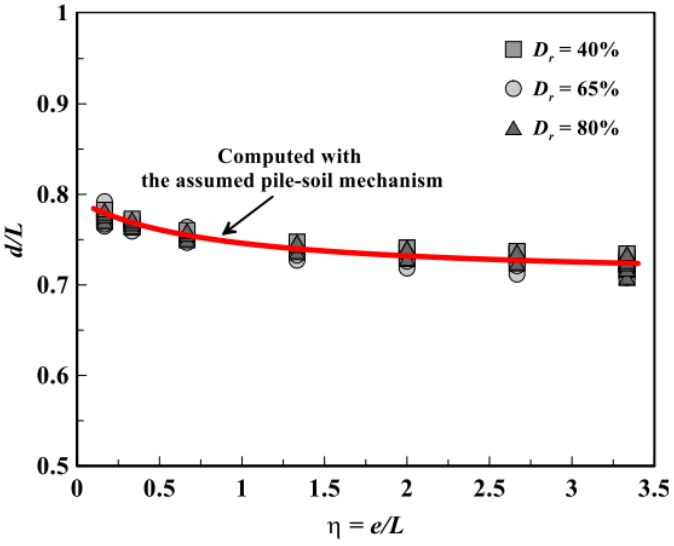

Figure 777: Depth of rotational centre d as a function of loading eccentricity e from Wang (2022)

Furthermore, Wang, et al. (2022) also showed a slight reduction in normalized moment for a given rotation with increasing pile length, especially at higher capacity mobilization (see Figure 78). This is thought to be because of decreasing dilatancy at higher stress levels which occur for longer piles, leading to a lower normalized pile moment capacity. This makes sense, given that the normalization method of Leblanc, et al. (2010) does not consider dilatancy. Nevertheless this does not offer a satisfying explanation in this instance, since the tests on piles with a diameter of 2.5m and a length of 9.0m show a higher normalized moment than the tests on piles with a diameter of 0.625m and a length of 2.25m.

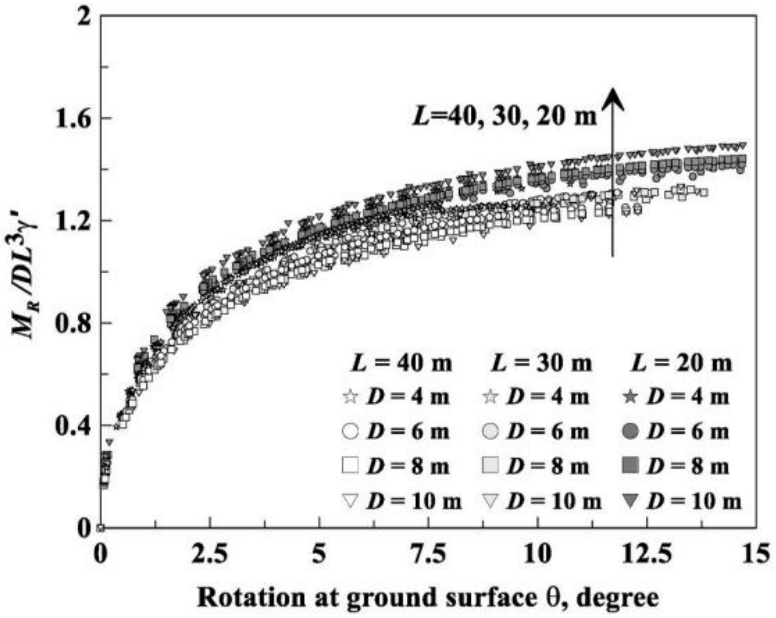

Figure 788: Inreasing moment capacity with increasing pile length from Wang (2022)

Likely explanations for the differences in normalized rotational moment capacity are significant non-uniformity of the model sand with respect to relative density, variation in overall sand relative density between samples, changes in relative density due to pile installation or a combination of these related factors. As can be seen in Figure 79, Wang (2022) found that a doubling of the sand relative density from 40% to 80% leads to a near doubling of the ultimate moment capacity.

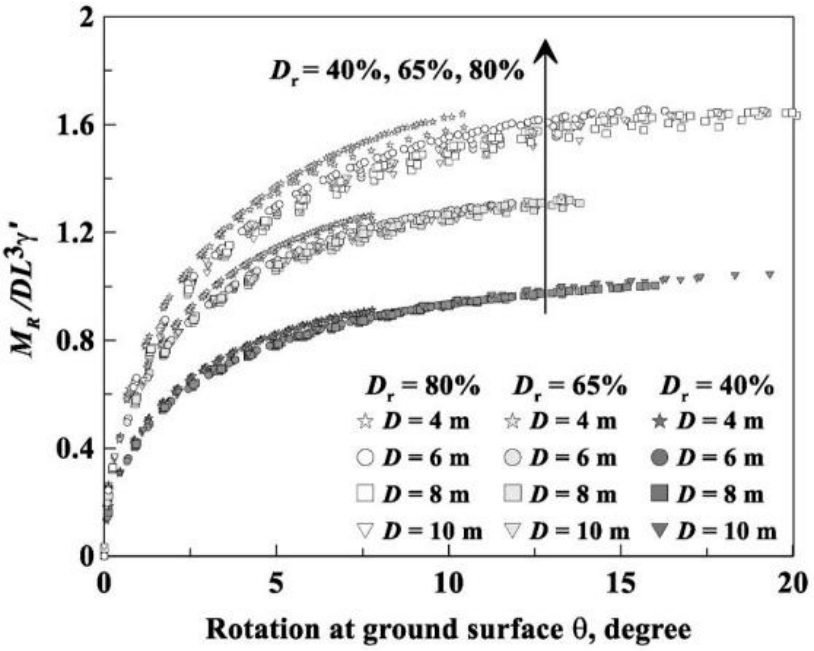

Figure 79: Increasing moment capacity with increasing sand relative density Dr from Wang (2022)

Additionally, as is shown in Figure 54 and Figure 55 from Section 3.3.3, there is significant non-uniformity present in the sand samples used in the centrifuge load tests from this study (local variations of up to around 10% D_r). Furthermore, although the tests shown in Figure 766 were all performed in sands of around 80% D_r, in reality the true density will have varied by up to several percentage points between tests. Looking at the findings shown in Figure 79, this has likely produced a significant variation in normalized pile moment capacity. Considering the differences between lab testing and FEA (where a sand can be perfectly homogenous and of exactly equal density between tests) this is to be expected to a degree.

Finally, the experimental load tests presented here differ from the numerical analyses performed by Wang, et al. (2022) because the model piles, though quite stiff, are not perfectly rigid (as was assumed in the numerical calculations). This could also provide an explanation for the imperfect unification of the moment-rotation response.

Part 5. Conclusions and future work

5.1 Conclusions & discussion

Given the current trends in monopile foundation construction and design the aim of this study is to evaluate the performance- and find ways of developing design methods for the laterally loaded pile in sand and short and rigid piles in particular under monotonic loading.. This is done by collecting and re-analysing experimental load-deflection results from existing literature and also performing additional centrifuge pile load tests in the TU Delft lab to obtain data from which *p-y* curves are derived. All the tests are performed under a fully drained monotonic loading condition. Additionally in the course of these lab tests, the experimental methods used are evaluated and improved upon. The measured load-deflection response and computed response at ground level are compared to qualitatively and quantitatively assess the performance of the different *CPT*-based *p-y* models in Part 2 and 4. Furthermore, the applied experimental methods are outlined and evaluated in Part 3. Finally the predicted *p-y* curves are produced and evaluated against the gathered experimental test data and the moment-rotation responses of the lab tests are unified through normalization in Part 4. Below, the main conclusions for each part of the study are presented and discussed.

Part 2:

- The load tests gathered in the database are fairly representative for monopile foundations built offshore in Europe with regard to aspect ratio and for 31 out of 38 tests the ULS is reached.
- All *CPT*-based *p-y* methods fail to properly capture weak behaviour at large displacements. This likely means that even Suryasentana & Lehane (2014;2016) don't accurately model ultimate soil pressures.
- All methods except that from Suryasentana & Lehane 2014 are less accurate at small- than at large displacements.
- All methods are on average conservative at a displacement of D/100
- All methods are either neutral or unconservative at a displacement of D/10. This is potentially due to the absence- or overestimation of the ultimate soil pressure.
- Overall Dyson and Randolph (2001) and Li, et al. (2014) generate the most accurate predictions and Suryasentana & Lehane (2014;2016) generate the least accurate ones, even though the latter two have more advanced features.
- All methods generate relatively inaccurate predictions in general when compared to a benchmark from Burd, et al. (2019).
- All methods except Novello (2001) are more accurate for long and flexible piles at small displacements.
- Suryasentana & Lehane (2014) and Li, et al. (2014) are more accurate for short and rigid piles at large displacements, though this trend is less clear.

The results regarding the relationship between the accuracy of load-deflection predictions generated using the *CPT*-based *p-y* models and pile aspect ratio and rigidity are not as conclusive as the others, because the type of trend that is evaluated for these correlations is somewhat arbitrary. Nevertheless, in the stated cases significant trends do seem to be present.

Part 3:

- Processed CT scans and results from several centrifuge *CPT* tests are used to show that both sample preparation methods produce samples of acceptable uniformity with sufficiently consistent mean D_r

- Overall hand raining (method B) is preferred for sample preparation since it requires less equipment, is less time-consuming and produces samples with less overall variance in D_r.

It should be noted that due to uneven vibration the sand in the top half of samples (which contain the model piles) produced using the hand raining method is substantially more dense than the bottom half. This is acceptable for the purposes of this study since it is reflected in the *CPT*-profiles that serve as input for the *p-y* models and since this study only concerns dense sands. It could however be a problem for tests in samples of intermediate density or for deeper embedded piles.

A second potential weakness of the experimental results presented in this study is that problems with the vertical actuator in the centrifuge setup limited the range of stress levels and soil conditions for which CPT data could be obtained and they furthermore necessitated the use of a single *CPT*-profile for multiple load tests at the same acceleration level. This is ultimately deemed acceptable because *CPT*-results are shown to be consistent between tests and because the soil conditions with sand of 80% relative density are fairly representative of offshore conditions in the North Sea.

Finally, the model pile installation method of pushing at 1g is not representative for real-world conditions and can cause disturbance of the soil surrounding the pile, in this case decreasing the D_r. However, a processed CT scan is presented to show that this disturbance is limited.

Part 4:

- The conclusion from previous research (Choo & Kim 2015) that the initial response predicted by API is consistently far too stiff is supported by the lab test data. This means that the API model is likely unconservative in the prediction of the limit states and that it is therefore unsafe.
- The change in stiffness of the pile response with increasing displacement predicted by *CPT*-based *p-y* models is usually too gradual, whereas that predicted by API is usually to sudden.
- A 5^{th} order polynomial curve fitting method is applied to the bending moment data and is subsequently found to produce reasonable soil resistance profiles
- The ultimate resistance incorporated in the models from Suryasentana & Lehane (2014;2016) is only reached at very shallow depths and even then it does not closely match the measured p_u, which is in agreement with the findings from Part 2.
- At all except the shallowest depths, all *CPT*-based models overestimate the soil resistance by a factor of 2-3. Dyson & Randolph (2001) and Novello (1999) overestimate *p* the least. However, the resulting prediction of the load-deflection response is much more reasonable

An important caveat to the conclusions regarding the *p-y* predictions of the various models is that due to difficulties with the gathering of quality bending moment data, only *p-y* curves for one pile load test could be calculated. Ideally, *p-y* curves for a greater variety of load tests would be analysed.

- A normalization method by Leblanc, et al. (2010) which incorporates stress dependency of stiffness is used on the empirical test results presented in this study to show that for a laterally loaded, rigidly rotating pile the normalized load transfer response is independent of pile diameter.
- The normalization method by Leblanc, et al. (2010) is combined with a simplified pile-soil interaction model for a rigidly rotating pile by Wang, et al. (2022) to show that relative to

the rotation centre (located at a depth of 0.75*L*) a normalized moment-rotation response can be defined that is independent of pile diameter, stress level and loading eccentricity.

Several explanations are suggested for the fact that the normalized moment-rotation curves are not entirely unified. Results from Wang, et al. (2022) show a decrease in moment with increasing pile length that is likely due to decreased dilatancy at higher stress levels (which is not incorporated in the normalization method by Leblanc et al.). However, this explanation does not fit the data well and instead the most likely cause is either imperfect uniformity of the sand samples and slight variations in mean relative density between them, or imperfect rigidity of the model pile.

Ultimately it can be concluded that the evaluated *CPT*-based *p-y* models potentially offer a promising and practical method of modelling laterally loaded piles in sand and that they provide better predictions for short and rigid piles than the API method. However, they are likely not accurate and consistent enough to provide useable predictions for the application of a monopile foundation in sand under lateral load. In that light, the following section will suggest a number of ways in which these can be improved. Furthermore, the successful unification of the rigid pile response from the lab test data is in agreement with previous numerical research (Wang, 2022) and supports the viability of a rotational spring model for predicting the response of monopile foundations under lateral load.

5.2 Recommendations for future work

A number of future investigations can be identified on the basis of the previously presented results that would expand upon the research presented in this study and that could lead to improvements in either the employed experimental research methods or the discussed design methods for the laterally loaded pile in sand. These investigations include:

- Improving the ultimate soil resistance as defined in the models from Suryasentana & Lehane (2014;2016).

It is shown for both the predicted load-deflection- and *p-y* response that the ultimate resistance is usually not reached when measurement data suggest that it should be. The (numerical) pile load test datasets from which these models were derived do contain a range of soil conditions and pile characteristics. However, the ultimate resistance can likely be improved by better calibration of the *p-y* curves at greater depths, possibly using experimental testing data.

- Improving the predicted change in stiffness with increasing displacement

It is clear that the change in stiffness predicted by the CPT-based p-y models is too gradual. This could potentially be improved by developing new models that are based on a different backbone function. A backbone function with more empirical fitting parameters could provide more control over the shape of the *p-y* curves. An example could be the four-parameter conic function employed by the PISA model presented by Byrne, et al. (2017)

- Systematically evaluating the predicted *p-y* curves of the discussed models for a more complete set of pile load tests.

The analysis from Section 4.2 can be expanded and its conclusions be made better supported by collecting more high-quality bending moment- and CPT data from either field tests or centrifuge tests.

- Performing further image analysis on the CT scans of the sand samples after model pile installation to quantify the change in relative density due to soil disturbance during pile installation at 1g as a function of the radial distance from the pile.
- Identify- and potentially incorporate the effect of varying pile rigidity on the moment-rotation response of a laterally loaded rigid pile.

References

Allersma, H. G. B. (1994). Development of miniature equipment for a small geotechnical centrifuge. *Transportation research record*, *1432*, 99.

Amar Bouzid, D. (2018). Numerical investigation of large-diameter monopiles in sands: Critical review and evaluation of both API and newly proposed py curves. *International Journal of Geomechanics*, *18*(11), 04018141.

API, 2011. Geotechnical and foundation design considerations, ANSI/API RP 2GEO. In: Washington, DC: API Publishing Services..

Arany, L., Bhattacharya, S., Macdonald, J. & Hogan, S. J., 2014. *Simplified critical mudline bending moment spectra of offshore wind turbine support structures.* Bristol, UK, John Wiley & Sons.

Ardalan, H., Eslami, A. & Nariman-Zahed, N., 2009. Piles shaft capacity from CPT and CPTu data by polynomial neural networks and genetic algorithms. Comput. Geotech., 2009, 36, 616– 625.

Baguelin, F., Frank, R. & Said, Y. H., 1977. Theoretical Study of Lateral Reaction Mechanism. Geotechnique, Volume Vol. 27, No. 3, pp. 405-434.

Bjerrum, L. (1973). Geotechnical problems involved in foundations of structures in the North Sea. *Geotechnique*, *23*(3), 319-358.

Broms, B., 1964. Lateral Resistance of Piles in Cohesionless Soils. Journal of the Soil Mechanics and Foundations Division, Proceedings of the ASCE , Volume 90, No.SM3, 123- 156.

Burd, H. J., Beuckelaers, W. J., Byrne, B. W., Gavin, K. G., Houlsby, G. T., Igoe, D. J., ... & Zdravković, L. (2020). New data analysis methods for instrumented medium-scale monopile field tests. *Géotechnique*, *70*(11), 961-969.

Burd, H. J., Beuckelaers, W. J., Byrne, B. W., Gavin, K. G., Houlsby, G. T., Igoe, D. J., ... & Zdravković, L. (2020). New data analysis methods for instrumented medium-scale monopile field tests. *Géotechnique*, *70*(11), 961-969.

Burd, H. J., Taborda, D. M., Zdravković, L., Abadie, C. N., Byrne, B. W., Houlsby, G. T., ... & Potts, D. M. (2020). PISA design model for monopiles for offshore wind turbines: application to a marine sand. *Géotechnique*, *70*(11), 1048-1066.

Byrne, B. et al., 2015b. Field testing of large diameter piles under lateral loading for offshore wind applications. *Proc 15th European Conf on Soil*..

Byrne, B. W., & Houlsby, G. T. (2004). Foundations for offshore wind turbines. *Philosophical Transactions of the Royal Society of London. Series A: Mathematical, Physical and Engineering Sciences*, *361*(1813), 2909-2930.

Byrne, B. W., McAdam, R. A., Burd, H. J., Houlsby, G. T., Martin, C. M., Beuckelaers, W. J. A. P., ... & Plummer, M. A. L. (2017, January). PISA: new design methods for offshore wind turbine monopiles. In *Offshore Site Investigation Geotechnics 8th International Conference Proceeding* (Vol. 142, No. 161, pp. 142-161). Society for Underwater Technology.

Byrne, B., McAdam, R., Burd, H., Houlsby, G., Martin, C., Zdravkovic, L., Taborda, D., Potts, D., Jardine, R., Sideri, M., (2015a). *New design methods for large diameter piles under lateral loading for offshore wind applications*, 3rd International Symposium on Frontiers in Offshore Geotechnics (ISFOG 2015), Oslo, Norway, June, pp. 10-12.

Choo, Y. W., & Kim, D. (2016). Experimental development of the p-y relationship for large-diameter offshore monopiles in sands: Centrifuge tests. *Journal of Geotechnical and Geoenvironmental Engineering*, *142*(1), 04015058.

Cox, W. R., Reese, L. C., & Grubbs, B. R. (1974, May). Field testing of laterally loaded piles in sand. In *Offshore Technology Conference*. OnePetro.

Davidson, H. L. & Donovan, T. D., 1983. DESIGN OF LATERALLY LOADED DRILLED PIERS. *IEEE Transactions on Power Apparatus and Systems*, Volume PAS-102, No. 1.

DNV-OS-J101, 2014. *Design of Offshore Wind Turbine Structures*, s.l.: DET NORSKE VERITAS AS.

Doherty, P., Li, W., Gavin, K., & Casey, B. (2012, September). Field lateral load test on monopile in dense sand. In *Offshore Site Investigation and Geotechnics: Integrated Technologies-Present and Future*. OnePetro.

Dyson, G. J. & Randolph, M. F., 2001. Monotonic lateral loading of piles in calcareous sand. J. Geotech. Geoenviron. Engng, 127(4), p. 346–352.

EUR-Lex - 52020DC0562 - EN - EUR-Lex. (n.d.). Retrieved September 16, 2022, from https://eur-lex.europa.eu/legal-content/EN/TXT/?uri=CELEX:52020DC0562

Foursoff. (2018). *Investigation into a new CPT-based design method for large diameter monopiles in sand.* Delft: TU Delft.

Haiderali, A. E., & Madabhushi, G. (2016). Evaluation of curve fitting techniques in deriving p–y curves for laterally loaded piles. *Geotechnical and Geological Engineering*, *34*(5), 1453-1473.

Houlsby , G. T. & Hitchman, . R., 1988. Calibration chamber tests of a cone penetrometer in sand. Géotechnique, 38(1), pp. 39-44.

Jamiolkowski, M., Lo Presti, D. C. F., & Manassero, M. (2003). Evaluation of relative density and shear strength of sands from CPT and DMT. *Soil behavior and soft ground construction*, *7*(119), 201-238.

Janoyan, K., & Whelan, M. (2004*). Interface between soil and large diameter piles. In A. Geotechnical, Drilled shafts, micropiling, deep mixing remedial methods and special foundation systems.* ASCE.

Kirkwood, P. B. (2016). *Cyclic lateral loading of monopile foundations in sand* (Doctoral dissertation, University of Cambridge).

Klinkvort, R. T., & Hededal, O. (2013). *Lateral response of monopile supporting an offshore wind turbine*. Proceedings of the Institution of Civil Engineers-Geotechnical Engineering, 166(2), 147-158.

Klinkvort, R.T. (2012). *Centrifuge modelling of drained lateral pile - soil response: Application for offshore wind turbine support structures*, PhD Thesis, Technical University of Denmark.

LAP. (n.d.). Retrieved September 16, 2022, from https://lap.geocalcs.com/Login.aspx

LeBlanc, C., Houlsby, G. T. and Byrne, B. W. (2010). Response of stiff piles in sand to long-term cyclic lateral loading. Géotechnique, 60(2), 79-90.

Lehnhoff, S., Gómez González, A., & Seume, J. R. (2020). Full-scale deformation measurements of a wind turbine rotor in comparison with aeroelastic simulations. *Wind Energy Science*, *5*(4), 1411-1423.

Lemnitzer, A., 2013. *www.findapile.com*. [Online] from: http://www.findapile.com/p-y-curves/definition

Li, W., Igoe, D. & K., G., 2014. Evaluation of CPT-based P–y models for laterally loaded piles in siliceous sand. Géotechnique Letters, Issue 4, p. 110–117.

Lunne, T., Robertson, P. & Powell, J., 1997. *Cone Penetration Testing in Geotechnical Practice*. New York, Blackie Academic/Routledge Publishing.

Madabhushi, G. (2017). *Centrifuge modelling for civil engineers*. CRC Press.

McAdam, R. A., Byrne, B. W., Houlsby, G. T., Beuckelaers, W. J. A. P., Burd, H. J., Gavin, K., ... & Zdravković, L. (2019). Monotonic lateral loaded pile testing in a dense marine sand at Dunkirk, Géotechnique. *online ahead of print*.

McClelland, B. & Focht, J. A., 1958. *Soil Modulus for Laterally Loaded Piles*.. ASCE, No. 2954, 1049-1063.

Muir Wood, D. (2004). *Geotechnical Modeling*. Version 2.2.

Murphy, G., Doherty, P., Cadogan, D., & Gavin, K. (2016). Field experiments on instrumented winged monopiles. *Proceedings of the Institution of Civil Engineers-Geotechnical Engineering*, *169*(3), 227-239.

Novello, E., 1999. From static to cyclic P–y data in calcareous. Perth, Proc. 2nd Int. Conf. on Engineering for Calcareous, p. 17–27.

Negro, V., López-Gutiérrez, J. S., Esteban, M. D., Alberdi, P., Imaz, M., & Serraclara, J. M. (2017). Monopiles in offshore wind: Preliminary estimate of main dimensions. *Ocean Engineering*, *133*, 253-261.

Nunez, I. L., P. J. Hoadley, M. F. Randolph, and J. M. Hulett (1988). *Driving and tension loading of piles in sand on a centrifuge*. In Centrifuge 88.

Padmanathan, K., Kamalakannan, N., Sanjeevikumar, P., Blaabjerg, F., Holm-Nielsen, J. B., Uma, G., ... & Baskaran, J. (2019). Conceptual framework of antecedents to trends on permanent magnet synchronous generators for wind energy conversion systems. *Energies*, *12*(13), 2616.

Peralta, P., 2010. *Investigations on the Behavior of Large Diameter Piles under Long-Term Lateral Cyclic Loading in Cohesionless Soil*, Hannover: Institut für Geomechanik (IGtH) Leibniz Universität Hannover.

Petrasovits, G. and Award, A. (1972). Ultimate lateral resistance of a rigid pile in cohesionless soil. Proc., 5th European Conf. on SMFE 3, The Spanish Society for Soil Mechanics and Foundation, 407–412.

Poulos, H. G. & Hull, T. (1989). *The role of analytical geomechanics in foundation engineering*. In Foundation engineering: current principles and practices (ed. F. H. Kulhawy), GSP No. 22, pp. 1578–1606. New York, NY, USA: ASCE.

Prendergast, L. J., & Gavin, K. (2016). Monitoring of Scour Critical Bridges using Changes in the Natural Frequency of Vibration of Foundation Piles: A Preliminary Investigation. *Materials and Infrastructures 1*, *5*, 199-209.

Remaud, D. (1999). *Pieux sous charges latérales: étude expérimentale de l'effet de groupe*. THESE DE DOCTORAT, DISCIPLINE: SCIENCES DE L'INGENIEUR, SPECIALITE: GENIE CIVIL.

Richards, I., Bransby, F., Byrne, B., Gaudin, C., & Houlsby, G. (2021). The effect of stress-level on the response of a model monopile to cyclic lateral loading in sand. *Journal of Geotechnical and Geoenvironmental Engineering-ASCE*, *147*(3).

Robertson, P. K. (2009). Interpretation of cone penetration tests—a unified approach. *Canadian geotechnical journal*, *46*(11), 1337-1355.

Rohatgi, A., 2021. *www.automeris.io*. [Online] from: https://automeris.io/WebPlotDigitizer

Rose C et al. 1996. *Cone Penetrometer. Innovative Technology Summary Report*, DOE/EM-0309. US Department of Energy: Washington, DC.

Salgado, R. & Randolph, M. F. (2001). Analysis of cavity expan-sion in sand.Int. J. Geomech.1, No. 2, 175–192.

Schmertmann, J. H. (1976). An updated correlation between relative density DR and Fugro-Type electric cone bearing, qc. *Contract report DACW*, *39*.

Suryasentana, S. & Lehane, B., 2016. Updated CPT-based p–y formulation for laterally loaded piles in cohesionless soil under static loading. Géotechnique 66, No. 6, p. 445–453.

Suryasentana, S. K. & Lehane, B. M., 2014a. Numerical derivation of CPT-based p-y curves for piles in sand. Géotechnique, 64(No. 3), p. 186–194.

Taylor, R. N. (1995). *Centrifuges in modelling: principles and scale effects*. Geotechnical centrifuge technology, 19-33.

Truong, P. (2017). *Experimental investigation on the behaviour of laterally loaded piles in soft clay, sand and residual soils* (Doctoral dissertation, PhD thesis, The University of Western Australia, Perth, Australia).

Wang, H., Lehane, B. M., Bransby, M. F., Askarinejad, A., Wang, L. Z., & Hong, Y. (2022). A simple rotational spring model for laterally loaded rigid piles in sand. *Marine Structures*, *84*, 103225.

Wang, H., Lehane, B. M., Bransby, M. F., Wang, L. Z., & Hong, Y. (2020). A simple approach for predicting the ultimate lateral capacity of a rigid pile in sand. *Géotechnique Letters*, *10*(3), 429-435.

WindEurope asbl/vzw. (2022, April 2). *Wind energy in Europe 2020 Statistics and the outlook for 2021-2025*. WindEurope. Retrieved September 16, 2022, from https://windeurope.org/intelligence-platform/product/wind-energy-in-europe-2020-statistics-and-the-outlook-for-2021-2025/

Wrana, B., 2015. PILE LOAD CAPACITY – CALCULATION METHODS. Studia Geotechnica et Mechanica, Vol. 37, No. 4, 2015.

Xue, J., Gavin, K., Murphy, G., Doherty, P., & Igoe, D. (2016). *Optimization technique to determine the py curves of laterally loaded stiff piles in dense sand*. ASTM International.

Yang, K., & Liang, R. (2019). Methods for deriving py curves from instrumented lateral load tests. *Geotechnical testing journal*, *30*(1), 31-38.

Zhang, W., & Askarinejad, A. (2019). *Centrifuge modelling of submarine landslides due to static liquefaction*. Landslides, 16(10), 1921-1938.

Appendix

A. Pile Load Test CPT- and H-y curves

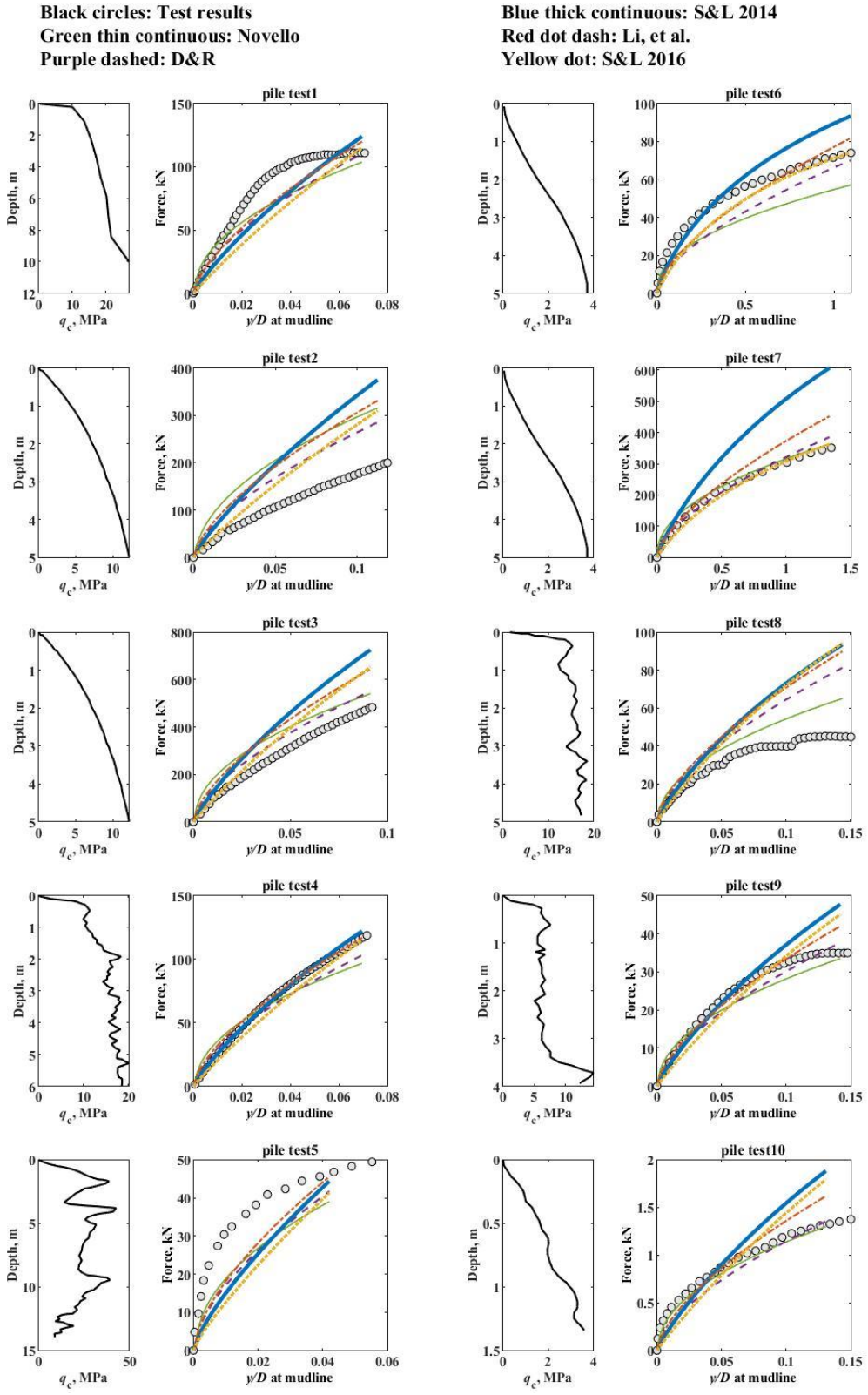

Black circles: Test results
Green thin continuous: Novello
Purple dashed: D&R

Blue thick continuous: S&L 2014
Red dot dash: Li, et al.
Yellow dot: S&L 2016

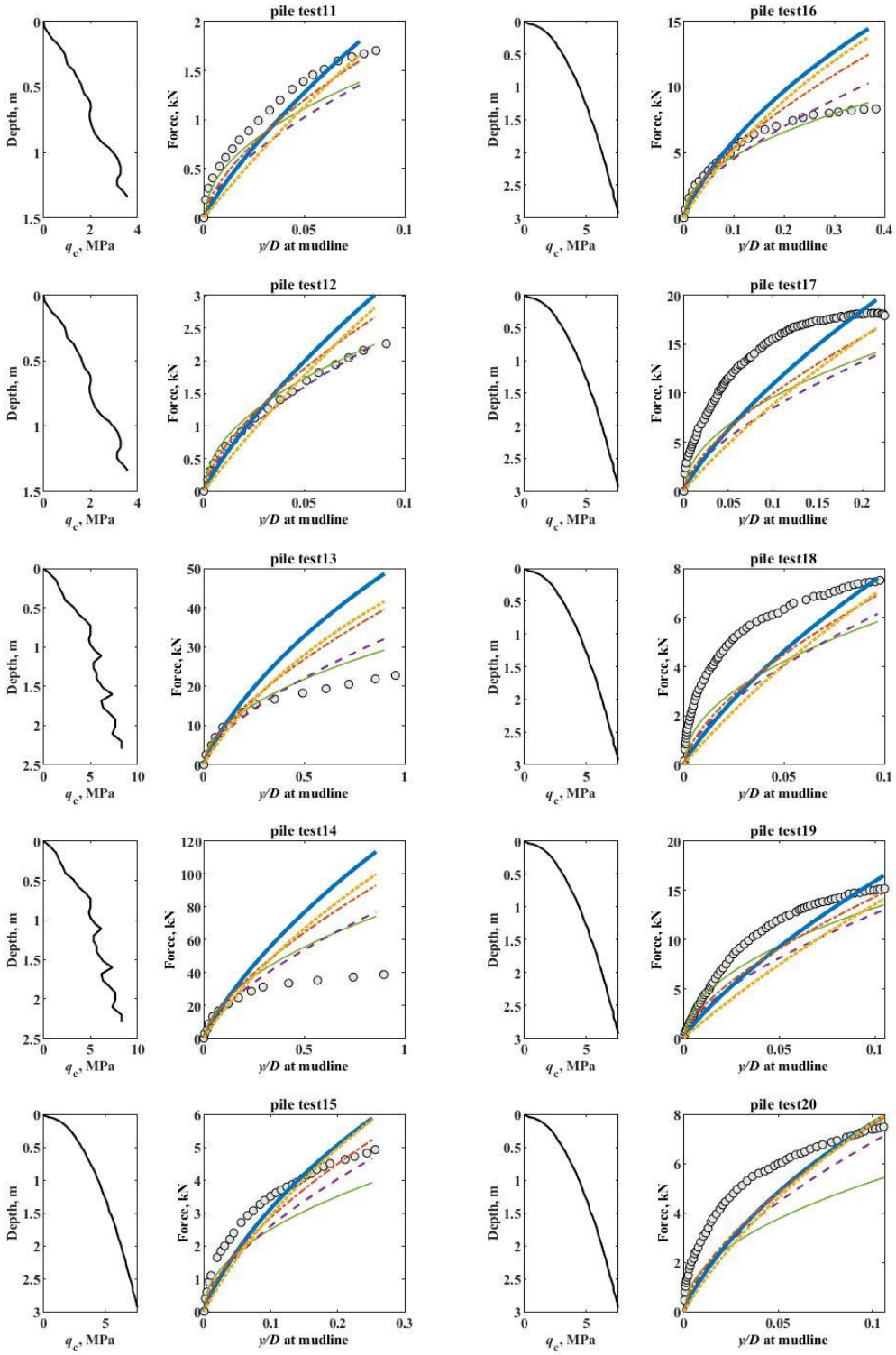

Black circles: Test results
Green thin continuous: Novello
Purple dashed: D&R

Blue thick continuous: S&L 2014
Red dot dash: Li, et al.
Yellow dot: S&L 2016

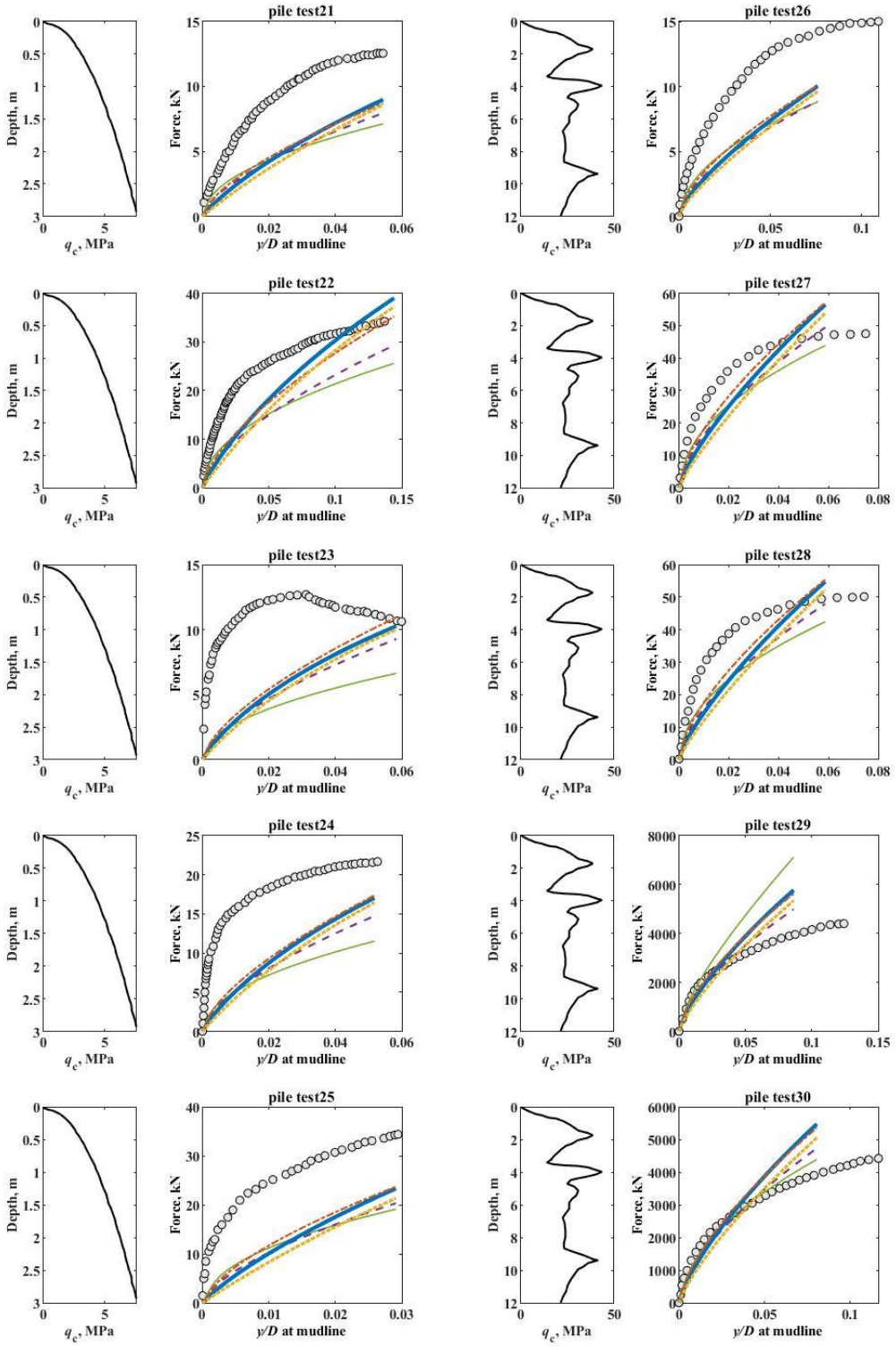

Black circles: Test results
Green thin continuous: Novello
Purple dashed: D&R

Blue thick continuous: S&L 2014
Red dot dash: Li, et al.
Yellow dot: S&L 2016

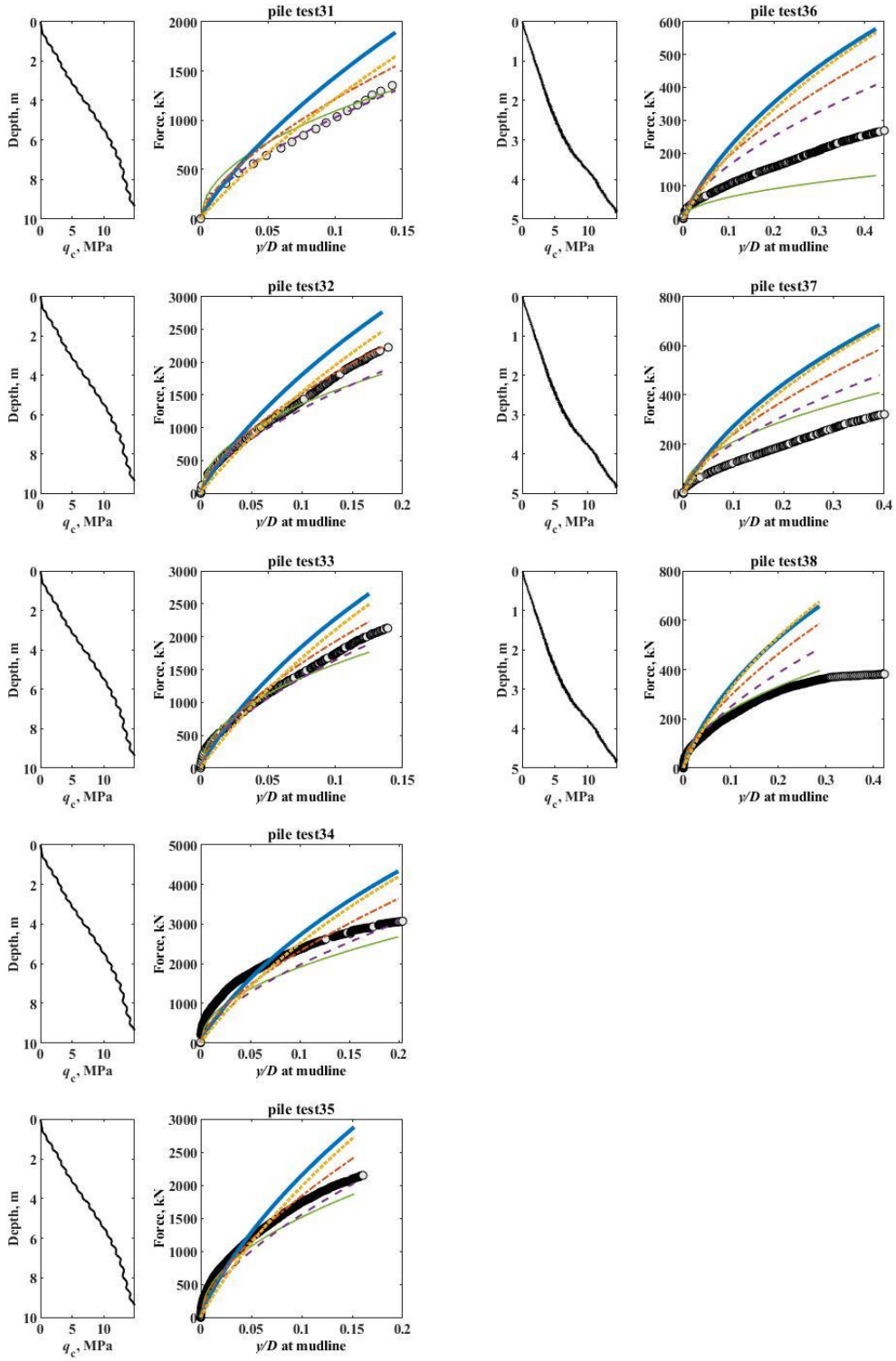

B. Summary PLT database information

Test nr.	Field/Lab	Acceleration level (g)	Location	Soil	CPT profile	Diameter (m)	Length (m)	L/D	max y/D at y0	Type	Source
1	F	na	Blessington, Ireland	Sand	Yes	0.34	2.2	6.5	0.068	Steel Pipe Pile	Doherty et al. (2012)
2	L	20		sil. sand	yes	0.5	5.0	10.0	0.112	open steel pipe pile	Haouari & Bouafia (2020)
3	L	20		sil. sand	yes	0.9	5.0	5.6	0.091	open steel pipe pile	Haouari & Bouafia (2020)
4	F	na	Blessington Ireland	sil. sand	yes	0.34	2.2	6.5	0.069	open steel pipe pile	Li et al (2017)
5	F	na	Dunkirk	sil. sand	yes	0.762	2.29	3.0	0.042	open steel pipe pile	Foursoff (2018)
6	L	50		sil. sand	yes	0.5	2.50	5.0	1.082	?	Lehane & Guo (2017)
7	L	50		sil. sand	yes	0.5	5.0	10.0	1.312	?	Lehane & Guo (2017)
8	F	na	Blessington Ireland	fine sil. Sand	yes	0.245	1.5	6.1	0.143	open steel pipe pile	Xue et al. (2016)
9	F	na	Garryhesta Ireland	fine silty sil. Sand	yes	0.2445	1.5	6.1	0.141	open steel pipe pile	Murphy et al. (2016)
10	L	na		sandy silt	yes	0.165	0.915	5.5	0.138	closed steel pile	Zhu et al. (2015)
11	L	na		sandy silt	yes	0.165	0.915	5.5	0.081	closed steel pile	Zhu et al. (2015)
12	L	na		sandy silt	yes	0.165	0.915	5.5	0.090	closed steel pile	Zhu et al. (2015)
13	F	na	Chatenenay sur-Seine, France	poorly graded siliceous sand	yes	0.1	1.53	15.3	0.946	closed steel grout filled pile	Bouafia (2007)
14	F	na	Chatenenay sur-Seine, France	poorly graded siliceous sand	yes	0.1	2.30	22.95	0.932	closed steel grout filled pile	Bouafia (2007)
15	F	na	Shenton Park (Perth), Western Australia	sil. sand	yes	0.127	0.75	5.9	0.245	open steel pipe pile	Wang et al. (2020)
16	F	na	Shenton Park (Perth), Western Australia	sil. sand	yes	0.127	1.0	7.9	0.373	open steel pipe pile	Wang et al. (2020)
17	F	na	Shenton Park (Perth), Western Australia	sil. sand	yes	0.127	1.5	11.8	0.217	open steel pipe pile	Wang et al. (2020)
18	F	na	Shenton Park (Perth), Western Australia	sil. sand	yes	0.169	1.0	5.9	0.095	open steel pipe pile	Wang et al. (2020)
19	F	na	Shenton Park (Perth), Western Australia	sil. sand	yes	0.169	1.5	8.9	0.103	open steel pipe pile	Wang et al. (2020)
20	F	na	Shenton Park (Perth), Western Australia	sil. sand	yes	0.273	0.75	2.7	0.104	open steel pipe pile	Wang et al. (2020)
21	F	na	Shenton Park (Perth), Western Australia	sil. sand	yes	0.273	1.0	3.7	0.053	open steel pipe pile	Wang et al. (2020)
22	F	na	Shenton Park (Perth), Western Australia	sil. sand	yes	0.273	1.5	5.5	0.144	open steel pipe pile	Wang et al. (2020)
23	F	na	Shenton Park (Perth), Western Australia	sil. sand	yes	0.457	0.8	1.6	0.058	open steel pipe pile	Wang et al. (2020)
24	F	na	Shenton Park (Perth), Western Australia	sil. sand	yes	0.457	1.0	2.2	0.051	open steel pipe pile	Wang et al. (2020)
25	F	na	Shenton Park (Perth), Western Australia	sil. sand	yes	0.457	1.5	3.3	0.029	open steel pipe pile	Wang et al. (2020)
26	F	na	Dunkirk, France	sil. sand	yes	0.273	1.43	5.24	0.076	open steel pipe pile	McAdam et al. (2019)
27	F	na	Dunkirk, France	sil. sand	yes	0.762	2.27	2.98	0.059	open steel pipe pile	McAdam et al. (2019)
28	F	na	Dunkirk, France	sil. sand	yes	0.762	2.24	2.94	0.059	open steel pipe pile	McAdam et al. (2019)
29	F	na	Dunkirk, France	sil. sand	yes	2.0	10.61	5.31	0.086	open steel pipe pile	McAdam et al. (2019)
30	F	na	Dunkirk, France	sil. sand	yes	2.0	10.57	5.29	0.080	open steel pipe pile	McAdam et al. (2019)
31	L	100		fine sil. Sand (GEBA)	yes	1.8	9.0	5.0	0.153	open aluminium tube	own lab tests
32	L	100		fine sil. Sand (GEBA)	yes	1.8	9.0	5.0	0.186	open aluminium tube	own lab tests
33	L	100		fine sil. Sand (GEBA)	yes	2.5	9.0	3.6	0.193	open aluminium tube	own lab tests
34	L	100		fine sil. Sand (GEBA)	yes	2.5	9.0	3.6	0.283	open aluminium tube	own lab tests
35	L	100		fine sil. Sand (GEBA)	yes	2.5	9.0	3.6	0.543	open aluminium tube	own lab tests
36	L	50		fine sil. Sand (GEBA)	yes	0.9	4.5	5.0	0.434	open aluminium tube	own lab tests
37	L	50		fine sil. Sand (GEBA)	yes	0.9	4.5	5.0	0.397	open aluminium tube	own lab tests
38	L	50		fine sil. Sand (GEBA)	yes	1.25	4.5	3.6	0.416	open aluminium tube	own lab tests

C. Accuracy- and ratio metric values per PLT

	η										ρ									
	initial response					ultimate response					initial response					ultimate response				
	Novello	D&R	S&L 2014	Li et al.	S&L 2016	Novello	D&R	S&L 2014	Li et al.	S&L 2016	Novello	D&R	S&L 2014	Li et al.	S&L 2016	Novello	D&R	S&L 2014	Li et al.	S&L 2016
1	0.826	0.818	0.783	0.824	0.685	0.853	0.806	0.869	0.556	0.794	1.084	0.880	0.701	0.885	0.547					
2	-0.539	0.198	0.139	0.461	0.249	0.104	-0.061	0.232	0.762	0.480	2.920	2.078	1.834	2.285	1.254	1.684	1.500	1.942	1.737	1.593
3	0.209	0.768	0.594	0.819	0.609	0.521	0.419	0.632	0.930	0.713	1.884	1.416	1.309	1.582	0.960					
4	0.753	0.882	0.897	0.893	0.975	0.977	0.817	0.995	0.818	0.922	1.396	1.161	1.009	1.264	0.796					
5	0.651	0.788	0.611	0.819	0.564	0.849	0.652	0.891	0.486	0.778	0.610	0.553	0.486	0.586	0.409					
6	0.816	0.723	0.507	0.806	0.425	0.834	0.527	0.886	0.253	0.892	0.857	0.516	0.405	0.533	0.232	0.686	0.582	0.761	0.641	0.565
7	-0.783	0.939	0.399	0.953	0.922	0.423	0.610	0.826	0.536	0.946	2.977	1.697	1.098	1.457	0.542	1.419	1.033	1.212	1.075	0.728
8	0.575	0.705	0.692	0.493	0.844	0.323	0.618	0.351	0.915	0.363	1.556	1.371	1.115	1.442	0.898	1.364	1.620	1.834	1.778	1.808
9	0.742	0.886	0.924	0.914	0.908	0.860	0.908	0.931	0.699	0.872	1.382	1.084	0.895	1.144	0.663	0.868	0.929	1.143	1.028	1.054
10	0.860	0.947	0.656	0.918	0.628	0.773	0.747	0.890	0.487	0.818	0.844	0.615	0.547	0.696	0.406	0.946	0.950	1.284	1.129	1.198
11	0.830	0.809	0.638	0.747	0.619	0.915	0.728	0.876	0.483	0.834	0.844	0.622	0.560	0.705	0.419					
12	0.818	0.966	0.910	0.969	0.892	0.773	0.945	0.856	0.706	0.870	1.186	0.875	0.802	0.996	0.608					
13	0.768	0.820	0.857	0.764	0.700	0.249	0.942	0.547	0.462	0.483	1.103	0.766	0.591	0.853	0.379	0.987	0.813	0.989	0.954	0.785
14	0.805	0.422	0.880	0.466	0.718	-0.147	0.928	0.181	0.488	0.118	1.232	0.908	0.714	0.980	0.473	1.170	0.960	1.103	1.099	0.888
15	0.758	0.748	0.590	0.817	0.503	0.876	0.621	0.887	0.386	0.859	0.797	0.596	0.476	0.623	0.352	0.713	0.741	0.893	0.815	0.834
16	0.911	0.928	0.766	0.889	0.694	0.611	0.862	0.782	0.501	0.685	1.060	0.745	0.630	0.836	0.438	0.889	0.859	1.120	1.016	0.986
17	0.589	0.664	0.417	0.605	0.377	0.788	0.469	0.712	0.258	0.658	0.595	0.407	0.343	0.454	0.225	0.617	0.547	0.703	0.640	0.569
18	0.557	0.692	0.445	0.684	0.406	0.803	0.482	0.763	0.315	0.721	0.553	0.424	0.361	0.456	0.270					
19	0.874	0.818	0.682	0.737	0.611	0.859	0.741	0.829	0.437	0.725	1.002	0.702	0.584	0.758	0.401	0.881	0.841	1.061	0.954	0.905
20	0.560	0.659	0.547	0.808	0.510	0.877	0.579	0.874	0.434	0.853	0.568	0.533	0.472	0.559	0.387	0.715	0.929	1.034	1.023	1.034
21	0.507	0.520	0.465	0.555	0.437	0.609	0.497	0.604	0.370	0.567	0.503	0.443	0.393	0.470	0.320					
22	0.550	0.653	0.449	0.694	0.440	0.847	0.514	0.825	0.344	0.807	0.568	0.446	0.410	0.507	0.308	0.675	0.733	0.957	0.874	0.892
23	0.276	0.475	0.314	0.633	0.322	0.701	0.360	0.741	0.280	0.669	0.259	0.282	0.280	0.322	0.236					
24	0.346	0.477	0.367	0.586	0.379	0.669	0.421	0.686	0.328	0.632	0.325	0.330	0.327	0.377	0.273					
25	0.471	0.550	0.451	0.578	0.466	0.659	0.517	0.673	0.399	0.598	0.453	0.415	0.407	0.473	0.336					
26	0.559	0.576	0.486	0.556	0.451	0.601	0.530	0.626	0.395	0.564	0.575	0.487	0.435	0.528	0.374					
27	0.694	0.831	0.657	0.888	0.625	0.890	0.733	0.902	0.539	0.872	0.681	0.621	0.563	0.688	0.472					
28	0.624	0.763	0.592	0.827	0.562	0.881	0.660	0.906	0.484	0.841	0.593	0.542	0.491	0.601	0.412					
29	0.907	0.446	0.879	0.863	0.867	0.730	0.941	0.733	0.741	0.825	0.999	0.820	0.780	0.879	0.656					
30	0.876	0.944	0.820	0.903	0.809	0.789	0.888	0.791	0.691	0.864	0.857	0.784	0.748	0.843	0.629					
31	0.633	0.907	0.972	0.975	0.916	0.636	0.874	0.827	0.706	0.843	1.361	0.954	0.893	1.072	0.612	1.065	1.002	1.403	1.185	1.189
32	0.793	0.903	0.870	0.885	0.870	0.755	0.964	0.951	0.622	0.906	1.261	0.877	0.818	0.987	0.563	0.965	0.910	1.279	1.078	1.095
33	0.888	0.932	0.860	0.941	0.855	0.736	0.919	0.903	0.685	0.842	1.105	0.834	0.797	0.918	0.598	0.910	0.944	1.307	1.108	1.210
34	0.729	0.819	0.567	0.860	0.574	0.777	0.633	0.903	0.445	0.807	0.738	0.551	0.520	0.609	0.387	0.808	0.832	1.148	0.979	1.062
35	0.891	0.882	0.706	0.893	0.731	0.780	0.798	0.930	0.572	0.844	0.902	0.687	0.667	0.770	0.504	0.869	0.892	1.232	1.054	1.136
36	0.624	0.551	0.816	0.441	0.776	-0.181	0.701	0.132	0.799	-0.072	0.620	1.073	0.964	1.189	0.706	0.626	1.553	2.059	1.824	1.851
37	-0.007	0.547	0.501	0.433	0.540	-0.197	0.311	0.120	0.809	-0.093	1.952	1.404	1.287	1.571	0.950	1.690	1.635	2.193	1.928	1.988
38	0.849	0.914	0.904	0.774	0.847	0.349	0.885	0.534	0.747	0.353	1.142	0.878	0.830	0.987	0.651	1.109	1.170	1.560	1.384	1.509

D. Ratio metric distributions per model

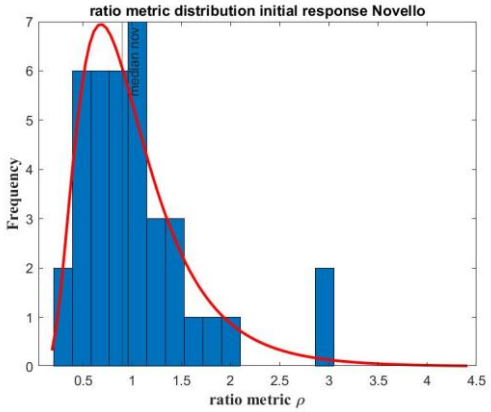

(a)

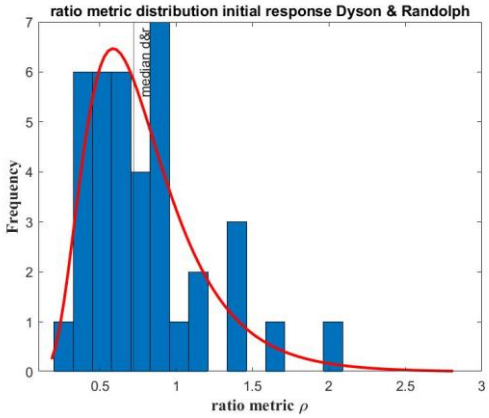

(b)

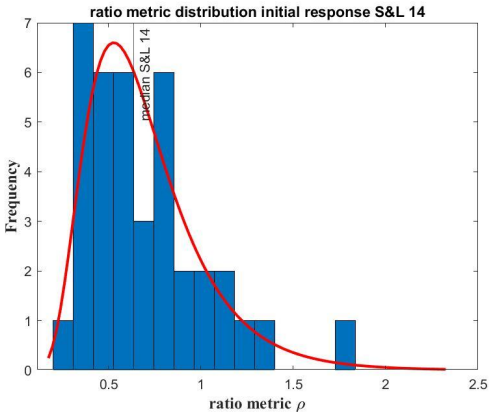

(c)

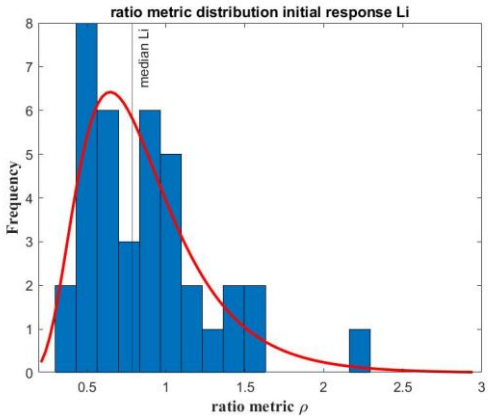

(d)

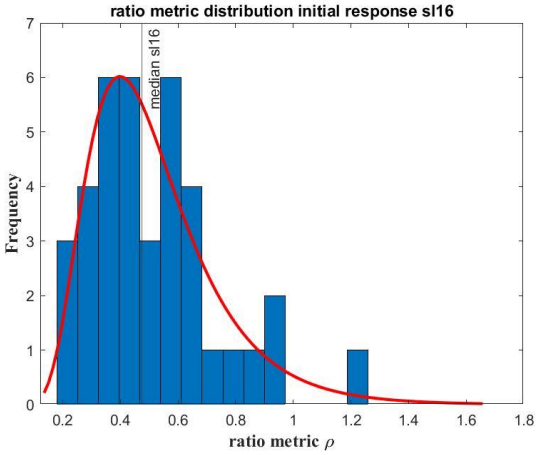

(e)

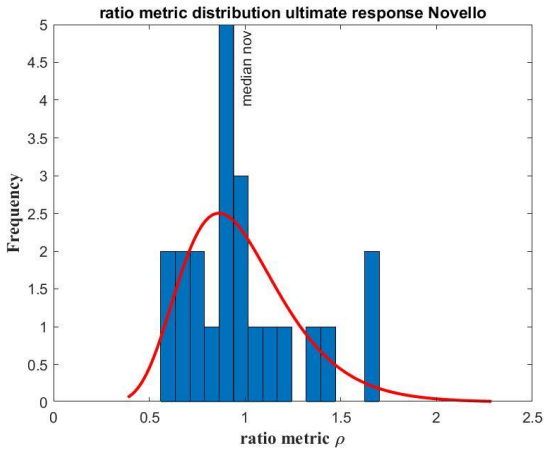
ratio metric distribution ultimate response Novello
median nov
Frequency
ratio metric ρ

(f)

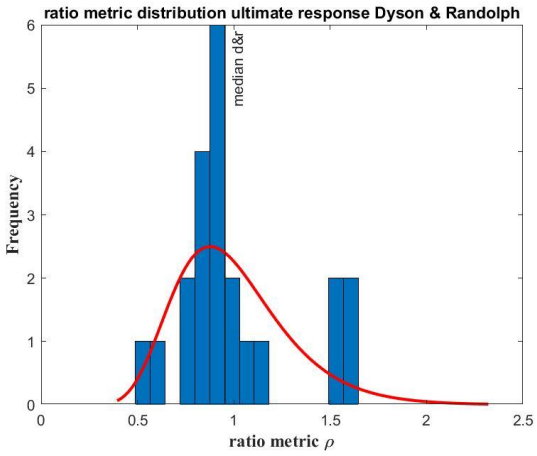
ratio metric distribution ultimate response Dyson & Randolph
median d&r
Frequency
ratio metric ρ

(g)

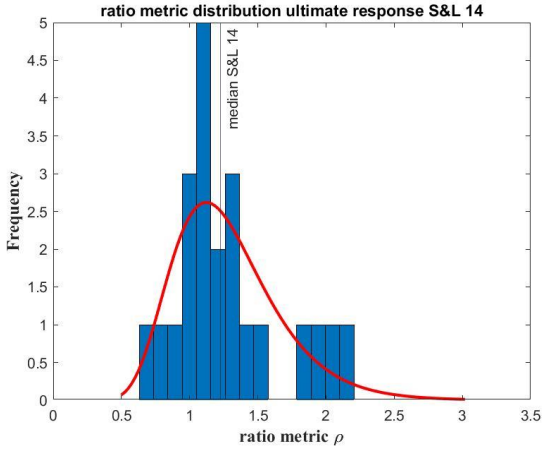
ratio metric distribution ultimate response S&L 14
median S&L 14
Frequency
ratio metric ρ

(h)

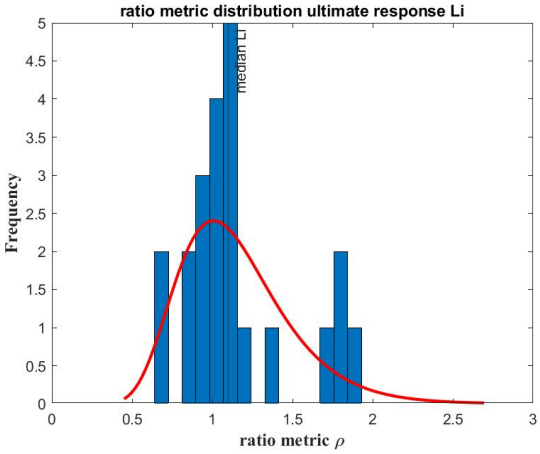
ratio metric distribution ultimate response Li
median Li
Frequency
ratio metric ρ

(i)

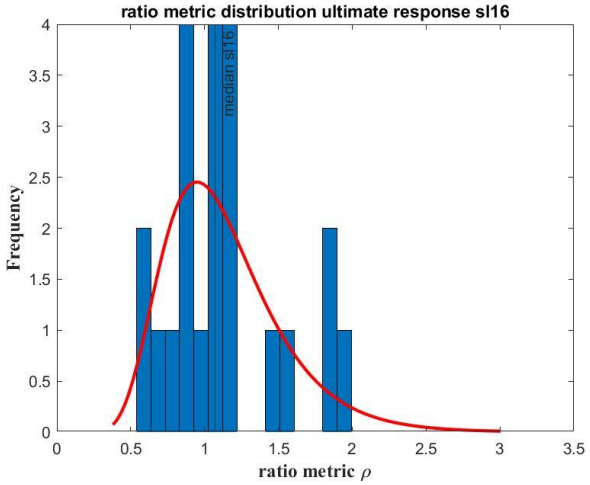
ratio metric distribution ultimate response sl16
median sl16
Frequency
ratio metric ρ

(j)

E. Accuracy metric correlations

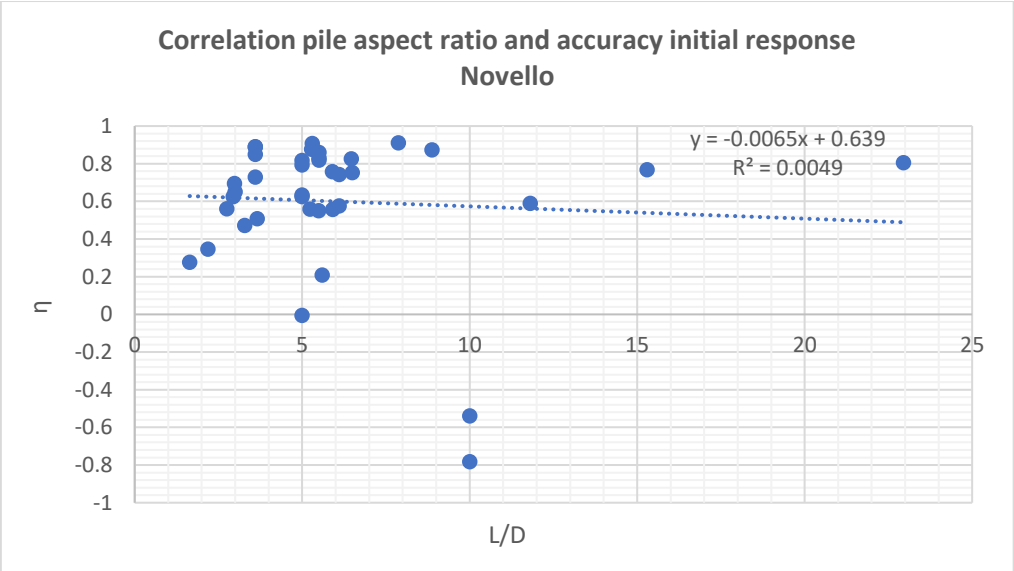

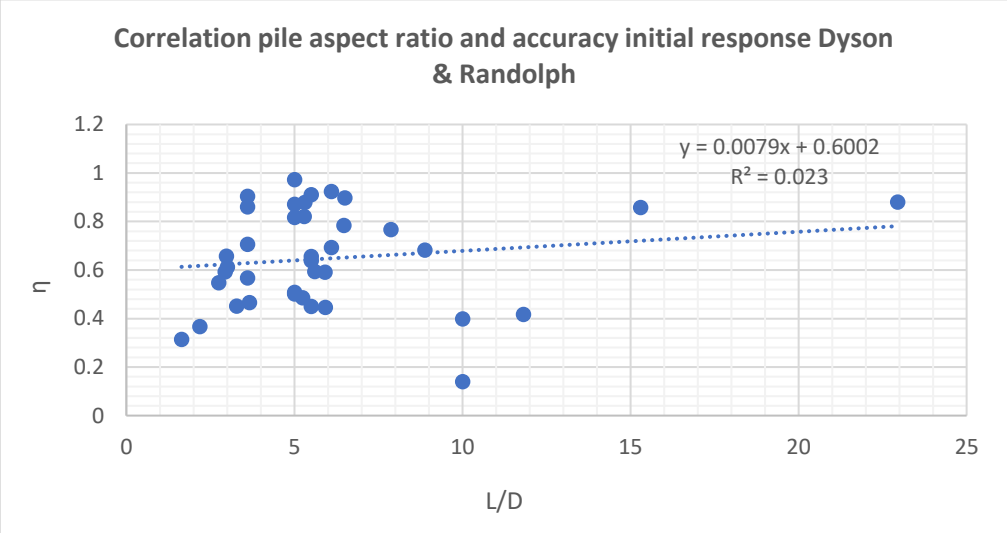

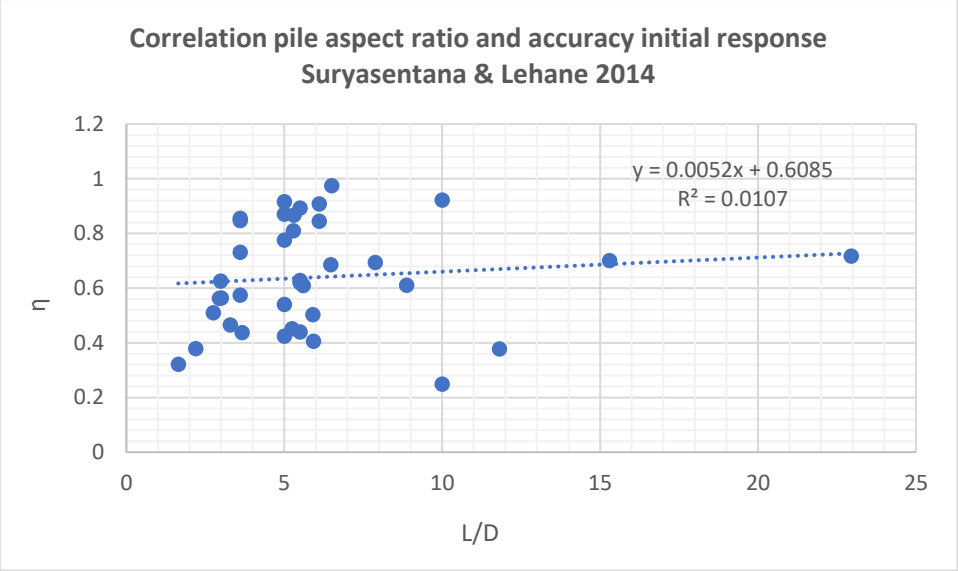
Correlation pile aspect ratio and accuracy initial response Suryasentana & Lehane 2014
y = 0.0052x + 0.6085
R² = 0.0107
η
L/D
1.2
1
0.8
0.6
0.4
0.2
0
0
5
10
15
20
25

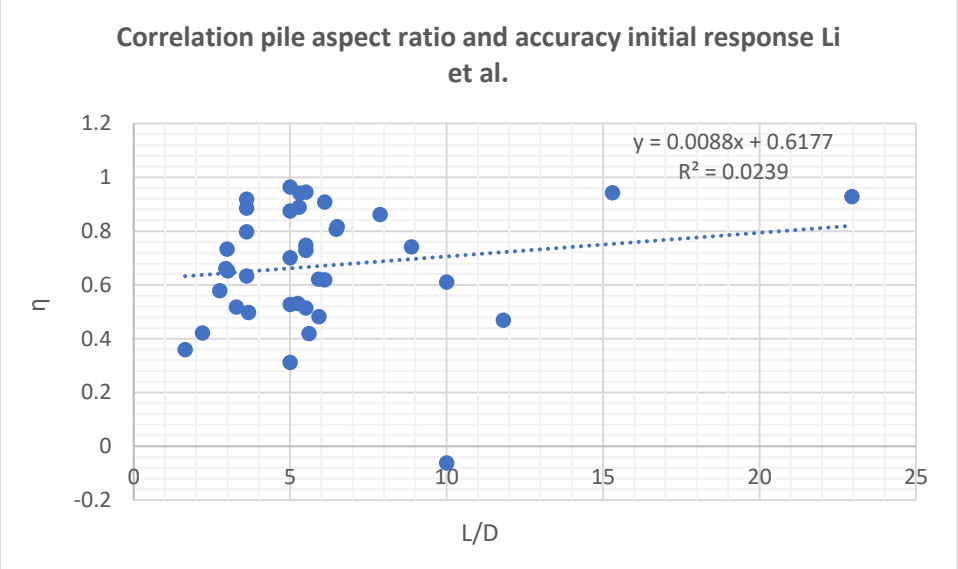
Correlation pile aspect ratio and accuracy initial response Li et al.
y = 0.0088x + 0.6177
R² = 0.0239
η
L/D
1.2
1
0.8
0.6
0.4
0.2
0
-0.2
0
5
10
15
20
25

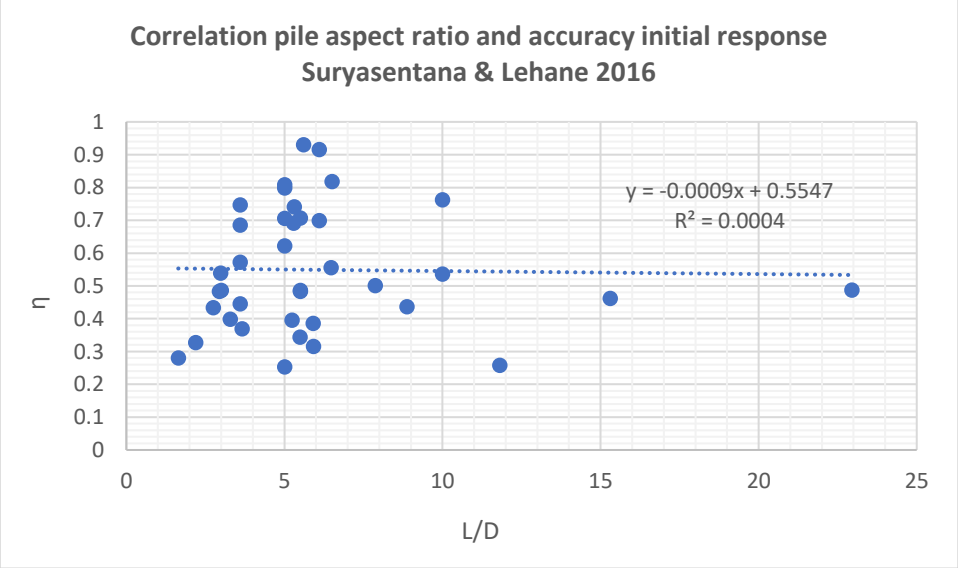
Correlation pile aspect ratio and accuracy initial response Suryasentana & Lehane 2016
y = -0.0009x + 0.5547
R² = 0.0004
η
L/D
1
0.9
0.8
0.7
0.6
0.5
0.4
0.3
0.2
0.1
0
0
5
10
15
20
25

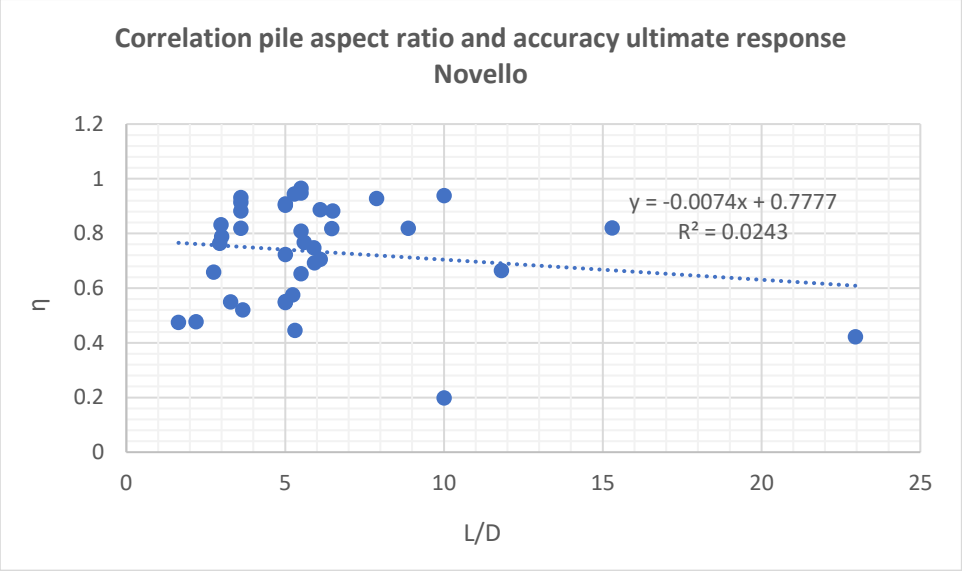
Correlation pile aspect ratio and accuracy ultimate response
Novello
y = -0.0074x + 0.7777
R² = 0.0243
η
L/D
1.2
1
0.8
0.6
0.4
0.2
0
0
5
10
15
20
25

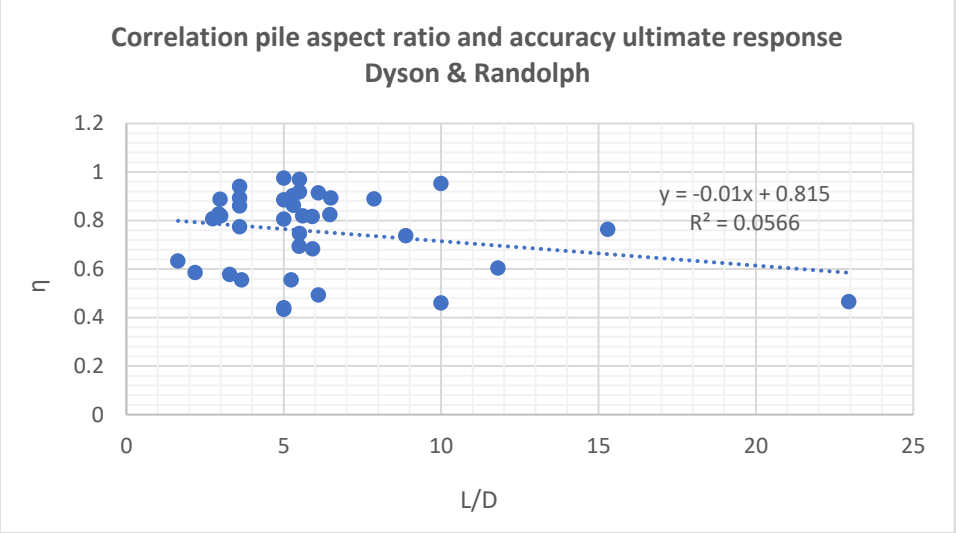
Correlation pile aspect ratio and accuracy ultimate response
Dyson & Randolph
y = -0.01x + 0.815
R² = 0.0566
η
L/D
1.2
1
0.8
0.6
0.4
0.2
0
0
5
10
15
20
25

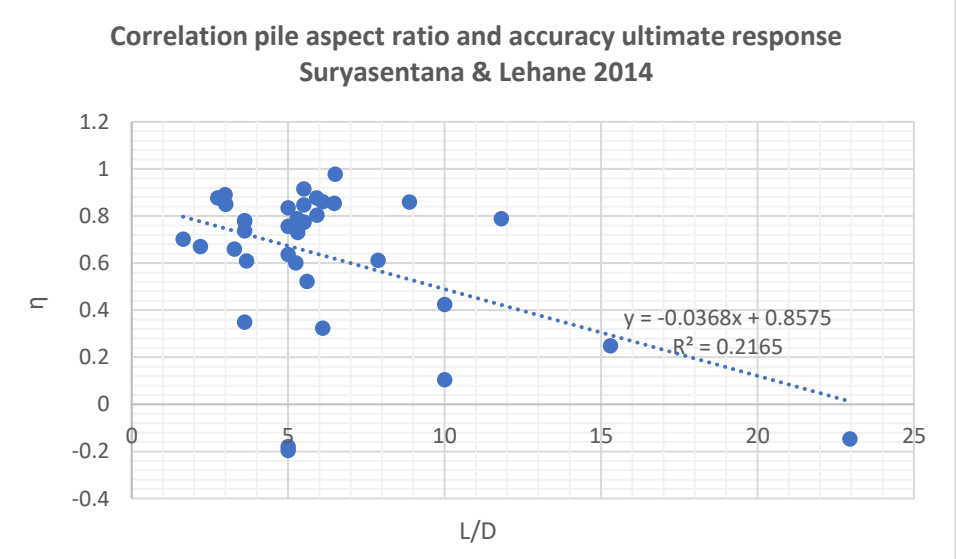
Correlation pile aspect ratio and accuracy ultimate response
Suryasentana & Lehane 2014
y = -0.0368x + 0.8575
R² = 0.2165
η
L/D
1.2
1
0.8
0.6
0.4
0.2
0
-0.2
-0.4
0
5
10
15
20
25

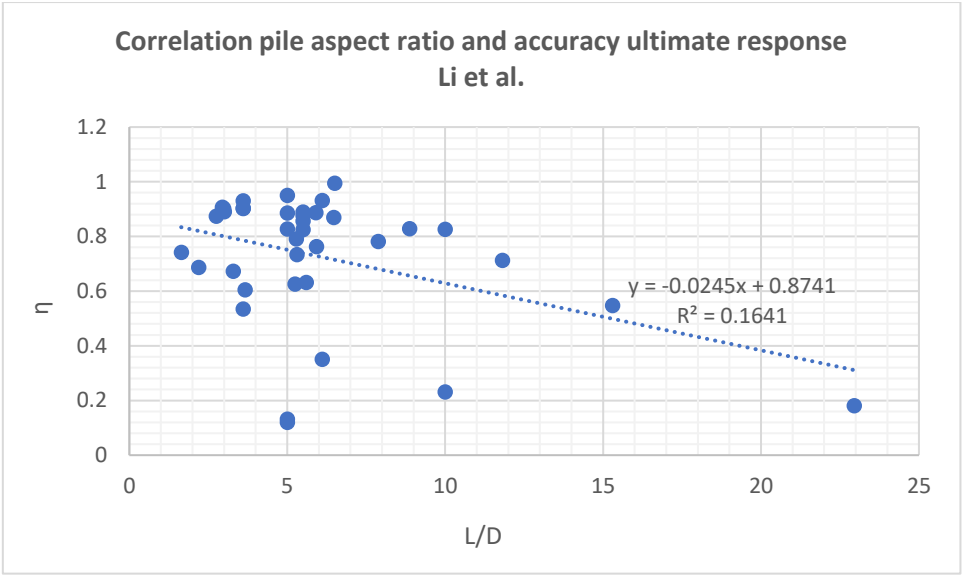
Correlation pile aspect ratio and accuracy ultimate response
Li et al.
η
L/D
y = -0.0245x + 0.8741
R² = 0.1641
1.2
1
0.8
0.6
0.4
0.2
0
0
5
10
15
20
25

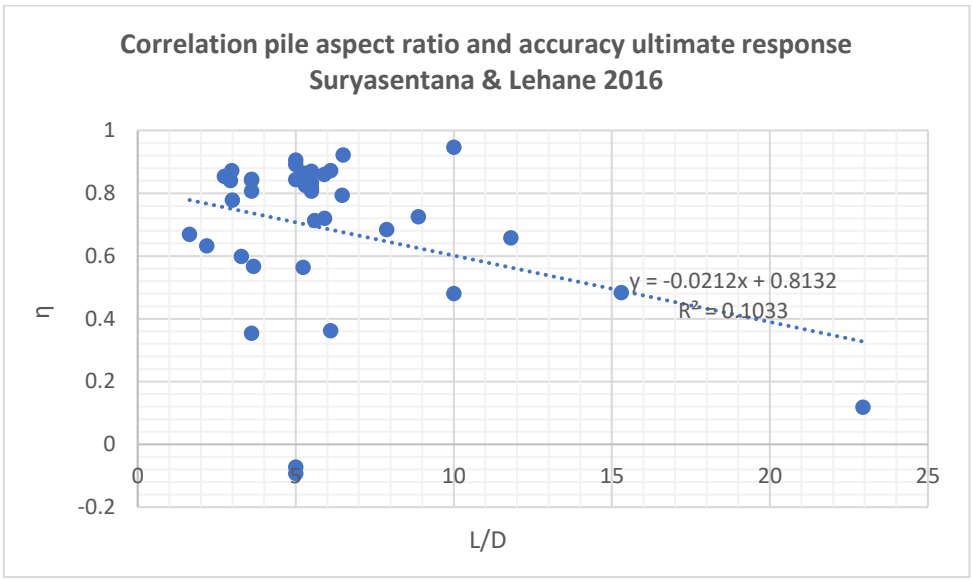
Correlation pile aspect ratio and accuracy ultimate response
Suryasentana & Lehane 2016
η
L/D
y = -0.0212x + 0.8132
R² = 0.1033
1
0.8
0.6
0.4
0.2
0
-0.2
0
5
10
15
20
25

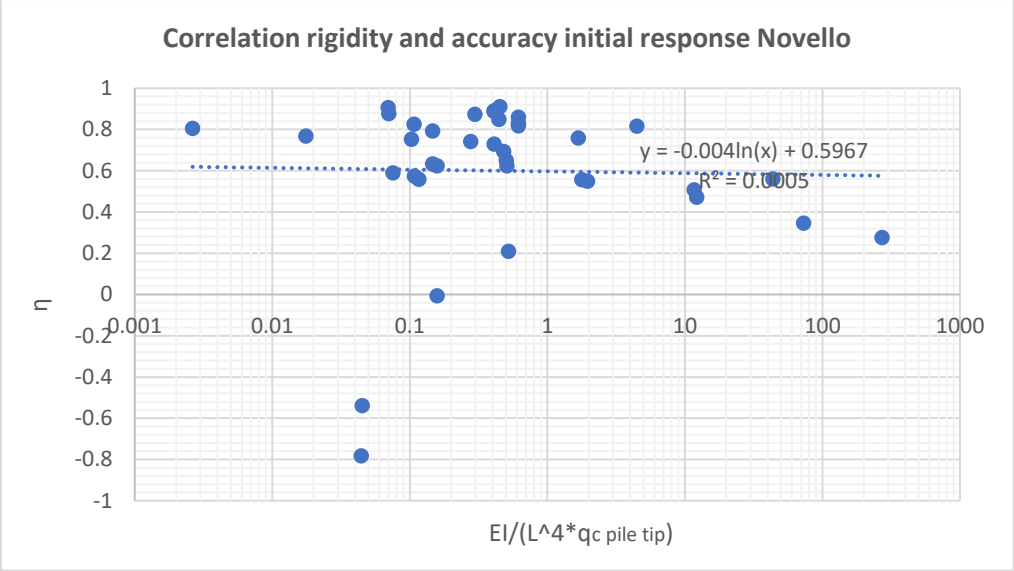
Correlation rigidity and accuracy initial response Novello
y = -0.004ln(x) + 0.5967
R² = 0.0005
η
EI/(L^4*qc pile tip)
1
0.8
0.6
0.4
0.2
0
-0.2
-0.4
-0.6
-0.8
-1
0.001
0.01
0.1
1
10
100
1000

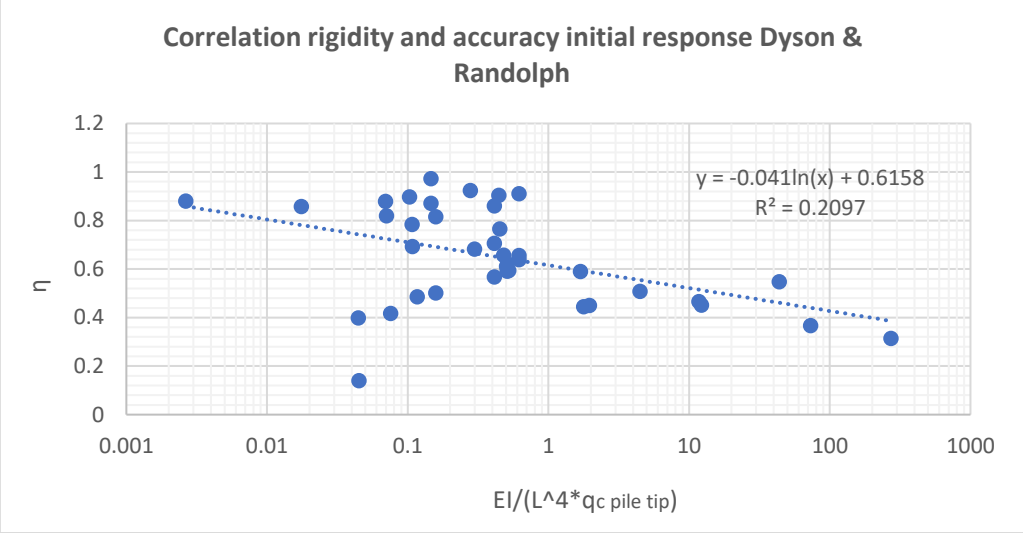
Correlation rigidity and accuracy initial response Dyson & Randolph
y = -0.041ln(x) + 0.6158
R² = 0.2097
η
EI/(L^4*qc pile tip)
1.2
1
0.8
0.6
0.4
0.2
0
0.001
0.01
0.1
1
10
100
1000

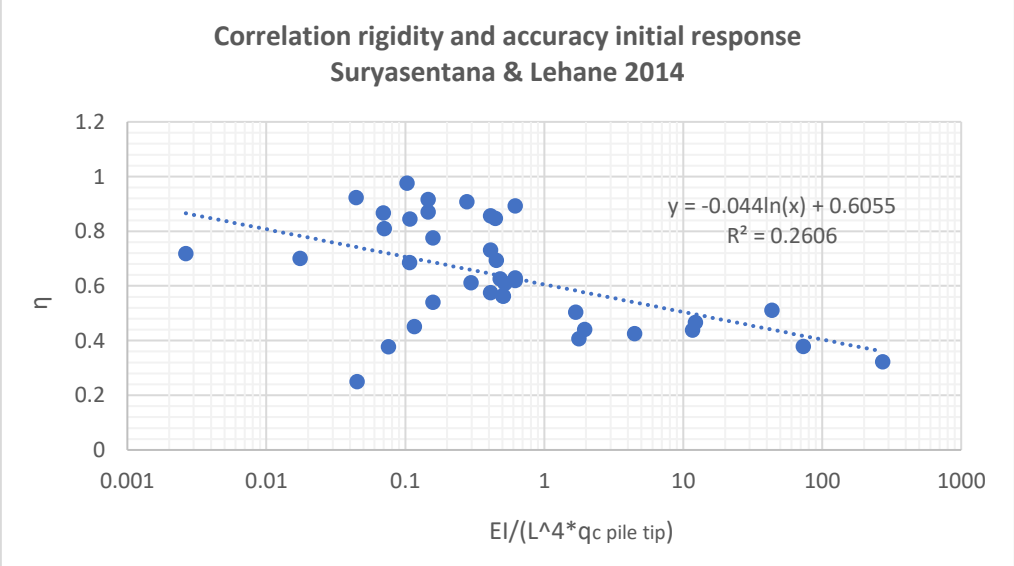
Correlation rigidity and accuracy initial response Suryasentana & Lehane 2014
y = -0.044ln(x) + 0.6055
R² = 0.2606
η
EI/(L^4*qc pile tip)
1.2
1
0.8
0.6
0.4
0.2
0
0.001
0.01
0.1
1
10
100
1000

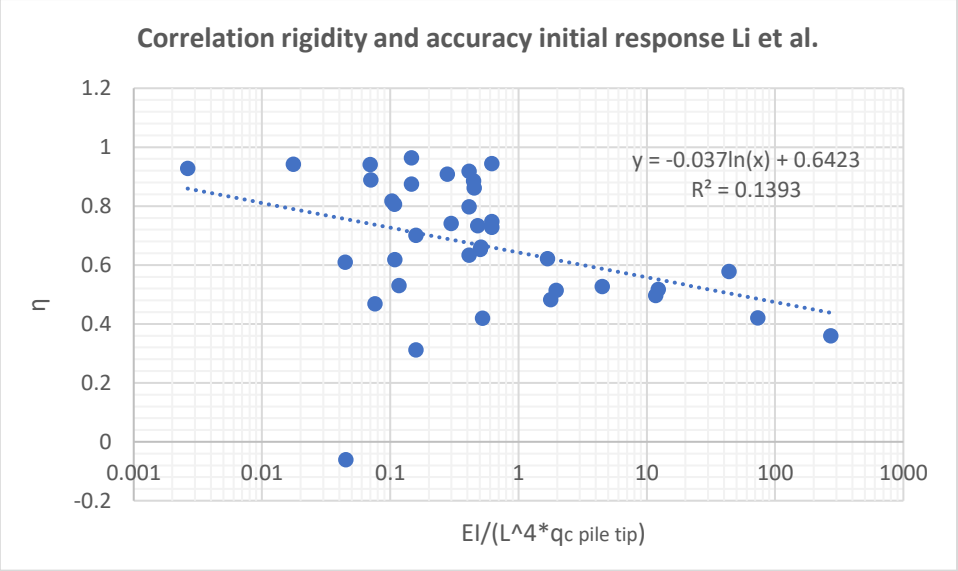
Correlation rigidity and accuracy initial response Li et al.
y = -0.037ln(x) + 0.6423
R² = 0.1393
η
EI/(L^4*qc pile tip)
1.2
1
0.8
0.6
0.4
0.2
0
-0.2
0.001
0.01
0.1
1
10
100
1000

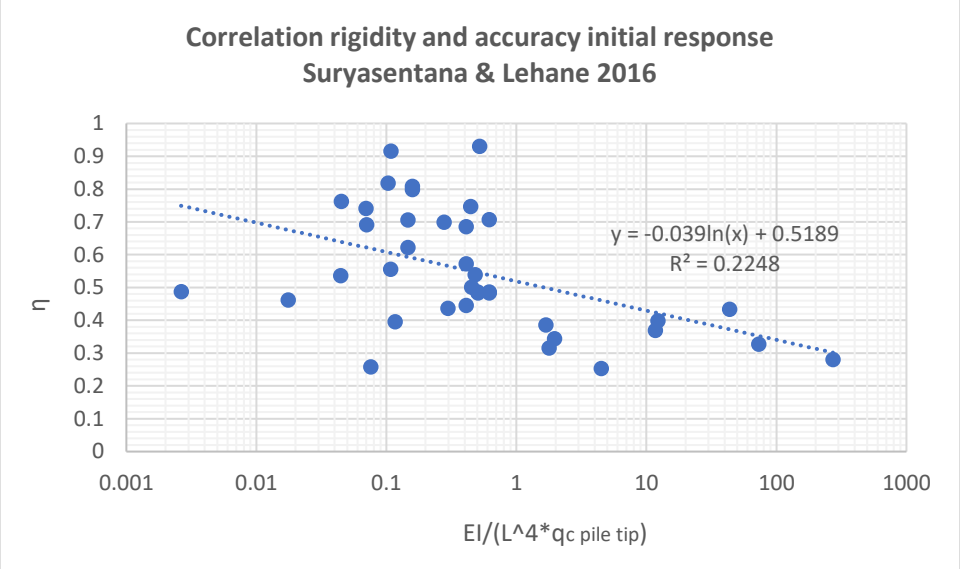
Correlation rigidity and accuracy initial response
Suryasentana & Lehane 2016
y = -0.039ln(x) + 0.5189
R² = 0.2248
η
EI/(L^4*qc pile tip)
1
0.9
0.8
0.7
0.6
0.5
0.4
0.3
0.2
0.1
0
0.001
0.01
0.1
1
10
100
1000

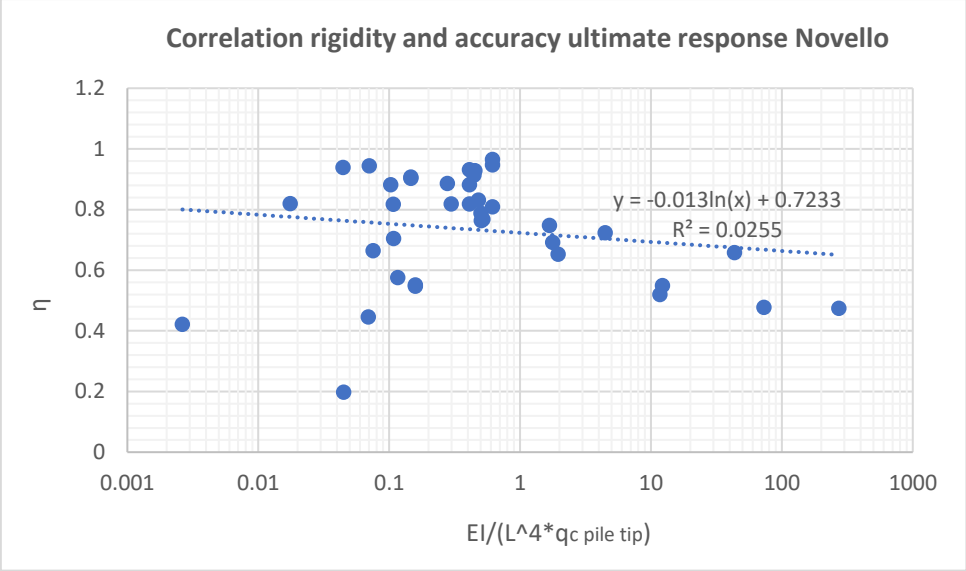
Correlation rigidity and accuracy ultimate response Novello
y = -0.013ln(x) + 0.7233
R² = 0.0255
η
EI/(L^4*qc pile tip)
1.2
1
0.8
0.6
0.4
0.2
0
0.001
0.01
0.1
1
10
100
1000

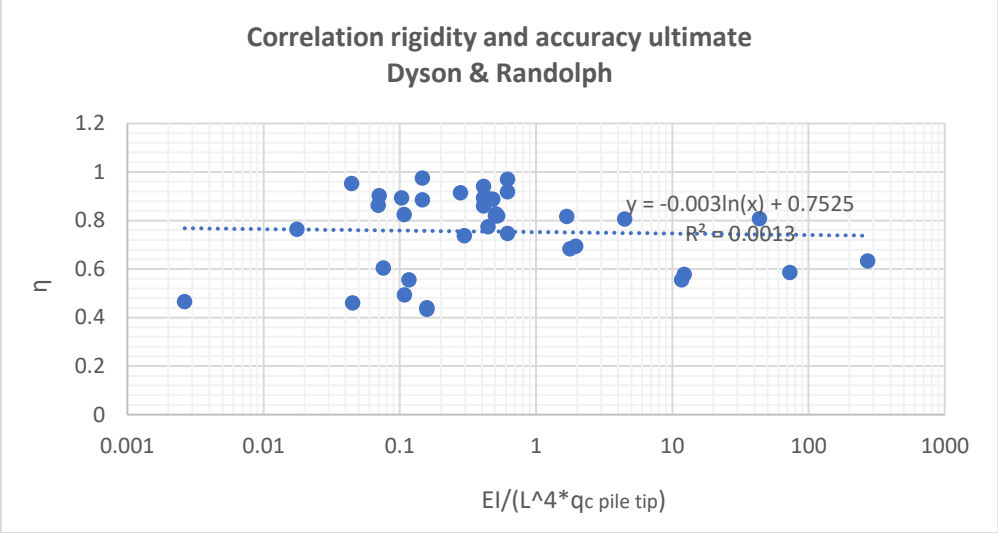
Correlation rigidity and accuracy ultimate
Dyson & Randolph
y = -0.003ln(x) + 0.7525
R² = 0.0013
η
EI/(L^4*qc pile tip)
1.2
1
0.8
0.6
0.4
0.2
0
0.001
0.01
0.1
1
10
100
1000

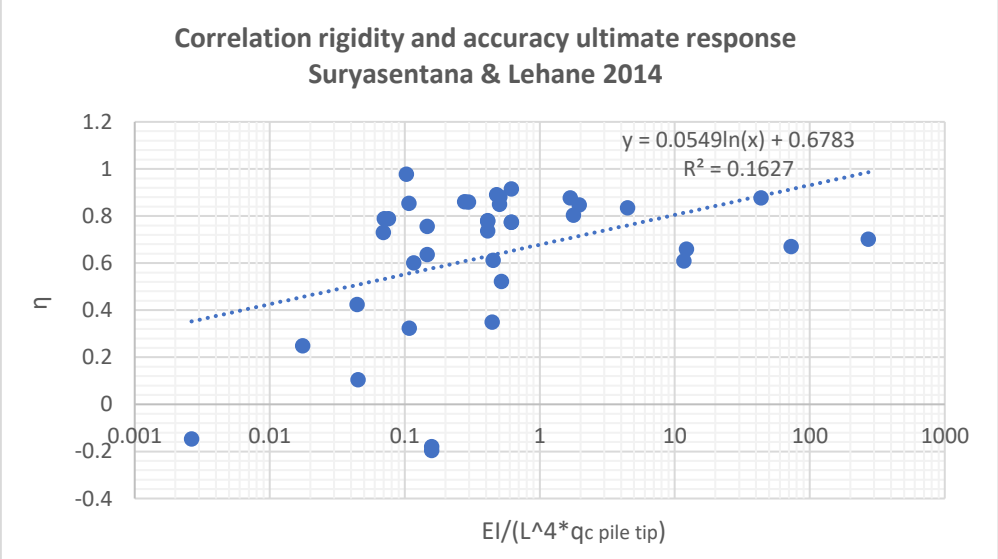
Correlation rigidity and accuracy ultimate response
Suryasentana & Lehane 2014
y = 0.0549ln(x) + 0.6783
R² = 0.1627
η
EI/(L^4*qc pile tip)
1.2
1
0.8
0.6
0.4
0.2
0
-0.2
-0.4
0.001
0.01
0.1
1
10
100
1000

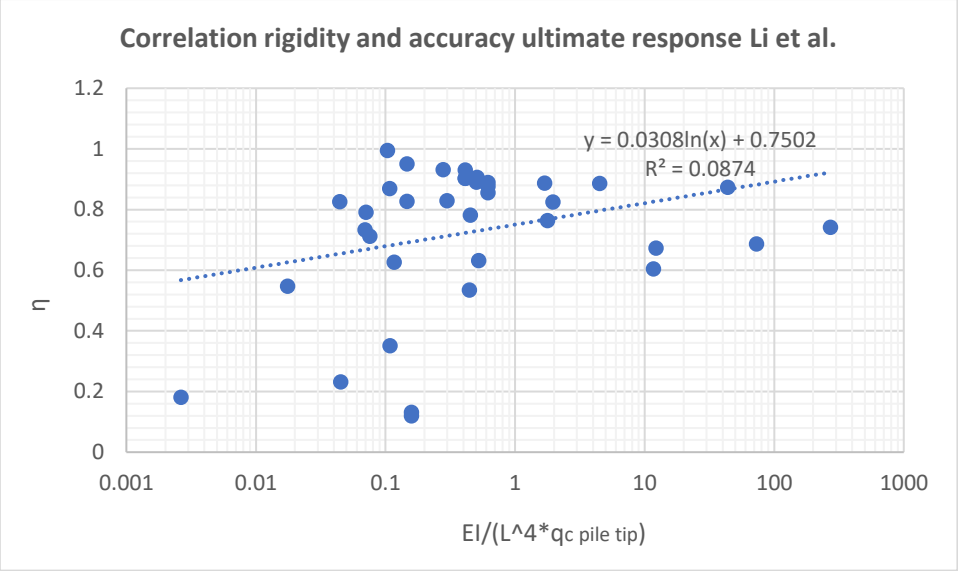
Correlation rigidity and accuracy ultimate response Li et al.
y = 0.0308ln(x) + 0.7502
R² = 0.0874
η
EI/(L^4*qc pile tip)
1.2
1
0.8
0.6
0.4
0.2
0
0.001
0.01
0.1
1
10
100
1000

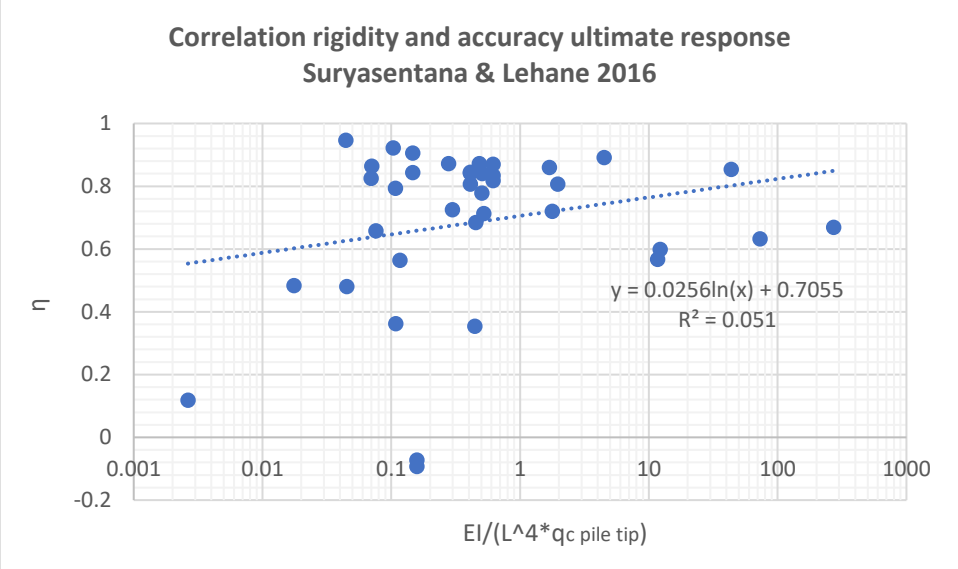
Correlation rigidity and accuracy ultimate response
Suryasentana & Lehane 2016
y = 0.0256ln(x) + 0.7055
R² = 0.051
η
EI/(L^4*qc pile tip)
1
0.8
0.6
0.4
0.2
0
-0.2
0.001
0.01
0.1
1
10
100
1000